ENHANCED COLOUR ENCODING OF MATERIALS DISCRIMINATION INFORMATION FOR MULTIPLE VIEW DUAL-ENERGY X-RAY IMAGING

XUN WANG

A thesis submitted in partial fulfilment of the requirements of
Nottingham Trent University for the degree of Doctor of Philosophy

School of Science and Technology
Nottingham Trent University,
Burton Street,
Nottingham, UK.

Collaborating Establishment:

Home Office Scientific Development Branch (H.O.S.D.B),
Sandridge, UK.

February 2009

COPYRIGHT STATEMENT

ABSTRACT

This thesis reports an investigation into dual-energy X-ray discrimination techniques. These techniques are designed to provide colour-coded materials discrimination information in a sequence of perspective images exhibiting sequential parallax. The methods developed are combined with a novel 3D imaging technique employing depth from motion or kinetic depth effect (KDE). This technique when applied to X-ray images is termed KDEX imaging and was developed previously by the university team for luggage screening applications at security checkpoints.

A primary motivation for this research is that the dual-energy X-ray techniques, which are routinely incorporated into 'standard' 2D luggage scanners, provide relatively crude materials discrimination information. In this work it was critical that robust materials discrimination and colour encoding process was implemented as the sequential parallax exhibited by the KDEX imagery may introduce colour changes, due to the different X-ray beam paths associated with each perspective image. Any introduction of 'colour noise' into the resultant image sequences could affect the perception of depth and hinder the ongoing assessment of the potential utility of the dual-energy KDEX technique.

Two dual-energy discrimination methods have been developed, termed K-II and W-E respectively. Employing the total amount of attenuation measured at each energy level and the weight fraction of layered structures, a combination of the K-II and the W-E techniques enables the computation and extraction of a target objects' effective atomic number (Z_{eff}) and its surface density (ρ_S) in the presence of masking layers. These material parameters (Z_{eff} and ρ_S) together with laminographic layer thickness estimation enable mass density extraction.

A series of experiments investigated the computation of Z_{eff} and ρ_S as a function of system noise and repeatability. The estimation of thickness depends on the depth increment provided by the image capture geometry and the laminographic processing. Within the atomic number range of 6 to 30 and with up to 4 masking layers, the investigated techniques produce an accuracy of Z_{eff} and ρ_S up to 97% and 95% respectively. The thickness estimation technique provided a relatively high accuracy for object thickness' greater than 4cm. Although, the measurement accuracy for relatively thin layers is inherently limited by the minimum resolvable depth increment of the image collection geometry. The mass density extracted had an overall accuracy of greater than 90% for well-estimated thicknesses. Implementing a new four colours scheme highlights the presence of potential threat materials in the resultant KDEX imagery.

This thesis forms part of a larger programme of activity in collaboration with and funded by the UK Home Office Scientific Development Branch, and the US Department of Homeland Security and the EPSRC.

ACKNOWLEDGEMENT

I offer my utmost thanks and appreciation to my supervisors Professor Paul Evans, Dr. JerWang, Chan, and Professor Wayne Cranton for supporting me through my studies as a doctorial student. Limitless thanks to Paul and Dr. J.W Chan for the impeccable guidance and patience throughout the years and especially for reading and commenting on this thesis, though any remaining faults are mine.

I would like to thank those closest to me; Dr. Yong, Liu, Dr. David Downes, YongZhun Zheng, Dr. Cui and B. J. Heismann. They were my main source of encouragement and made the tougher times of research seem easy.

To my parents YanGang, Wang and XiuYing Liu, my wife Shan, Zhu, my wife's parents WenChang Zhu, YuFen Liu; no words are enough to describe their love, understanding and occasional monetary boost that helped me through my studies. I give my heartfelt gratitude.

Last but not least, to all those that I have not mentioned, thank you.

TABLE OF CONTENTS

LIST OF FIGURES

LIST OF TABLES

CHAPTER ONE: INTRODUCTION

1.1 Background

Government organisations in the UK and US acknowledge the threat from weapons and explosive devices concealed by terrorists in luggage. The efficiency and throughput of security checkpoints is a central issue in attempting to combat potential terrorist acts. For example only small amounts of liquids, gels and aerosols etc. are allowed in carry-on baggage, which is restricted by the 3-1-1 rule [1] for carry-on items issued by the US Transportation Security Administration (TSA). The TSA has also introduced a canine programme to enhance air cargo security and millimetre wave technology to detect weapons, explosives and other threat items concealed under layers of clothing on passengers [1]. Since the early of 1990s, academics at Nottingham Trent University (NTU) established an ongoing collaboration with the UK Home Office Scientific Development Branch (HOSDB) and the US Department of Homeland Security (DHS), to develop innovative technological solutions to increase the efficiency of X-ray screening of luggage at security checkpoints.

For example, the lack of visual cues to depth in conventional X-ray transmission images poses serious problems for the security operators manning X-ray scanners at airport checkpoints. This fast-stream screening task attempts to deal with a high-volume of luggage in which the content of each screened item is potentially highly disparate in terms of material composition and spatial distribution. This situation is further exacerbated by an unknown full set of targets including guns, knives and improvised explosive devices (IED). The UK HOSDB and the US DHS have identified that a potential solution is to install systems that are capable of producing high quality three-dimensional (3D) X-ray images [2]. The NTU team has taken a pivotal role in this programme of work for many years [3] [4] and has resulted in the commercialisation of a 3D X-ray scanner technology via a spin-off company. More recently the university team has pioneered a technique which generates dynamic 3D imagery employing a static configuration of multiple line-scan X-ray sensors and a single X-ray source [5] [6] [7].This unique approach employs an image capture geometry which enables the

perception of depth through motion or kinetic depth effect (KDE) [8][9] in the resultant display of the shadowgraph images. Therefore, it is referred to as kinetic depth effect X-ray or KDEX imaging [10]. The ability effectively to 'look around' an object under inspection using multiple views is particularly advantageous in comparison with 'stationary' binocular stereoscopic techniques, which are inherently limited to a relatively small maximum display parallax.

The requirement for visual discrimination of different materials is primarily driven by the requirement for the detection of plastic explosives, which resulted in the adoption of dual-energy X-ray imaging from the medical world in the early 1990's [11][12]. In the range of X-ray energies involved, dual-energy X-ray imaging exploits the integrated effect of Compton scattering and photoelectric absorption. The magnitude of signals measured at high-energy X-ray (~ 140 keV) and low-energy X-ray (~ 80 keV) are analysed for computing materials discrimination information, which is then presented to human operators via a predefined colour scheme. However, the masking and unmasking of object structures produced by the sequential parallax inherent in the KDEX technique, of primary interest in this research, may produce localised colour changes in the display. This effect is fundamental to materials discrimination based on transmission dual-energy X-ray properties. As the partially masked objects rotate, different sections of a target may appear in different colours. The colour will depend upon the masking object as well as the target. It was hypothesised that this colour transition effect could deliver valuable information to reveal a highly camouflaged threat. This hypothesis is an important aspect in a series of research grants awarded by the US DHS, UK HOSDB and the EPSRC.

The research is aimed at discriminating and colourising dual-energy data from line-scan format multiple-view transmission X-ray images. The fundamental requirement is to generate a dual-energy X-ray spectrum from a polychromatic X-ray source and establish an imaging geometry to produce dual-energy line-scan multiple-view transmission X-ray images. A significant challenge in this research programme is the imprecise and limited effective materials discrimination range provided by 'standard' dual-energy techniques employing a polychromatic X-ray source and X-ray sensors with relatively

broad energy sensitivity. The problem is exacerbated by non-uniformity of the X-ray footprint due to heel effect. Existing materials discrimination techniques such as those that employ the conventional discrimination curve methods [3], basis material decomposition (BMD) [13] [14], and the ρZ projection method [15], are all inherently limited in terms of their practical utility when incorporated into security X-ray screening systems. This research programme investigates and develops more accurate methods of computing the materials effective atomic number in combination with the mass density of the objects under inspection. The approach is designed to work under various object masking scenarios in the resultant dual-energy X-ray image sequence. The developed approach cannot correctly identify fully occluded threat materials but can deal with partially overlapped threat materials. The resultant colour encoding scheme incorporates the computed materials effective atomic number and mass density. The resultant imagery is colour coded to highlight a threat window in materials space. These aspects are considered further in terms of the materials identification achievable as practical indicator for the potential take up of these techniques by the security screening industry.

Prior research by the university team includes the modelling of multiple-view imaging geometry for improving image interpretation and commensurate human factors investigation [16][5][17][18][4][10][19], the development of image processing algorithms for image features recognition [20][21], threat image projection and image view synthesis [22][23][24][25][26][27] and, the development of materials discrimination modules for target detection [3] [28] [29]. The derivation of a basis materials subtraction (BMS) method [3], has enabled the extraction of information concerning layered structure from dual-energy imagery. When this information is coupled with the appropriate interrogation and analysis of the parallax (or depth) information provided by stereoscopic X-ray images [30][31], both atomic number and mass density may be estimated. This technique has achieved promising results within the atomic number range of ~6.6 to 13 [3]. However, this limited materials discrimination range is unable to discriminate the target from the masks in many envisaged practical scenarios. The lack of reliable mass density information is a barrier to the further development of such approaches for security screening applications. These

wider considerations have prompted the author to investigate the methods detailed in this thesis as a first step in technique development.

To achieve the research aim and objectives set out in this thesis requires that a materials discrimination technique, which specifically classifies the properties of transmission X-ray images, and a colour encoding scheme for 'moving' X-ray images, be investigated and developed.

1.2 Aim and objectives

The projects principal aim is to develop dual-energy X-ray materials discrimination techniques as an adjunct to a novel multiple view 3D X-ray imaging technique. This will ultimately provide partially rotating colour-coded images containing spatial and materials composition information that will thus significantly improve efficiency and use of security screening at airports.

The principal aim of the work is supported by the following specific objectives:

- investigate a calibration technique to generate dual-energy X-ray spectra utilising single X-ray beam;

- produce line-scan format multiple view dual-energy X-ray images by employing a real time X-ray image intensified system;

- devise techniques to normalise temporal and spatial non-uniformity in the resultant images;

- investigate imaging techniques to discriminate between a wide range of materials by computation of effective atomic number and mass density of multi-layered structure;

- develop a method to estimate the thickness of objects from 'moving' transmission X-ray images;

- develop an appropriate colour encoding scheme to enhance potentially detection and identification of threats in KDEX image sequences.

1.3 Research contributions

A list of the major contributions contained in this thesis is outlined as follows.

- A line-scan format multiple-view dual-energy X-ray imaging calibration scheme. Employing a real-time X-ray system and providing a series of parameters for filtering, collimation and image geometry.

- A materials discrimination method termed the 'K-II technique'. This is derived from the ρZ projection method to calculate the effective atomic number and surface density of structures from their dual-energy X-ray images.

- A materials discrimination method for multi-layered structures termed the 'W-E technique'. The technique enables the depth segmentation of multi-layered structures in terms of surface density and effective atomic number. The technique comprised of a mass subtraction equation to compute the surface density of overlapping regions and a weight fraction method to extract the effective atomic number. This technique is limited to well-behaved layers, which do not fully occlude the target material.

- A laminographic estimation method to compute the thickness of an imaged structure in multiple-view dual-energy X-ray image sequences and hence enabling the computation of its mass density.

- A materials discrimination image encoding scheme employing four hues. This is designed to highlight a 'threat window' in materials space to enhance the visual detection and identification of threats.

- A methodology to inform and apply the above contributions to the design of a novel materials discriminating (colour) kinetic depth X-ray (KDEX) imaging technique.

1.4 Structure of the report

This report consists of six chapters:

- Chapter One Introduction: presents the background, scope and objectives of the thesis.

- Chapter Two Enabling technologies and theoretical considerations: presents an introduction to various X-ray discrimination techniques, overview of the existing materials discrimination approaches and X-ray imaging techniques, and is followed by an introduction to relevant aspects of human vision and colour space.

- Chapter Three System calibration and standard colour encoded multiple-view X-ray image generation: presents a calibration of the real-time X-ray machine which involves dual-energy spectra generation, collimation, and filtering, and a detailed description of the generation of multiple-view X-ray images and industry 'standard' materials discrimination colour encoding schemes.

- Chapter Four Materials discrimination: presents the developed algorithm and supporting methodology of the K-II technique and W-E technique, and reports the experiment results and analysis of the K-II technique and W-E technique for materials discrimination.

- Chapter Five Thickness estimation and colour encoding of discriminated materials information: presents the developed algorithm and supporting methodology for the thickness estimation by considering laminographic data, and reporting the experiment results and analysis of the thickness estimation. Also a new colour encoding scheme, derived from and building on the

'standard' industry colour scheme, is presented to support the additional information provided by the K-II technique and W-E technique.

- Chapter Six: Summary, Conclusions and Future work: summaries the work completed, presents the conclusions and proposes the direction of the future work.

CHAPTER TWO: ENABLING TECHNOLOGIES AND THEORETICAL CONSIDERATIONS

2.1 Introduction

This chapter provides background information for materials discrimination employing the multiple-view dual-energy X-ray image data collected from a real-time VTX-160 X-ray machine. Central to this investigation is the extraction of material's effective atomic number [32], mass density, and the thickness along the X-ray inspection path. This data is extracted from the resultant multiple-view dual-energy X-ray images. The discussion is divided into the following five broad areas:

- X-ray attenuation;

- dual-energy X-ray materials discrimination;

- X-ray imaging;

- human vision;

- colour models.

2.2 X-ray attenuation

X-rays [33] [34] [35] were discovered by Wilhelm Conrad Röntgen (1845-1923), a German physicist, on the 8th November 1895. X-rays are produced by energy conversion when fast moving electrons from a filament interact with a target (anode). Due to their short wavelength (10^{-8} to 10^{-12} m), X-rays can pass through objects, which are normally opaque to ordinary light, and shadow images of internal structures can be made visible on a fluorescent screen. X-rays are widely used in security inspection applications, as well as medical imaging and NDT and E.

Attenuation is the reduction in the intensity of an X-ray beam as it transverses matter by either the absorption or scattering of incident photons. Four factors dictate the degree of attenuation, which is governed by the exponential attenuation law [36] [37][38]:

$$I_x = I_i \times \exp[-m \times (Z, r : E) \times d],$$ Equ 2-1

where Ix is the transmission intensity; Ii is the incident intensity; μ is the linear attenuation coefficient of the material, which is a function of effective atomic number Z_{eff} and mass density r and energy of the incident X-ray photons E; and d is the thickness of material along the X-ray inspection path. In general, increasing the effective atomic number, mass density and thickness of the material increases the total attenuation, while increasing the energy of the incident photons decreases the total attenuation [39]. *Fig. 2.1* illustrates the total mass attenuation coefficient for lead as an example [40].
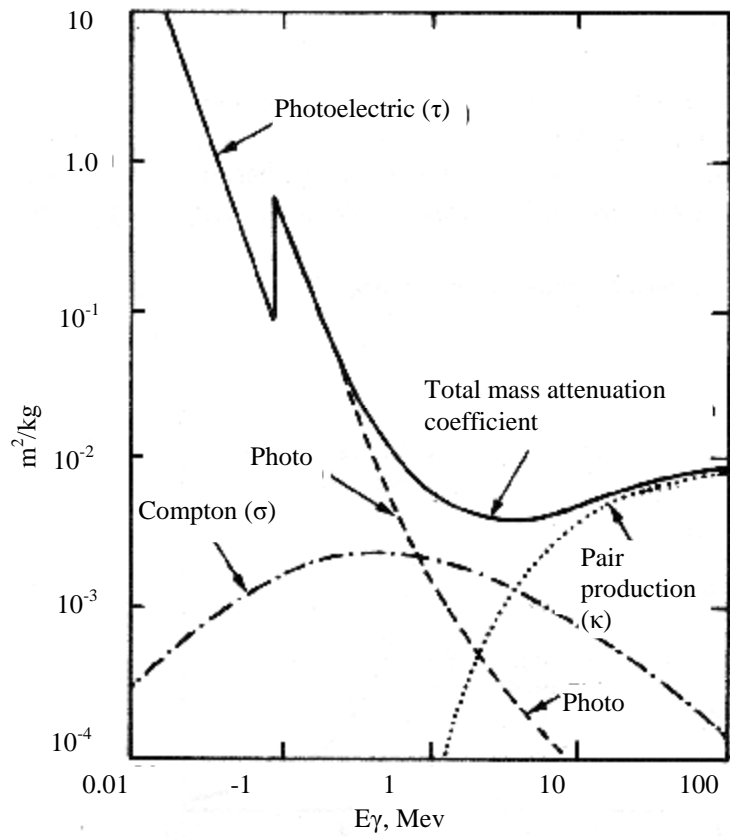
Fig. 2.1. Total mass attenuation coefficients for lead.

2.3 X-ray materials discrimination

Over recent years, many sophisticated methods have been tried on detecting explosives in airport security screening task. These methods included nuclear techniques such as thermal neutron analysis, fast neutron analysis and pulsed fast neutron analysis [3]. These detection techniques explore the high penetration power of neutrons and their interaction with nitrogen-rich explosives such as TNT, C-4 and Semtex. Although nuclear techniques have the potential to provide high precision multi-elemental identification, they produce poor resolution results and a high false alarm rate. This is because many other innocuous nitrogen-rich materials such as wool, nylon and leather may trigger the alarm. Also electromagnetic techniques such as magnetic resonance

imaging, quadrupole resonance analysis and microwave imaging have been tried [3]. These techniques exploit the effect of the electromagnetic properties of atoms and molecules on radio frequency response. However, the primary limitation of these techniques is the incapability of detecting materials enclosed in a metal container due to the field distortion produced by metallic objects. In addition X-ray scatter techniques have been incorporated into commercial systems. Unique crystalline structure of explosive or drugs can be identified by the coherent scattering technique to measure the resolution, energy and intensity of the diffraction pattern [41]. The effectiveness of the technique relies on the extensive compilation of reference patterns for all threat substances [41]. Also, in practice, the attenuation from overlapping objects can cause a loss of detected information. All these technologies are designed to detect the presence of explosives and do not produce conventional image data [19].

Despite the advance of these technologies, the problem of reducing false alarms remains unsolved. The problem of false alarm rates (or false positives) is compounded by the unique nature of each luggage item inspected and the fact that the full member set of target categories (e.g. explosives, guns and knives) cannot be defined. The existing dual-energy X-ray technologies are capable of detecting Z_{eff} with high accuracy. However, they do not convey useful volumetric information (i.e. thickness) to determine material density. Thus, dual-energy analysis is unable to isolate innocuous organic objects (e.g. clothing) from threat objects (e.g. plastic explosives) as their correct classification is largely determined by density (see *Fig.2.3*). It should be noted that the grey patch in *Fig.2.3* is an indicative guideline adopted by the aviation screening industry to discriminate explosives from harmless materials that commonly appear in travellers' luggage. In theory, materials can be synthesised to have the same Z_{eff} and density as explosives so that these materials lie in the grey patch and hence trigger the false alarm. However, in practice, this is unfeasible with current technology. Numerous efforts have been put forward by the aviation industry to fabricate quality explosive stimulant by using harmless materials. Explosive stimulant is perceived as a powerful device for system evaluation and operator training. However, thus far, these efforts have not yet been properly rewarded. The closer the density of the stimulant to real explosive, the higher the chance of the stimulant to behave like explosive. Hence,

explosion is likely to occur during the fabrication process. The regulation bodies have stringent guideline for the industry to avoid catastrophe. The above sentences highlighted the fact that explosives require certain density to cause the explosion. So, the attempt to deceive the explosive detection system by reducing the density of the explosives may not be as rewarding as it intended [3, 19]. False alarm rates of the order of 20-percent present serious logistical problems for high-volume and fast-stream airport environments.

In order to tackle this problem, a multiple-view dual-energy X-ray technique based materials discrimination method is introduced in this research. The multiple-view imaging technique provides depth information for mass density extraction to improve the capability of materials discrimination. The aim of dual-energy radiography is to provide information about the material parameters which includes material effective atomic number and mass density. It is important to note that Z_{eff} and ρ present completely different properties. The mass density $\rho=dm/dV$ describes the mass distribution, i.e., the morphology of the absorber. The Z_{eff} refers to the average atomic number of the hypothetical single element which produces the same X-ray attenuation as a compound being measured [42] [43]. For pure material, it exactly matches the atomic number, e.g., $Z_{eff} =13$ for Aluminum. Summarising, Z_{eff} describes chemical classification and ρ represents physical morphology of the absorbing material [15]. Material parameters can be appreciated from a material map for various materials as illustrated in *Fig. 2.3* once it is determined.
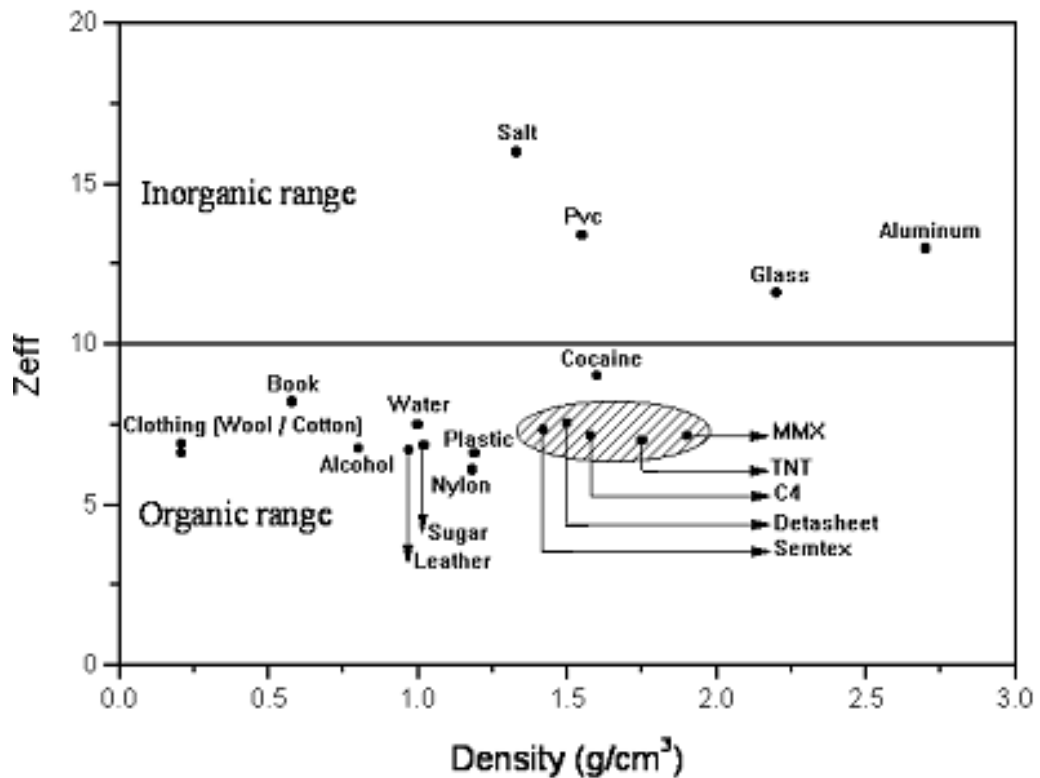
Fig. 2.3. The material map for common items found in airport luggage and for cocaine and some explosive materials [11].

Ideally, materials can be discriminated by two energy independent constants which can be provided by X-ray beams comprised of X-rays at two different energy levels 75 *keV* and 150 *keV*, respectively. Material parameters can be obtained from the measurements of the change in the transmitted low energy and high energy X-ray spectrum detected by the dual-energy X-ray sensors. The two energy independent constants characterises the integrated Compton scattering and photoelectric attenuation coefficients. Alverez and Macovski state that, above the k-edge, the total linear attenuation coefficient of a given material for photon energies in the X-ray range of 30-200 *keV* may be expressed approximately as a linear combination of Compton and photoelectric interaction coefficients [13][44][45][14][46][47] which is shown in *Equ 2-4*. Rayleigh scattering is not considered in this research, because it is only important in low energy photons and

its total quantity is too small to be important for the high X-ray energy (~140 *keV*) [48] considered in this programme of work.

$$I_x = I_i \times \exp[-(a \times s_{pe} + b \times s_{cs}) \times r \times d],$$ Equ 2-4

where *Ix* is the transmission intensity; *Ii* is the incident intensity; α and β are constant; ρ is mass density; *d* is the thickness along X-ray inspection path; σ_{pe} and σ_{cs} are Photoelectric absorption and Compton scattering respectively.

In this research programme, polychromatic radiation is utilised to accommodate the practical requirements of the industrial baggage screening, image processing and decision analysis required to be accomplished in approximately 6 seconds per luggage item [3]. The attenuation function in polychromatic radiation can be presented as *Equ 2-5*.

$$I_x = I_i \times \int S(E) \times \exp[-(a \times s_{pe} + b \times s_{cs}) \times r \times d]dE,$$ Equ 2-5

where *S(E)* is spectrum produced by a polychromatic X-ray source and *E* is the energy of the incident X-ray photon. In practice *Equ 2-5* incorporates higher order terms modelled by polynomial functions, to compensate for X-ray beam hardening effect [49] which increases as the thickness of the irradiated substances increases. A general form of polynomials of 2nd and 3rd order has been widely used to compensate for these effects [13][44].

2.3.1 Materials discrimination curves

The materials discrimination curves, which are produced by signals from the high energy and low energy detectors, can be employed to discriminate organic, mixture and metal substances [50][51][52]. The organic compounds are defined generally as consisting of elements that with effective atomic number of 10 or less, the mixture materials are defined as being comprised of elements have effective atomic number between 10 and 20, while the metal substances are defined as having effective atomic

number greater than 20 [3]. The materials discrimination curves, also known in the industry as 'banana curves', are employed to produce colour-coded images from the conventional monochrome X-ray images to assist discrimination. The difference between *High* and *Low* signals is a measure of the materials discrimination which is obtained from the dual-energy X-ray detectors. The material properties are determined by comparing the relative attenuation of the *Low* beam (~80 *keV*) and *High* beam (~140 *keV*). Materials discrimination curves for organic, mixture (a mixture of organic and metal materials) and metallic materials are shown in *Fig. 2.4*. The industry standard colour palettes, as illustrated in *Fig. 2.5*, are employed to colour encode X-ray images based on the banana curves, *High* and *Low* signals produced by dual-energy X-ray inspection. Typically organic, mixture and metallic materials are displayed as orange, green and blue colour, respectively. This colour encoding scheme provides a general indicator of materials such as plastics, paper, explosives and narcotics but is by no means a precise definition. Nonetheless, security X-ray screening systems utilising dual-energy materials discrimination are widely deployed in the major airports throughout the world.
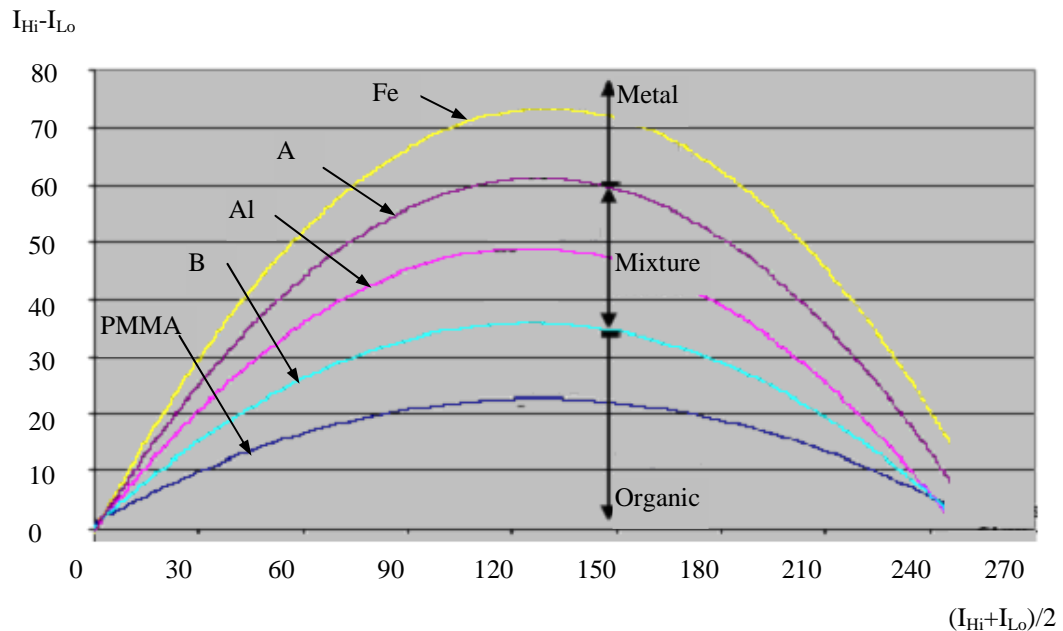
Fig. 2.4 Materials Discrimination Curves.
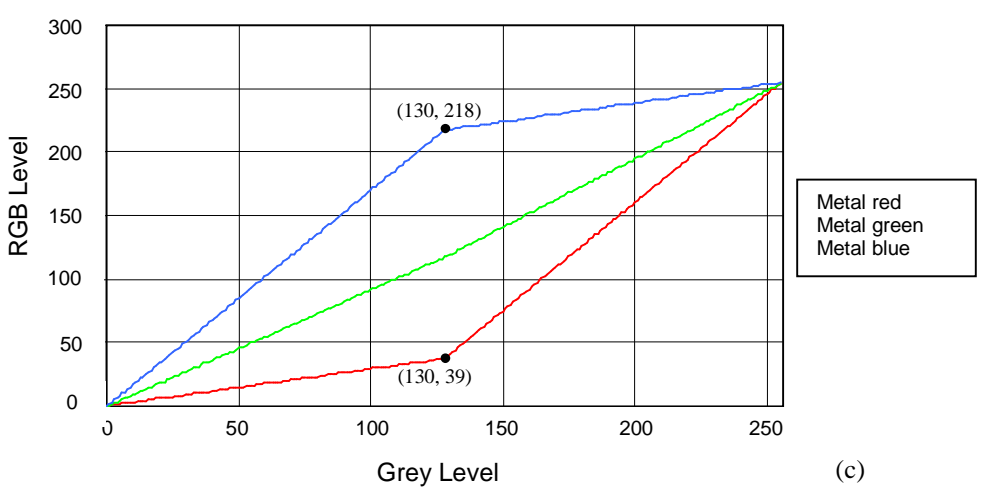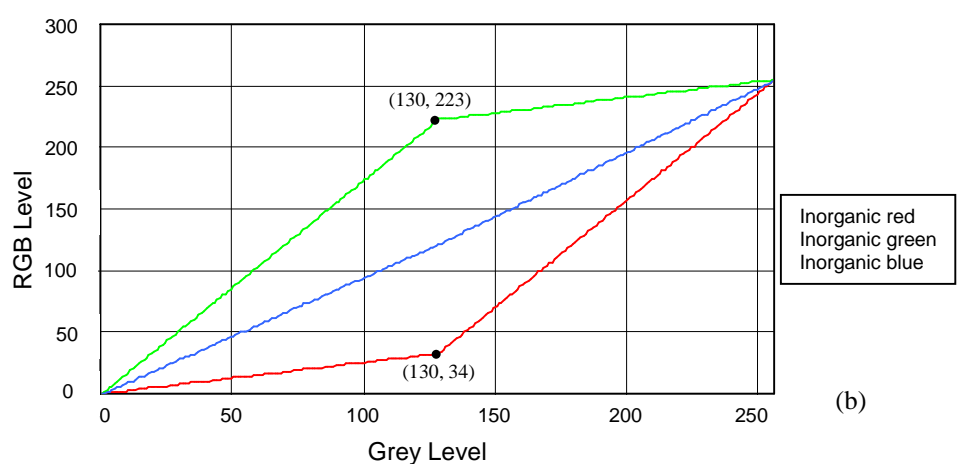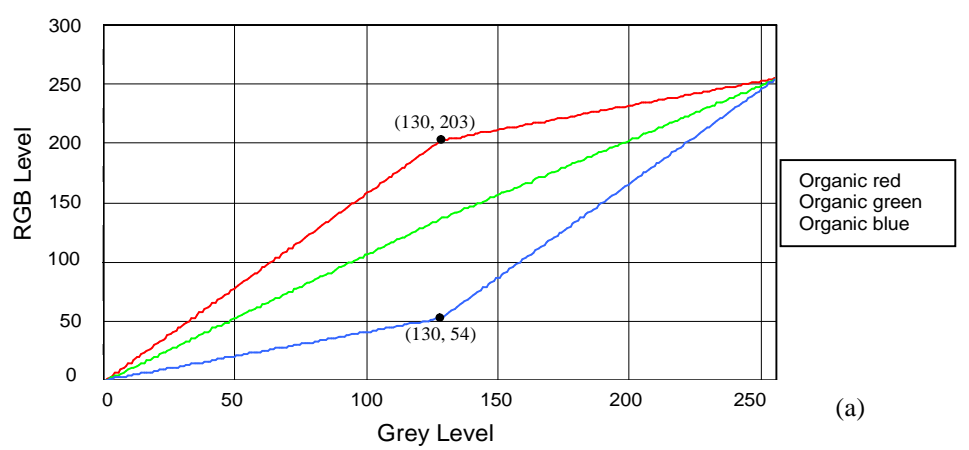
Fig. 2.5. Graph of the 'standard' industry colour palette for (a) organic substances, (b) mixture substances, and (c) metal substances [3].

2.3.2 Basis materials subtraction (BMS)

BMS techniques have been developed in prior research by the university team. This approach enables the characteristic angle from overlapping materials to be extracted [53]. The BMS technique is a derivative of the basis materials decomposition (BMD) [54] technique. It is capable of extracting the two energy independent constants (i.e. d_1 and d_2) that characterises the integrated photoelectric and Compton scattering attenuation coefficients from layers of overlapping substances. Consequently, the characteristic angle θ (i.e. $\tan^{-1}[d_1/d_2]$) for the attenuated material can be obtained. The equivalent basis materials thickness d_1 and d_2 for any materials are computed by utilising the direct approximation method [44] which is shown in *Equ 2-7* and *Equ 2-8*.

$$d_1 = a_0 + a_1 T_L + a_2 T_H + a_3 T_L T_H + a_4 T_L^2 + a_5 T_H^2 + a_6 T_L^2 T_H^2 + a_7 T_L^3 + a_8 T_H^3, \quad \text{Equ 2-7}$$

$$d_2 = b_0 + b_1 T_L + b_2 T_H + b_3 T_L T_H + b_4 T_L^2 + b_5 T_H^2 + b_6 T_L^2 T_H^2 + b_7 T_L^3 + b_8 T_H^3, \quad \text{Equ 2-8}$$

where a_i and b_i are coefficients, T_H and T_L are the logarithmic transmission value (i.e. $T_H = \ln(I_x/I_i)_H$, $TL = \ln(I_x/I_i)_L$). The direct approximation equations are calibrated using the aluminium (*Al*, $\rho = 2.7$ g/cm^3, Zeff=13) and plastic (*Pl*, $\rho = 1.4$ g/cm^3, Zeff =6.6) step wedges with various known thickness combinations, see in *Fig. 2.6*. The coefficients a_i and b_i are determined by using *Levenberg-Marquardt* [55] polynomial least square fitting algorithm. For a target material, equivalent basis materials thickness d_1 and d_2 can be calculated by applying the calibrated direct approximation method. Any material which has an effective atomic number lying between 6.6 and 13 can be discriminated by representing its effective atomic number as a characteristic angle $\theta = \tan^{-1}[d_1/d_2]$ which has a range between 0° to 90°. Ideally, plastic material would have a characteristic angle 0° and aluminium material would have a characteristic angle 90°. However, The BMS technique is unable to discriminate the materials which have an effective atomic number either greater than 13 or less than 6.6.
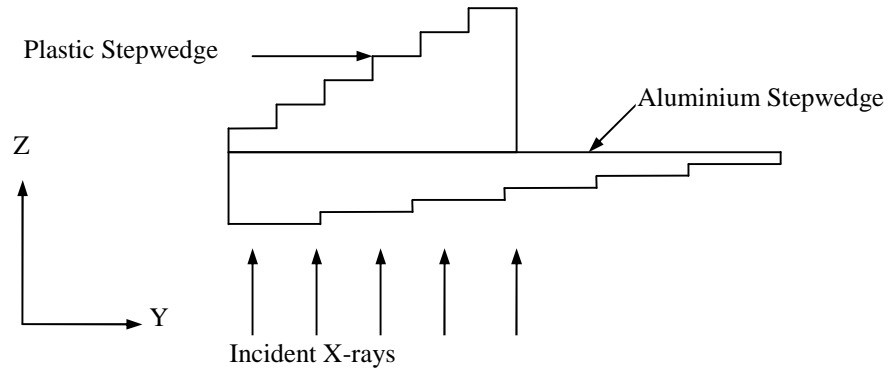
Fig. 2.6 The arrangement of Al and Pl stepwedges for the calibration of the direct approximation method.

2.3.3 ρZ projection method

The *ρZ* projection method was reported by B. J. Heismann, J. Leppert, and K. Stierstorfer in August, 2003 [15]. It enables the computation materials of an effective atomic number and mass density directly according the image data obtained from computed tomography (CT) data. With a given measurement of the X-ray tube spectrum *S(E)* and the detector sensitivity *D(E)*, 0<*D(E)*<1, the effective attenuation coefficient is

$$m = \int W(E) \times K(E) dE ,$$

Equ 2-9

where the weighting function

$$W(E) = \frac{S(E) \times D(E)}{\int S(E) \times D(E) dE} ,$$

Equ 2-10

and *K(E)* function

$$K(E) = a \times r \times \frac{Z^k}{E^l} + b \times r ,$$

Equ 2-11

where *α*, *β*, *k*, and *l* are what constant, ρ is mass density, Z_{eff} is effective atomic number, and *E* is energy. For the numerical fits of experiment data, *k* is between 3 and 4 and *l* between 3 and 3.5. An approximation is made to *Equ* 2-9 as the thickness in the CT image is very small. Analysing dual-energy CT image data, material parameters can be obtained from

$$Z = (m_1, m_2),$$
Equ 2-12

and

$$r = (m_1, m_2),$$
Equ 2-13

where μ_1 and μ_2 are the effective attenuation coefficient of high and low energy X-ray scanning respectively. The contour plot of Z_{eff} and ρ is shown in *Fig. 2.7*. The absolute precision of mass density is 20 mg/cm^3 and the absolute precision of effective atomic number is 0.1 [15][56]. It is concluded that the ρZ projection method provided a further class of precise information for quantitative X-ray applications. However, the ρZ projection method is only applied and tested by using CT X-ray image data. The factor of material thickness is ignored by an approximation as the CT image is in slice format.
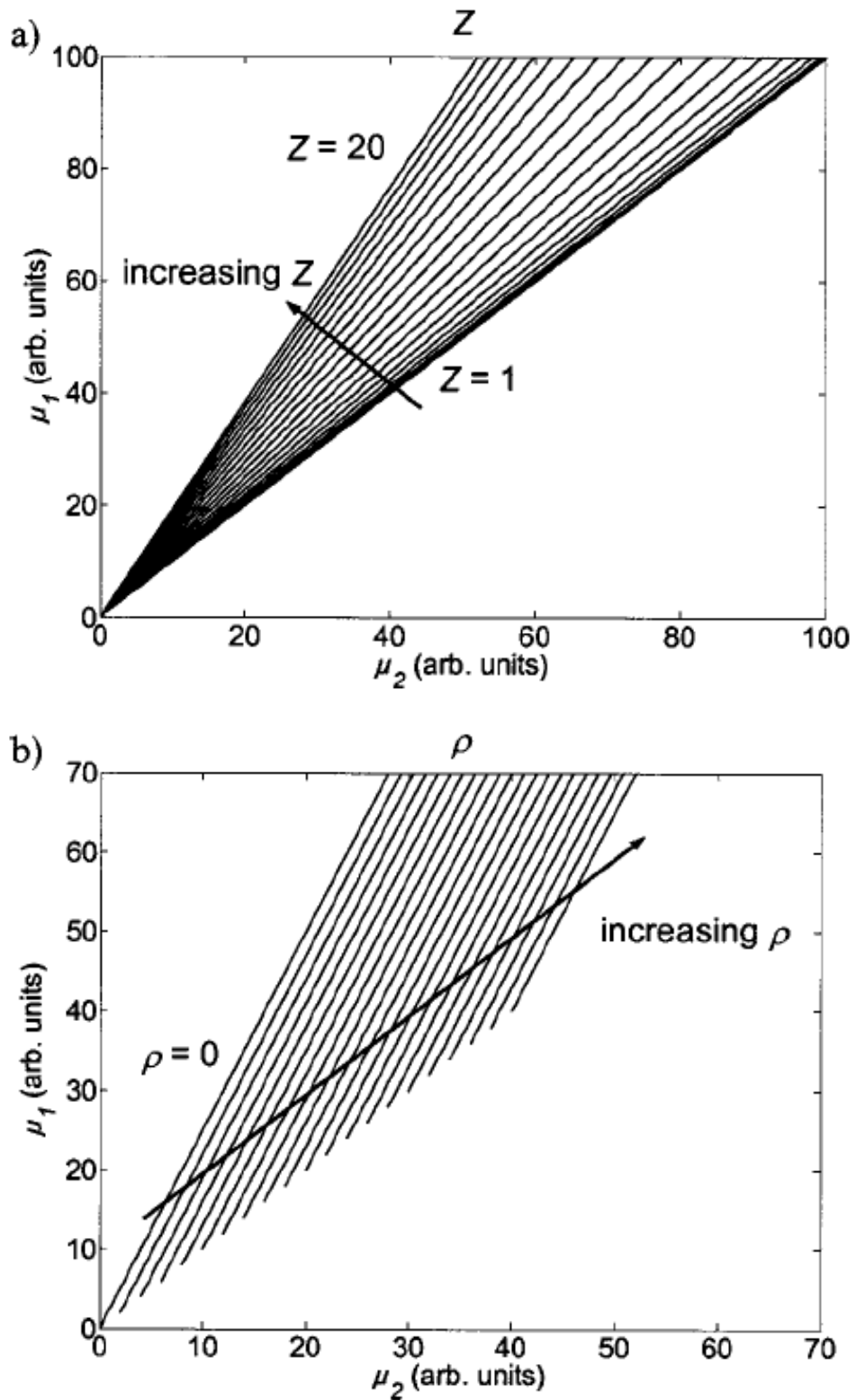
Fig. 2.7. Contour plot of the analytic ρZ projection method (a) shows Z=contants and (b) shows ρ=constant as function of μ₁ and μ2 [15].

2.4 X-ray image production and processing

Stereoscopy was introduced to radiology by J. Mackenzie Davidson in 1898 [57]. The application of stereoscopy in X-ray imaging originated from the operating principle of the human visual system [58][59][60][61][62][63]. Binocular parallax is one of the most robust depth cues utilised by a human observer [64][65]. This cue can only exist when the observer's eyes are focused and converged onto an object producing a conjugate image point on the retina of each eye. A binocular stereoscopic X-ray screening technique [30][31] has been developed by the university team which enhances the observer's understanding of the true nature of the three-dimensional scene under observation. Multiple-view X-ray imaging technique have also been developed to combine the binocular stereoscopic visual cue with motion parallax cue [66][67]. The relative movement or rotation of an object produces a vivid sensation of depth for the observer.

2.4.1 Dual-energy X-ray imaging

Dual-energy X-ray imaging requires the production of two X-ray images taken at different energy levels thus characterising the integrated effects of photoelectric absorption and Compton scattering [14][68][69][70][71][72]. Photoelectric absorption contributes to the X-ray beam's attenuation by absorbing the incident photons and is the predominant interaction in the low range energy from 1 to 100 keV. The probability of this interaction occurring is characterised by the photoelectric cross section, s_{pe} as follows:

$$s_{pe} \ a \ \frac{Z^n}{E^3},$$

Equ 2-2

where Z_{eff} is the effective atomic number of the atom; E is the energy of the incident X-ray photon; and exponent n is between 3 and 4 [73]. The Compton scattering is responsible for bulk scattering effects in radiography when an incident photon collides with a "free" outer-shell electron. The probability of Compton scattering is a function of

the number of electrons available for the scattering targets and generally increases linearly with the atomic number:

$$\boldsymbol{s}_{cs} \propto Z_{eff} \, .$$
<div align="right">Equ 2-3</div>

High atomic number, Z_{eff} materials absorb low-energy X-ray photons more significantly while low-Z materials scatter high-energy X-ray more significantly. This relationship can be appreciated from *Fig. 2.8*.
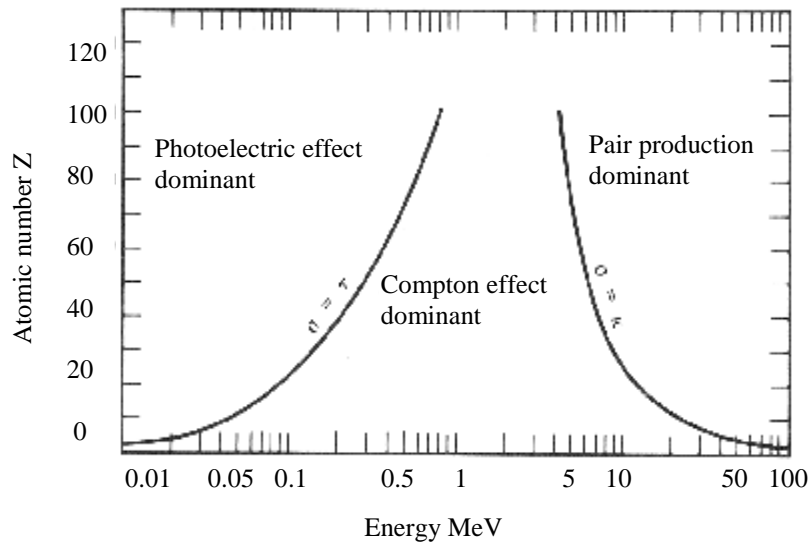
Fig. 2.8. The Relative Importance of the Three Major Types of X-ray Interaction [36].

Low-Z materials such as explosives can be distinguished from high-Z materials such as metal by appropriate treatment of the X-ray signals obtained at different energy levels.

2.4.2 Multiple-view X-ray imaging

A special case of motion parallax termed the kinetic depth effect or KDE was first systematically investigated by Wallach and O'Connel in 1953 [8] and is an adoption from the previous work reported by Miles [74] and Metzger [75]. This effect involves the recovery of three-dimensional information from a sequence of two-dimensional

silhouettes. The resultant depth effect is compelling and the observer can work out the shapes of certain objects with remarkable accuracy from the shadows during a full or partial rotation. However, in the KDE the direction of depth is inherently ambiguous, since the direction of perceived depth may change spontaneously, even though there is no physical change in the stimulus. Binocular disparity tends to disambiguate the depth produced by motion parallax and KDE. In principle, this new imaging technique is equally applicable to both standard monochrome X-ray imaging and dual-energy X-ray imaging. The depth from motion or KDEX imaging technique is designed to meet a number of critical operational constraints for airport luggage security screening. It is envisaged that the technique would have no impact upon the speed of the conveyor belt or the standard functionality that is currently available on the conventional two-dimensional (2D) X-ray machines. The two X-ray source/sensor configurations which are utilised for line-scan multiple-view X-ray image collection are illustrated in *Fig. 2.8.*
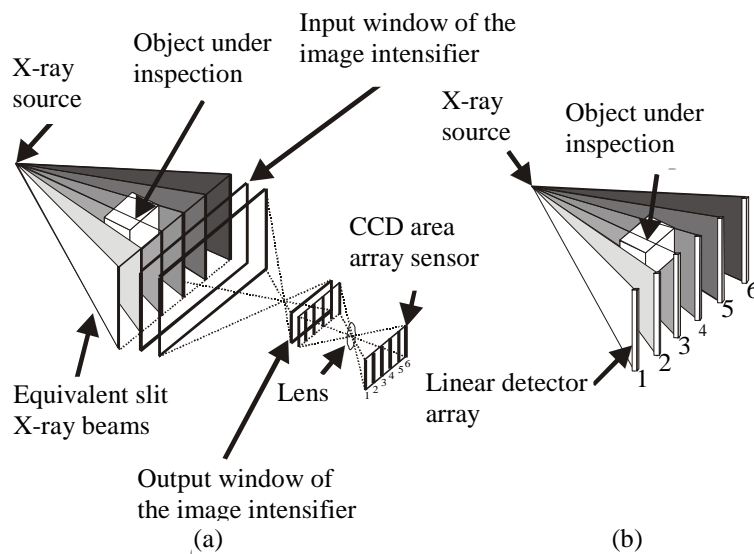
Fig. 2.8. Line-scan multiple-view image collection geometry utilising (a) image intensifier X-ray system (b) linear X-ray detector array system [27].

It is useful to draw a distinction between KDEX and computed tomography (CT) technology. CT technology produces volumetric views of the object under inspection by

integrating a stack of contiguous slice images or tomograms [76][77][78]. The success of CT systems rely on complex and bulky mechanical constructions such as a slip ring to provide data signals (and power to the X-ray tube) to flow between the continuously rotating gantry and the stationary CT components, through the electrical, radio frequency or optical connections on the slip ring (Hsieh, 2003). With increasingly demanding scan speeds, the mechanical requirements on the gantry increase because the centrifugal force increases with the square of the rotation speed. Note that CT components mounted on a gantry can weigh of the order of a hundred kilos or more. The purchase and running costs of commercial CT scanners are estimated to be at least an order of magnitude greater than anticipated for the KDEX technology. Thus the KDEX technique could offer a significant improvement to the existing 2D technology but at the fraction of the cost, bulk and radiation exposure associated with CT. It is not suggested that the KDEX could replace CT per se but rather that it has the potential to replace 2D technology with a cost effective 3D imaging technology [7].

2.4.3 Laminography

Laminography is introduced as a technique to image objects layer by layer, producing cross sectional images (laminograms) of selected planes within the object [79]. The distance between successive laminograms conveys the depth information of the inspection volume. While the quality of laminograms may be high, they are fundamentally different from tomograms produced by the CT technique. However, laminography requires only a limited range of inspection angles to offer a relatively faster solution to the extraction of depth information, which tends to favour its application in airport screening applications. In this research programme, the extracted depth information enables the computation of the object thickness, which is essential for determining its mass density.

Laminography requires a coordinated motion of any two of the three imaging components i.e., X-ray source, object and detector. Examples of the coordinated motion are, but not limited to, linear translation, circular and elliptical. *Fig. 2.9* (a) and (b)

illustrate the imaging geometry of the rotational laminography and linear translational laminography. During an imaging cycle, the coordinated motion enables the images of a point in a particular object plane (or depth plane) to have a fixed position on the detector plane, while any point outside the object plane will be projected at different locations. In this manner, only the depth plane of interest appears in focus in the resultant images with other depth planes contributing to image blurring.
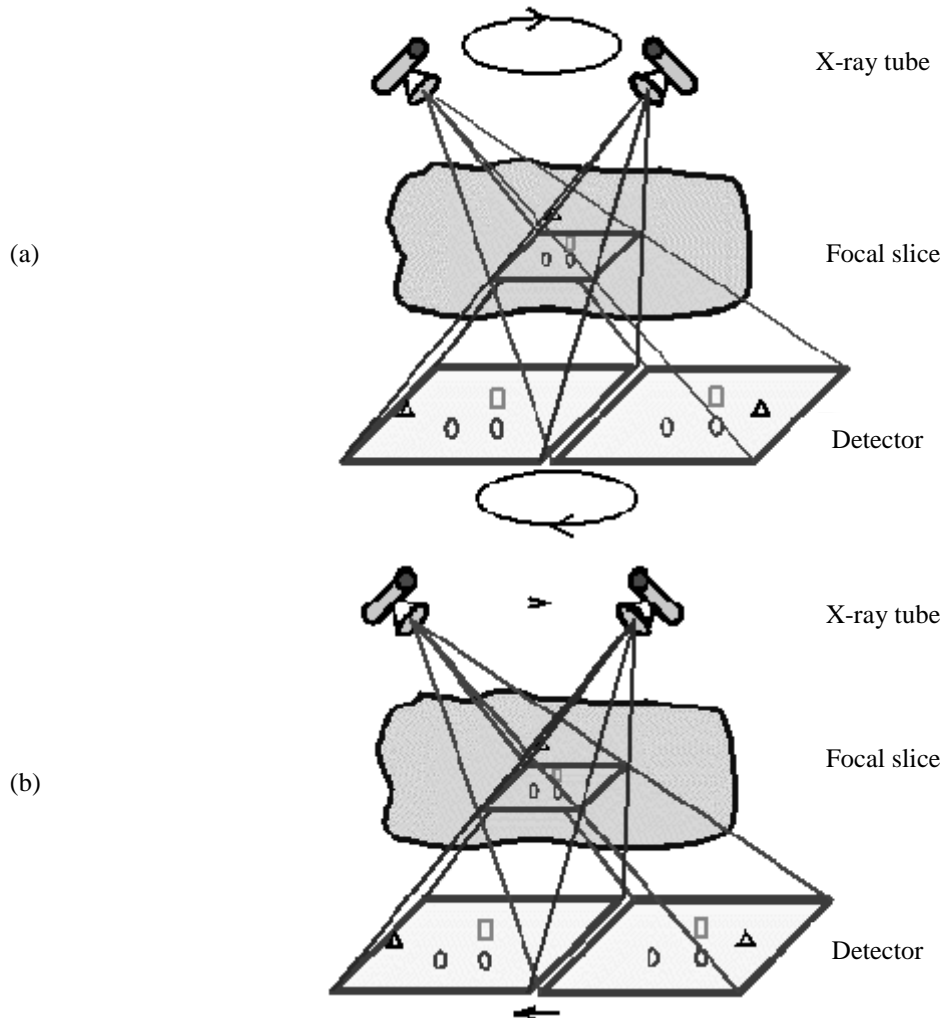
Fig. 2.9. Laminography techniques (a) rotational, (b) translational [79].
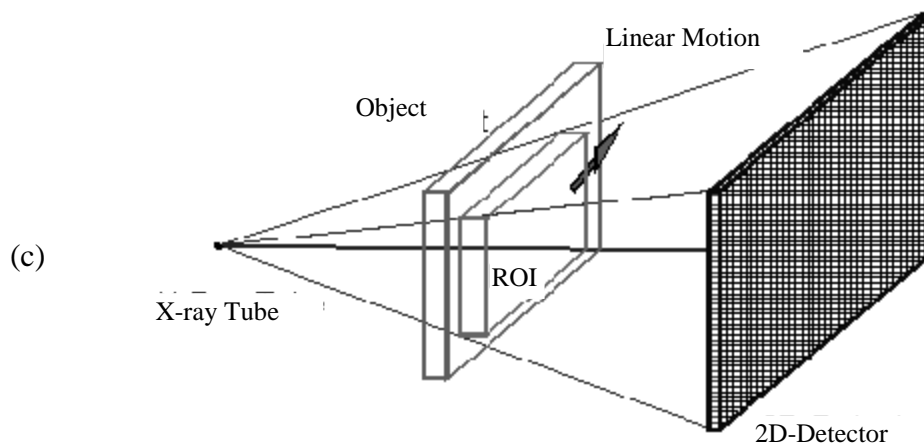
Fig. 2.10. Computed laminography technique [79].

The Fraunhofer Institute Nondestructive Testing IZFP has developed the computed laminography (CL) technique. The technique involves only a linear translation of a object through the cone beam of the X-ray source [80][81] while keeping both X-ray source and detector remain stationary as shown in *Fig. 2.10*. So it becomes very simple to examine large objects that normally cannot be easily examined with classical laminography due to complicated system engineering. During the movement, the object is irradiated by the X-ray beam at different angles. This allows the detector to acquire successive information of a given volume element (voxel) of the object under consecutively changing angles. These 2D area-scan projections contain the structure information from all object slices. In comparison with the classical approach described in *Fig 2.9*, the projection values simply have to be sorted and added correctly in order to obtain a desired cross sectional image.

While both CL and KDEX techniques involve using a stationary source/detector configuration and the linear translation of the objects, these techniques are very different. The former acquires 2D area-scan X-ray images from the footprint of the X-ray cone beam. However, the latter utilises a set of collimated X-ray fan beams to produce 2D line-scan X-ray images. Comparatively, the resultant images of the KDEX technique exhibit better contrast due to scatter removal by the collimation. Also the line-scan imaging allows, in theory, scanning an infinitely long object. The appropriate

processing on the transmitted X-ray images acquired by the KDEX technique can generate a set of laminograms. The distance between successive laminograms (i.e., depth increment) is determined by the voxel [27] created by the overlapping field of adjacent views, as illustrated in *Fig. 2.11*. The angle of separation between two adjacent views is s and δX is the sample size along the motion axis (X-axis). The depth increment ΔZ can be expressed as:

$$\Delta Z = \Delta X / \tan(\frac{s}{2}).$$ Equ 2-14

The equation signifies that large s and small ΔX are required to achieve the best measurement capability in the depth axis [82][83].
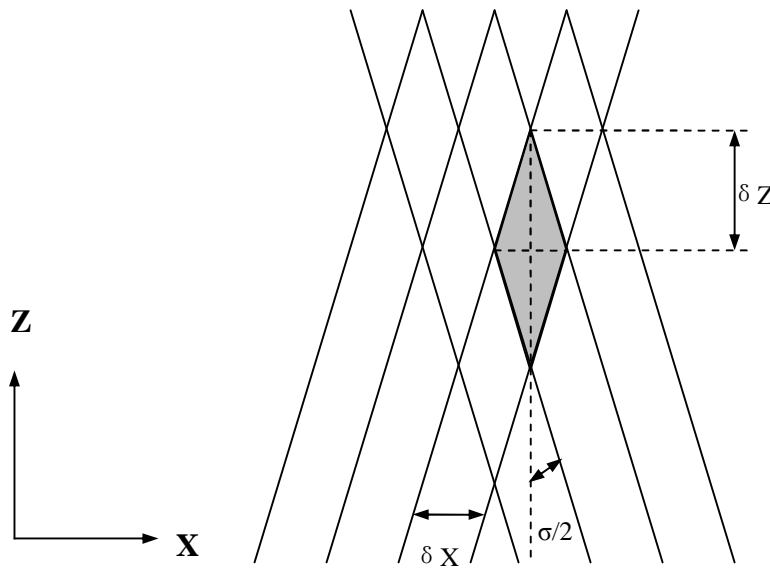
Fig. 2.11. The image geometry of a voxel.

2.4.4 X-ray image segmentation

The critical problem for the detection of target materials like plastic explosives is the requirement to resolve each layer of the materials present in the baggage. The problem is accentuated for complicated arrangements of overlapping objects routinely encountered in security screening application. Therefore, pre-processing procedures such as segmentation require to be applied to reduce the overlapping objects into smaller and more manageable regions (i.e., homogeneous grey level areas). Image segmentation [84][85][86] is the splitting of an image into a set of connected regions based on features (e.g. pixel intensity). Normally, image segmentation techniques can be divided into three groups: thresholding, edge detection, and region extraction [26].

Thresholding

Thresholding [87][88][89][90][91] had been widely used in image segmentation and widely reported in the literature[92][93]. Global or histogram-based algorithms [94][95][96][97] are the most commonly used as these technique are simple and computationally fast. This approach is based on the assumption that each distinctive feature in an image can be represented by an approximately hill-shaped distribution in the grey-scale histogram. Therefore, appropriate thresholding of the image histogram can be employed to segment the original image.

Edge Detection

Edge-based methods utilise the concept of discontinuity to highlight boundaries between adjacent structures. The edge elements can be extracted by employing a variety of edge detecting operators [98][99][100][101]. This process may be followed by thresholding of the edges detected produce a resultant binary image. However, in practical images the selection of the edge threshold values is often problematic. At low threshold values there is often a high value of continuity resulting in relatively thick edges, while at high threshold values the continuity tends to decrease producing thinner edges [102], as illustrated in *Fig. 2.12*. Finally, the threshold edge elements may be

combined to form edge chains which may be labelled and converted into image segments.

X-ray image

Edge detected image

Edge detected image employing a low threshold value of 5

Edge detected image employing a high threshold value of 30

Thick edge with high continuity

Thin edge with low continuity
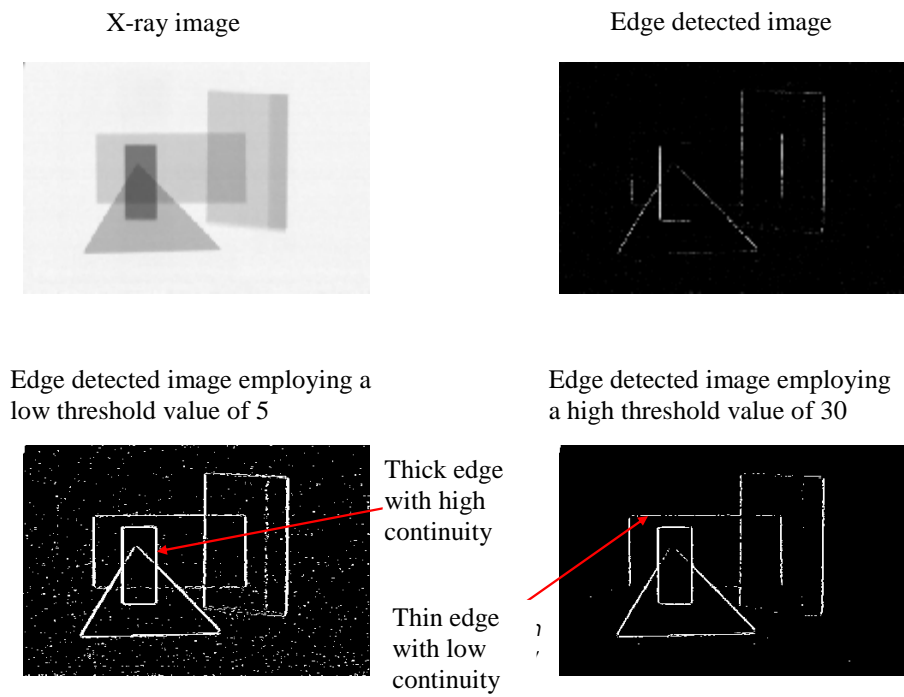
Fig. 2.12. Comparison between low value thresholding and high value thresholding for edge detection [26].

Region Extraction

Region-based methods generally perform better for noisy images where edges are difficult to detect. There are three basic approaches to region identification: region merging, region dividing, and a combination of region merging and dividing. All of the region-based methods are iterative in approach and computationally intensive. Therefore, in general these methods are not popular.

2.5 Human vision

Humans can distinguish around ten million different colours [103]. The cornea and lens acting together form a small inverted image of the outside world on the retina which is

the light-sensitive surface of the eye. The individual cones and rods on retina transmit signals to the brain through nerve fibres in different ways [104][105]. In each eye, there are about 130 million rod cells and 7 million cones. The light sensitivity of rod cells is about 1,000 times that of cone cells. Cones consist of three cell types termed ρ, γ and β cones and exhibit peak for sensitivities to wavelengths around 580 nm, 540 nm, and 440 nm, respectively. One estimate of their relative abundances is that they are in the ratios of 40 to 20 to 1 for the ρ, γ and β cones, respectively [106].

When light is absorbed in a receptor in the retina, the molecules of the photosensitive pigment are excited, and, as a result, a change in electrical potential is produced. The pulses themselves are all of the same amplitude, and it is only their frequency that carries information to the brain. The frequencies involved are typically from a few pulses per second to around 400 pulses per second. Although, there are four different types of receptor, there is overwhelming evidence that there are not four transmitted signals along four different types of nerve fibre [107]. While much still remains unknown about the way in which the signals are encoded for transmission, the simple scheme shown in *Fig. 2.13* can be regarded as a plausible framework [104] for incorporating some of the salient features of what is believed to take place.
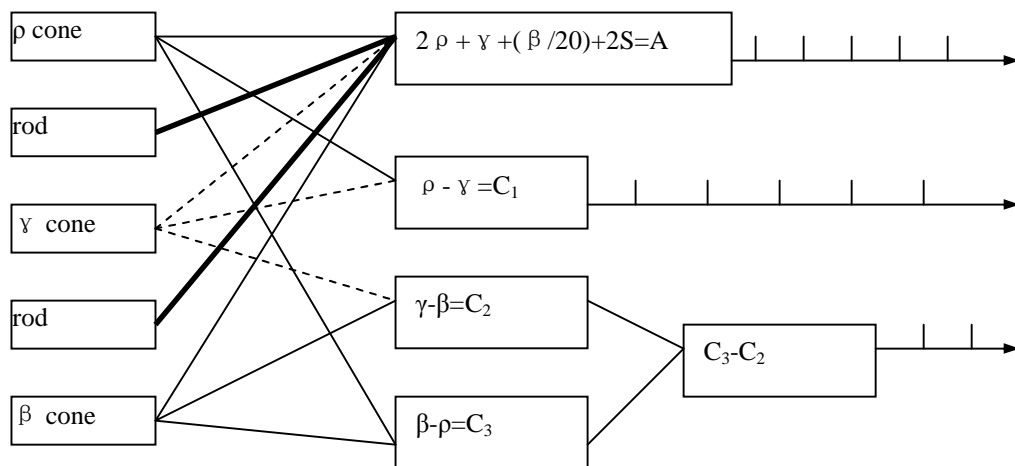
Fig. 2.13. Possible types of connections between some retinal receptors and some nerve fibres [104].

The signal from the cones is represented by the symbols, ρ, γ and β and signals from the rods is represented by the symbol S. Because of the different abundances of the ρ, γ and β cones, the cone part of the signals is represented as:

$$2 \times r + g + b/20 . \qquad \text{Equ 2-14}$$

Then, the total achromatic signal (A) is:

$$2 \times r + g + b/20 + 2S = A . \qquad \text{Equ 2-15}$$

The other two signals in the nerve fibres are usually referred to as colour difference signals. Three basic difference signals are possible between cones:

$$r - g = C_1 , \qquad \text{Equ 2-16}$$
$$g - b = C_2 , \qquad \text{Equ 2-17}$$
$$b - r = C_3 , \qquad \text{Equ 2-18}$$

In fact, there are various evidences to suggest that the signals transmitted resemble:

$$C_3 - C_2 = 2 \times b - (r + g) , \qquad \text{Equ 2-19}$$

Behavioural studies have shown the presence of well developed colour vision in various species; in many years, physiological experiments on these species have revealed signals of three general types that are broadly similar to the signals, A, C_1, and $C_3 - C_2$, proposed above. There are three basic perceptual attributes of colour: brightness, hue, and saturation (colourfulness). Brightness could depend on the strength of signal A, saturation could depend on signals such as C_1/A and $(C_3 - C_2)/A$, and hue is exhibited in colours possessing a hue when increased signals C_1 and $(C_3 - C_2)$ indicating the degree of the hue [108].

2.6 Colour models

Humans can only discern a few dozen grey levels dependent upon viewing conditions while capable of distinguishing thousands of colours [109]. The use of colour for human interpretation could improve the number of objects that can be distinguished. Colour also adds vivacity to images, which in turn decreases boredom and improves the attention span of screeners. Pseudo colouring of grey scale images is a typical process used as a means of supplementing the information in various fields including medicine, military, and several other data visualisation applications [110][111]. It is widely recognised that colour can contribute to reducing the time required to perform certain inspection tasks and lessens the probability of error due to fatigue and boredom. In security luggage screening, colour X-ray image can be divided generally into two groups. First, single energy X-ray luggage images tints with pseudo colours to highlight detected boundaries of objects [112][110]. Second, dual-energy X-ray data are processed to produce colour X-ray images containing materials discrimination information. Over the past decades, a number of colour models had been developed to accommodate the need for different applications. The selection of a colour model is application dependent. Colour models can be broadly categorised as device-based models and perceptual-based models [113]. For example, the RGB (Red, Green, and Blue) colour model is a device-based model while the HSI (Hue, Saturation, Intensity) colour model is a perceptual-based model. The research concentrated initially on the RGB and HSI models for the following reasons: (1) to continue prior research, which employed a RGB colour model to produce colour X-ray images as described in Section 2.3.1 and presented in *Fig. 2-13* and; (2) HSI colour model to investigate a more intuitive scheme to encode materials discrimination and X-ray intensity information [110]. Further elaboration of this reasoning is arranged in Section 2.6.2.

2.6.1 RGB colour model

The colour space for computer based applications is often visualised by a unit cube. Each colour (red, green, blue) is assigned to one of the three orthogonal coordinate axes in 3D space. An example of such a cube is shown below along with some key colours

and their coordinates. *Fig. 2.14* shows a colour representation of the RGB cube and coordinate plot of cube.
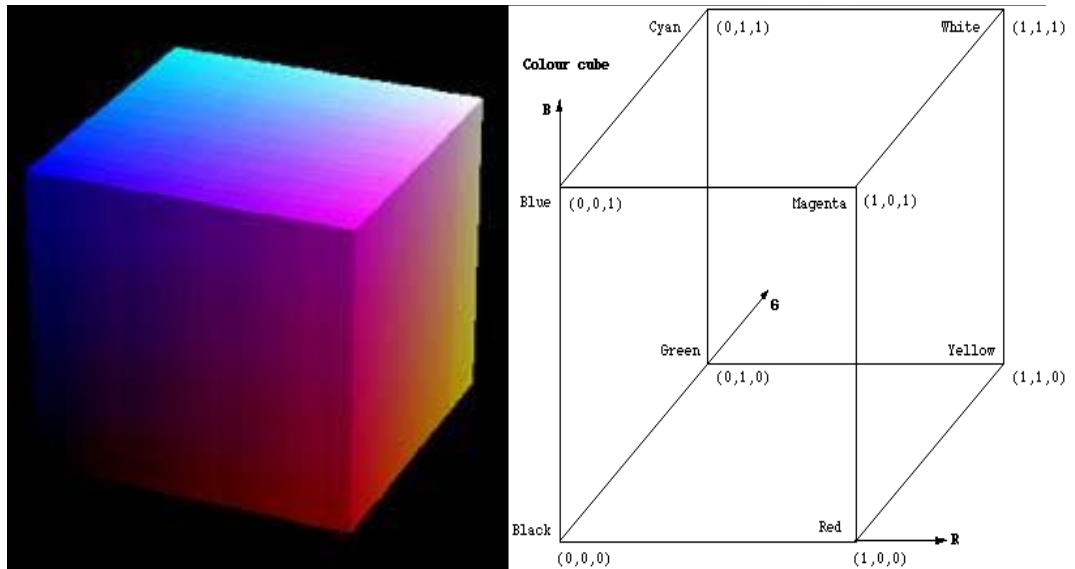
Fig. 2.14 Colour plot of RGB cube shell.

2.6.2 HSI colour model

The RGB colour model is ideally suited for hardware implementations because the distribution of these primary colours across the visible light spectrum produces wide-gamut colour images. However, the RGB and other similar colour models (e.g. CMYK) are not well suited for describing colours in terms that are practical for human interpretation. A human observer describes a colour by its hue, colourfulness (saturation), and brightness. Hue is a colour attribute that describes a pure colour, whereas saturation gives a measure of the degree to which a pure colour is diluted by white light. Brightness is the perception elicited by the luminance of a visual target. Unfortunately, brightness is a subjective descriptor which embodies the achromatic notion of intensity and it is one of the key factors in describing colour sensation. As

known, intensity is a most useful descriptor of monochromatic images. This quantity is definitely is measurable and easily interpretable. So, the model adopted in this research is the HSI (Hue, Saturation, and Intensity) colour model which decouples the intensity component from the colour-carrying information (hue and saturation) in a colour image. HSI is regarded an ideal tool for developing image processing algorithms based on colour descriptions that are natural and intuitive to humans, who, after all, are the developers and users of these algorithms [114]. *Fig. 2.15* shows the colour cone of the HSI colour model.

H: Hue, angle

S: Saturation

I: Intensity
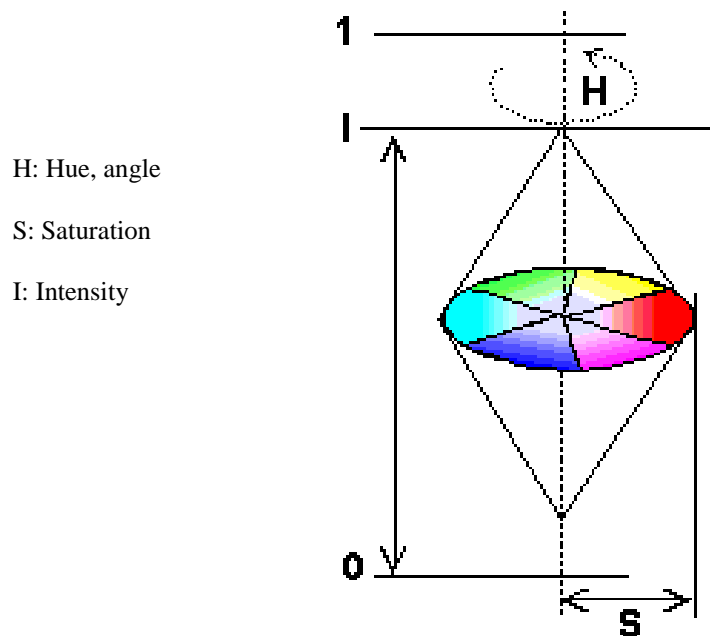
Fig. 2.15 HSI colour model.

In order to satisfy hardware implementations, conversions between HSI colour model and RGB colour model are required. For the conversion from HSI colour model to RGB colour model, raw data values of *H*, *S*, and *I* are given. The factors *h, s, I, x, y*, and *z* has the following relationships:

$$h = H \times p / 180 , \qquad\qquad\qquad \text{Equ 2-20}$$

$$s = S / 100 , \qquad\qquad\qquad\qquad\qquad \text{Equ 2-21}$$

$$i = I / 255 , \hspace{4cm} \text{Equ 2-22}$$

$$x = i \times (1 - s) , \hspace{4cm} \text{Equ 2-23}$$

$$y = i \times [1 + \frac{s \times \cos(h)}{\cos(p/3 - h)}] , \hspace{3cm} \text{Equ 2-24}$$

$$z = 3 \times i - (x + y) . \hspace{3.5cm} \text{Equ 2-25}$$

The values of R, G, and B can be calculated by utilising the following equations:

$$0 < h < 2 \times p / 3$$

$$B = 255 \times x, R = 255 \times y, G = 255 \times z , \hspace{2cm} \text{Equ 2-26}$$

$$2 \times p / 3 \leq h < 4 \times p / 3$$

$$R = 255 \times x, G = 255 \times y, B = 255 \times z , \hspace{2cm} \text{Equ 2-27}$$

$$4 \times p / 3 \leq h < 2 \times p$$

$$G = 255 \times x, B = 255 \times y, R = 255 \times z . \hspace{2cm} \text{Equ 2-28}$$

For the conversion from RGB colour model to HSI colour model, the raw data values of *H*, *S*, and *I* are given. The factors *r*, *g*, and *b* are given by the following equations:

$$r = \frac{R}{R + G + B} , \hspace{4cm} \text{Equ 2-29}$$

$$g = \frac{G}{R + G + B} , \hspace{4cm} \text{Equ 2-30}$$

$$b = \frac{B}{R + G + B} . \hspace{4cm} \text{Equ 2-31}$$

The values of *H*, *S*, and *I* can be calculated by employing the following equations:

$$b \leq g$$

$$H = \cos^{-1} \{ \frac{0.5 \times [(r - g) + (r - b)]}{[(r - g)^2 + (r - b) \times (g - b)]^{0.5}} \} \times 180 / p , \hspace{1cm} \text{Equ 2-32}$$

$$b > g$$

$$H = 360 - \cos^{-1}\{\frac{0.5 \times [(r-g)+(r-b)]}{[(r-g)^2+(r-b)\times(g-b)]^{0.5}}\} \times 180/p \ ,$$ Equ 2-33

$$S = 100 \times [1 - 3 \times \min(r,g,b)] ,$$ Equ 2-34

$$I = (R+G+B)/3 .$$ Equ 2-35

For the conversation between RGB and HSI colour models, it should be noted that the values of saturation and intensity are limited by each other. This is conducted due to the double cone shape of the HSI colour model.

CHAPTER THREE: SYSTEM CALIBRATION AND STANDARD COLOUR ENCODED MULTIPLE-VIEW X-RAY IMAGE GENERATION

3.1 Introduction

This chapter presents the calibration of the X-TEK real-time X-ray machine VTX-160 in order to produce high quality multiple-view dual-energy X-ray images for the materials discrimination experiments. The four processes involved are the generation of an appropriate dual-energy X-ray spectrum, the generation of multiple-view X-ray image sequence, the normalisation of the image intensity, and the calibration of materials discrimination. The conventional materials discrimination curves (banana curves) method, which is widely adopted in the security industry, employs two materials discrimination curves to produce three material classes, which are namely organic, mixture, and metal. These three material classes are coded utilising an industry 'standard' colour palette into orange, green, and blue respectively. This conventional method is utilised to exam in the reliability of the calibrated VTX-160 system. Various experiments are analysed and discussed. Thousands of X-ray images are collected and stored as the basis for the further investigation of materials discrimination reported in Chapter four and Chapter five.

3.2 Generation of a Dual-energy X-ray Spectrum

Commercial security screening systems typically utilise split dual-energy linear X-ray detector arrays to sample simultaneously the low-energy and high-energy components of a polychromatic X-ray beam [115][70]. The signal from a front detector arises primarily from low-energy photons while the signal from a back detector is produced from the remaining higher energy photons. Therefore, dual-energy X-ray data are simultaneously produced from a single exposure for materials discrimination process. The initial objective of this research programme is to simulate simultaneous dual-energy

X-ray generation by producing a high-energy X-ray image sequence and a low-energy X-ray image sequence separately using two filters each exhibiting a different attenuation profile. The experiment setup employs a real-time X-ray imaging system; model VTX-160, manufactured by X-TEK Systems Ltd, as shown in *Fig. 3.1*. The image intensifier is optically coupled to an 8-bit $50Hz$ CCD camera system. The tungsten target X-ray source emits a polychromatic spectrum with an adjustable tube voltage ranging from $0\ keV$ to $160\ keV$. However, it is empirically observed that the maximum voltage for stable continuous operation is $150\ keV$. A tube current of $115\ \mu A$ is set constant throughout the experiments to ensure the system operated under the maximum power rating of $20\ kW$. Initially, the tube voltage is adjusted to $60\ keV$ and a filter (*Zn* plate of 3 mm thick) [116] is placed in front of the aperture of the X-ray source to attenuate most, if not all, of the emitted X-rays. This can be appreciated by referring to *Fig. 3.1*. The filter can be made of any material with the proviso that it has the thickness to introduce sufficient attenuation. Once the filter is selected, the tube voltage is increased to $95\ keV$ to enable a low energy X-ray spectrum in the range of $60\ keV$ to $95\ keV$ to be produced. A high-energy spectrum is obtained in a similar fashion by employing a *Zn* plate of 8 mm thick to attenuate radiation at $100\ keV$ and set the high-energy spectrum ranges from $100\ keV$ to $145\ keV$. The resultant energy windows are similar to those utilised by conventional security dual-energy X-ray scanners. The resultant low-energy and high-energy images have similar intensity.

1: VTX160 Control Panel
2: VTX160 Inspection Chamber
3: Image Intensifier
4: X-ray Point Source
5: Zinc Filter
6: Translation Table

Z (depth axis)

Y (detector axis)

X (motion axis)
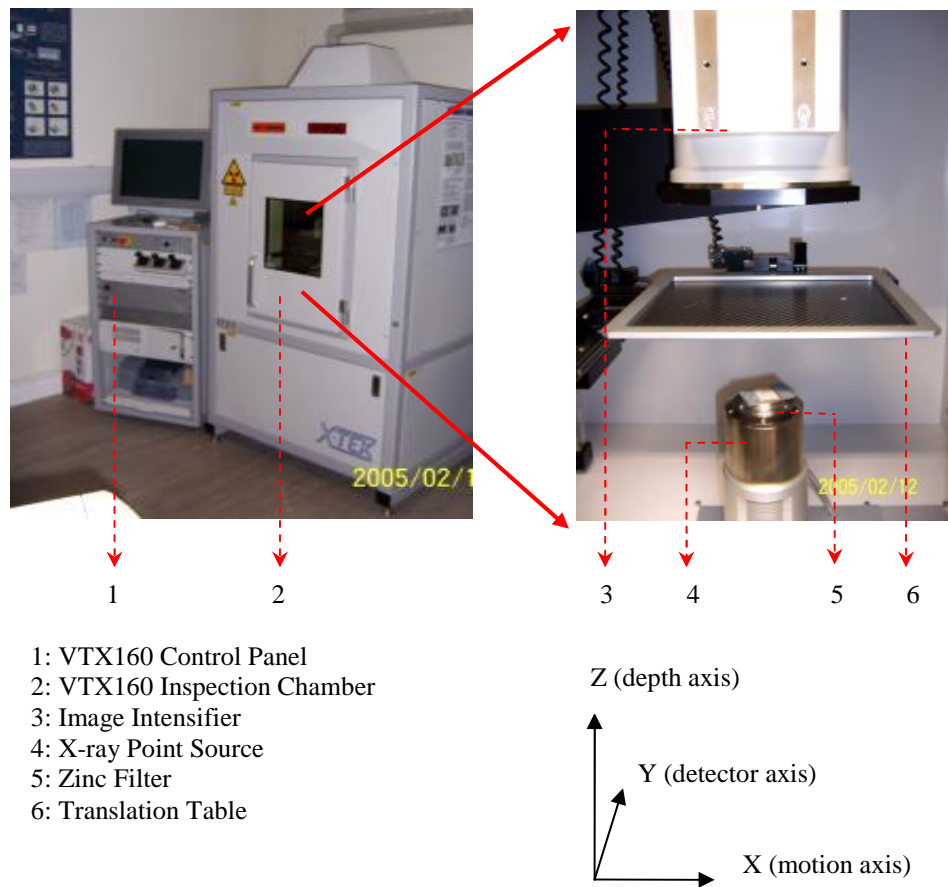
Fig. 3.1. Photographs of the experimental machine, VTX-160 model and its imaging configuration.

3.2 Generation of a Multiple View Line-scan X-ray Image Sequence

As described in Section 2.4 in Chapter two, a novel implementation of a real-time X-ray imaging system is developed to generate a sequence of perspective X-ray images in a line-scan format. The angular distribution of the line-scan views may be controlled by the simple expedient of selecting the appropriate video lines/photosite columns via software instructions. This feature has been found to be particularly useful during the empirical work. The developed implementation is adopted to produce 20 line-scan images acquired from 20 different perspectives, i.e. from -9 degree to +10 degree. This can be appreciated by correlating the illustration in *Fig. 3.2* and the imaging configuration in *Fig. 3.1*. The experiment specifications for this phase of work are as follows:

(a) angle of separation between adjacent perspectives: 1 degree;

(b) image resolution of the resultant line-scan image: 512 (*H*) × 512 (*W*) and;

(c) maximum field of view (*FOV*) along the *Y-axis* on the translation plate: 40 mm.
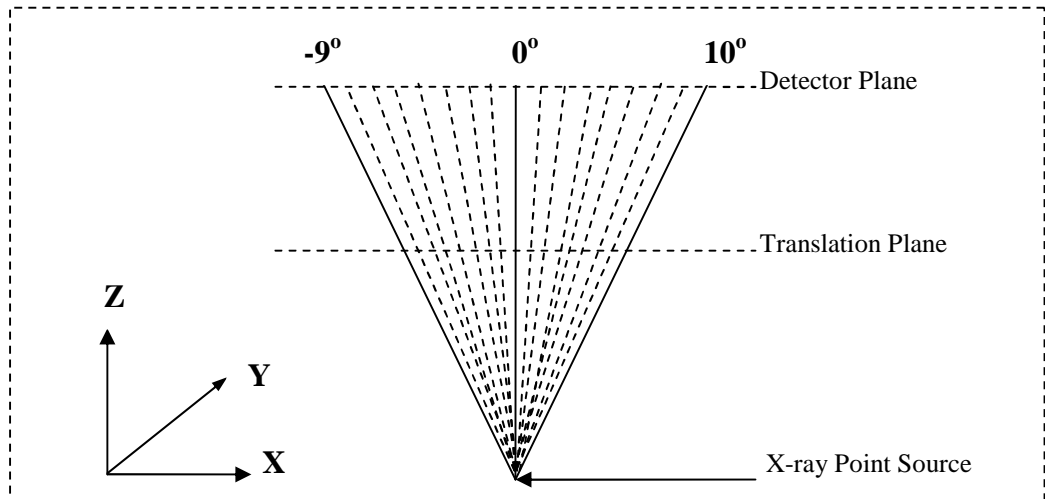
Fig. 3.2. Angular distribution for acquiring multiple-view line-scan images.

Fig. 3.3 illustrates a raw X-ray image captured by the installed area-array CCD camera where coordinates represents the *X*, *Y* coordinates of the four corners of the region of interest (ROI). The image resolution of this raw image is 768 (width) × 576 (height). A ROI, as highlighted by a red rectangular box, and was selected to meet the experimental specifications. *Fig. 3.4* illustrates the imaging geometry for the production of multiple view line-scan images.
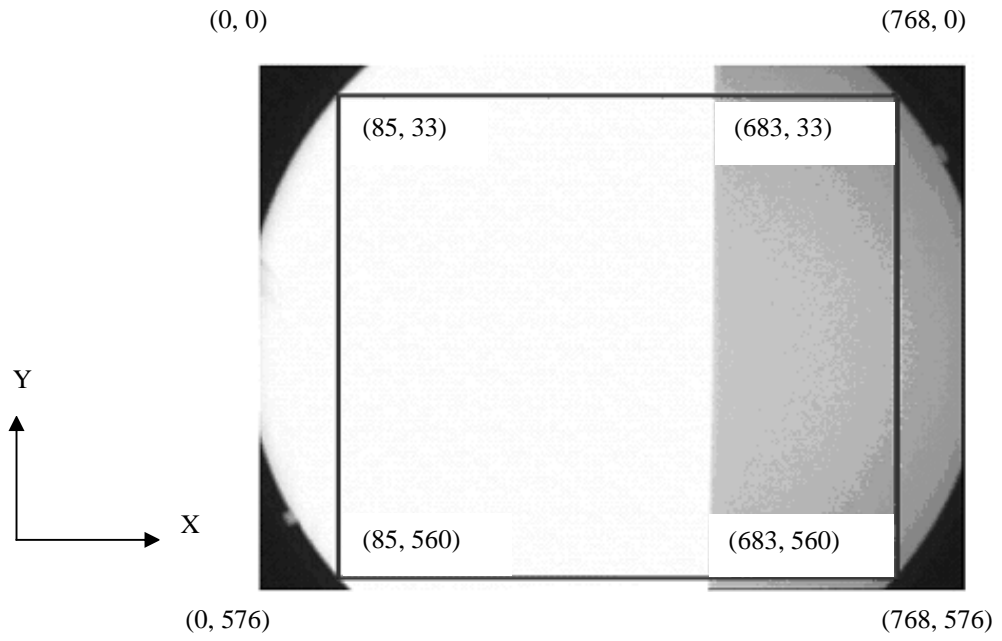
Fig. 3.3. Raw X-ray image captured by VTX-160.
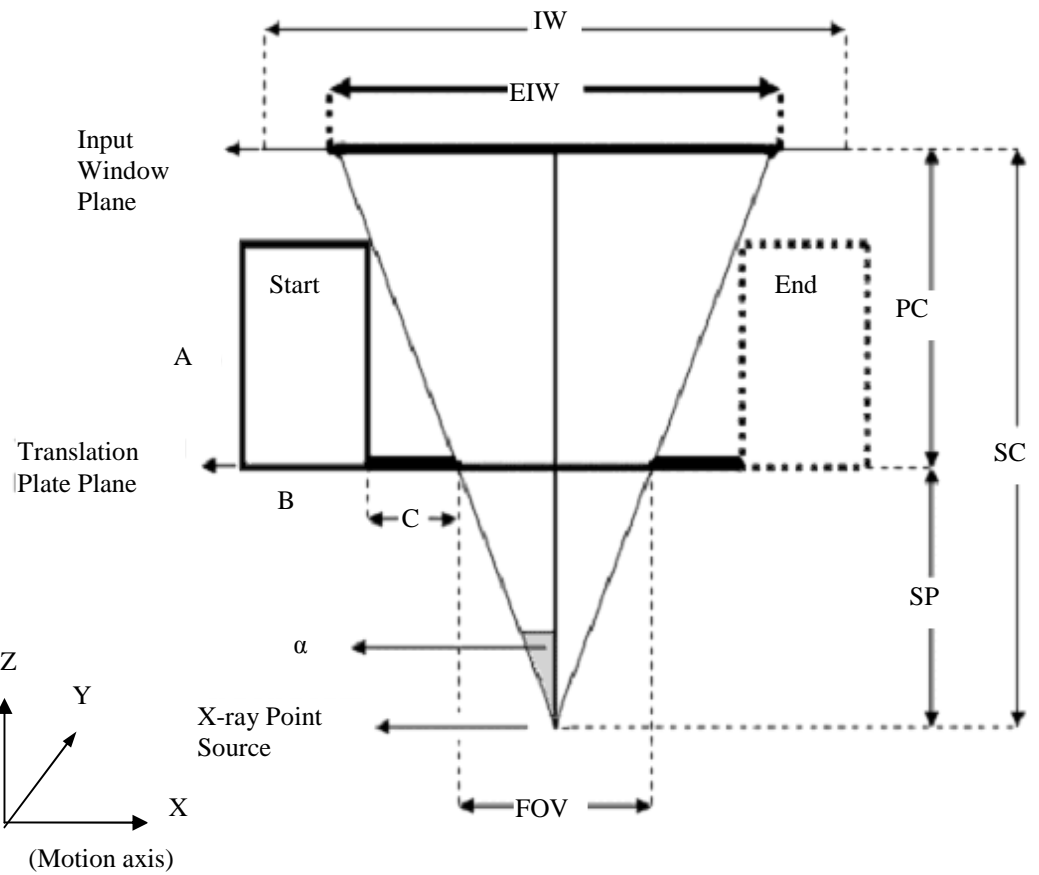
Fig. 3.4. Geometry for multiple view line-scan X-ray imaging.

41

IW is the measured input window for input window diameter of the image intensifier 135mm; *EIW* is the effective input window (mm); *A* is the height of the target object (mm) and *B* is width of target object; *C* is distance between the start scan position and the object peripheral in the translation plate plane (mm); *α* is half of maximum view angle (20 degree); *FOV* is field of view (40 mm); *PC* is distance between the input window plane and the translation plane (~185 mm); *SP* is distance between translation plate plane and X-ray point source (~115 mm) and; *SC* is the distance between input window plane and X-ray point source (~300 mm). This imaging configuration enables objects under inspection to have a maximum width of 40 mm and a maximum height of ~150 mm. The maximum length for an object under inspection is determined by the size of inspection chamber, and the maximum allowable weight that can be supported by the translation plate (i.e., 2 *kg*). The step resolution is defined as the smallest distance travelled along the X-axis between successive picture column acquisitions. By translating from left to right in *Fig. 3.4* is scanned over the full input window defined in *Fig.3.3*. The following equations were derived to calculate the parameters:

$$FOV = SP \times \tan(a) \times 2,$$
Equ 3-1

$$C = A \times \tan(a),$$
Equ 3-2

$$SC = SP + PC = EIW / (2 \times \tan(a)),$$
Equ 3-3

$$\text{Step resolution} = (B + C) / 512,$$
Equ 3-4

$$\text{Total motion on X-axis} = B + 2 \times C + FOV,$$
Equ 3-5

$$\text{Number of images} = \text{Total motion of X-axis} / \text{Step resolution},$$
Equ 3-6

$$EIW = IW \times (683 + 1 - 85) / 768,$$
Equ 3-7

Total displacement in *X*-axis is the distance between the start position and the end position of the target object.

3.3 Normalisation of the Image Intensity

When there is no structure between the X-ray source and the sensor, the presence of a filter at the X-ray source's aperture prevents the image intensity reaching the maximum value (i.e., 255 intensity levels for an 8-bit imaging system). Practical imaging systems produce images exhibiting non-uniform intensity even if a uniform input is supplied.

The imaging characteristics of each component in the imaging chain are unique. Thus variation in the response of detectors, either individually (over the time domain) or between themselves (over the spatial domain) is unavoidable in practice. The normalisation equation is employed to compensate for response non-uniformities is as follows:

$$I_{nor(n)} = Max \times \frac{(Raw_n - D_n)}{(B_n - D_n)}$$

.   Equ 3-8

Where $I_{nor\ (n)}$ is the normalised intensity, *Max* is the maximum intensity value of the imaging system, *Raw* is the raw intensity, *B* is the bright field intensity and *D* is the dark field intensity. Bright field is defined as the experimental condition where the system is exposed to the X-ray spectrum attenuated by a filter. Dark field refers to the experimental condition where the system is shielded from any external source. The width of each perspective image is formed by combining on a column-by-column basis, 512 sequential scan lines acquired from a selected photosite column on the CCD camera. Therefore, a line-scan based perspective image contains both temporal and spatial noise components which are compensated by the application of *Equ 3-8*.

3.3.1 Experiment results and discussion

As explained in the preceding test, the resultant line-scan X-ray images generated by using the proposed multiple-view imaging technique will exhibit spatial noise (*S*) and temporal noise (*T*) along the *Y*-axis and the *X*-axis, respectively. A separate analysis is therefore devised to measure the magnitude of each noise source as a function of perspective angle and to evaluate the effectiveness of the proposed normalisation algorithm. The variation in intensity produced by the high-energy (*H*) and the low-energy (*L*) X-ray data are organised in *Fig. 3.5* and *Fig. 3.6*, respectively. *Fig 3.5(a)* and *Fig 3.6(a)* indicate intensity trends along the Y-axis while the respective (b) plot in both figures represents the intensity trends along the X-axis. Besides plotting the average intensity (*MEAN*), the maximum (*MAX*) and minimum (*MIN*) bands are included to signify the fluctuation caused by both noise sources. Also included are

measurements obtained from normalised (*N*) data to demonstrate the positive effect of applying normalisation. The degree of fluctuation for both noise sources are measured in standard deviation units as presented in *Fig. 3.7*. It should be noted that linear lines are superimposed to aid the visual analysis but do not represent an accurate intermediary intensity between two perspectives.
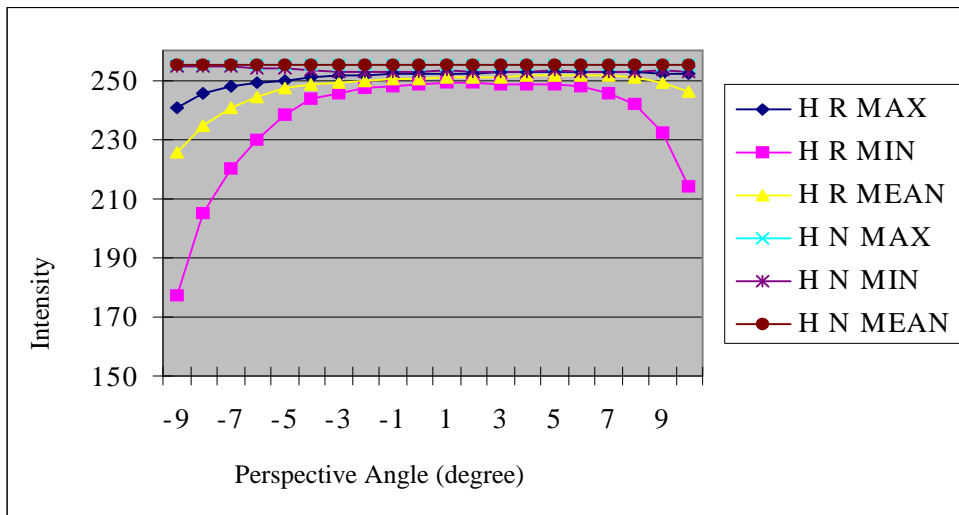
(a)
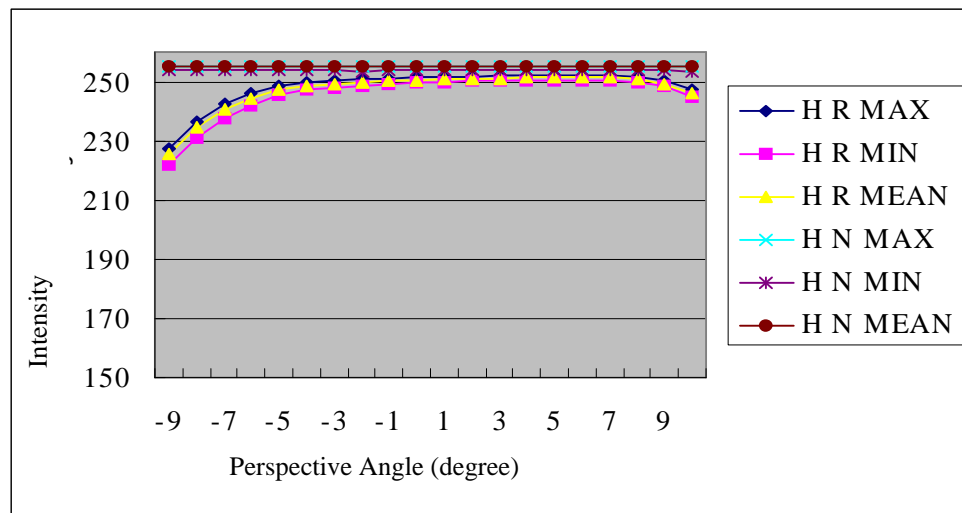
(b)

Fig. 3.5. Plots of maximum (MAX), minimum (MIN) and MEAN values of intensity against perspective angle that are measured along the (a) Y-axis and (b) X-axis of the raw (R) and the normalised (N) High-energy (H) X-ray Line-scan image.
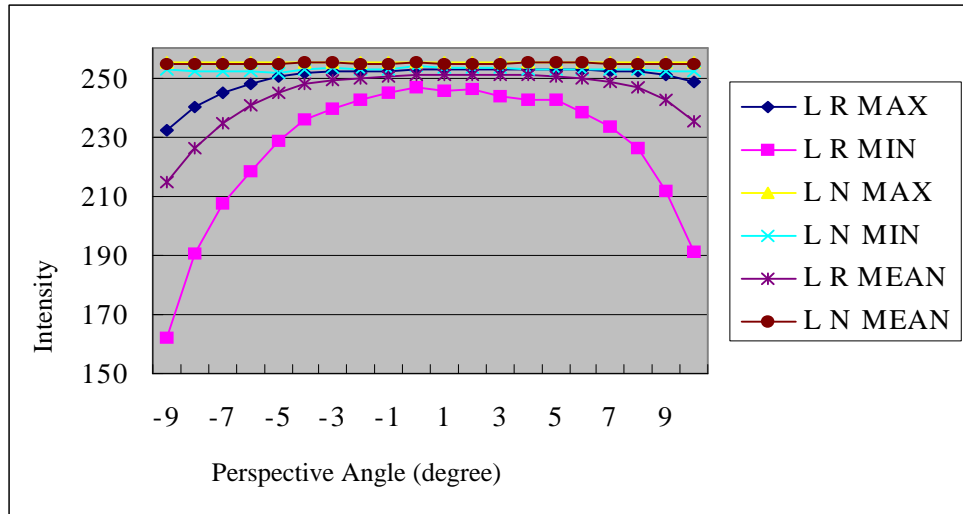
(a)
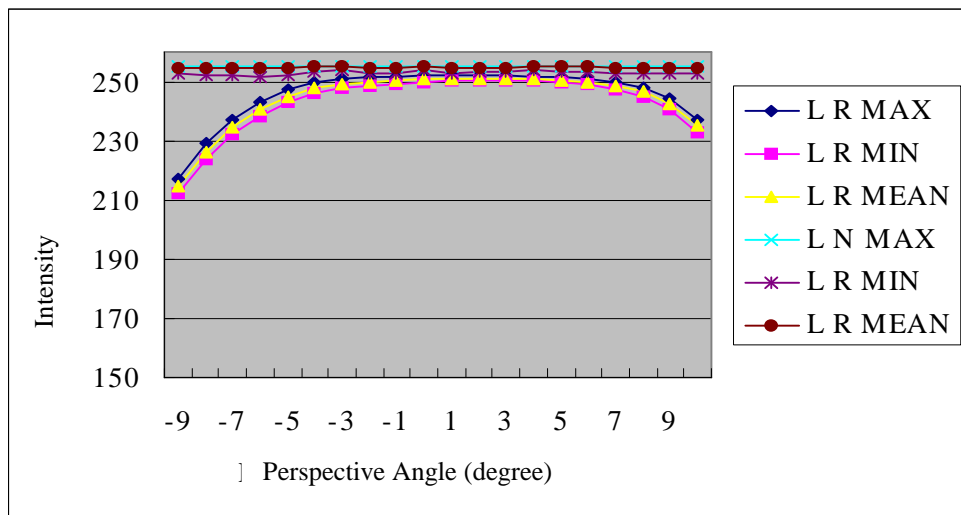
(b)

Fig. 3.6. Plots of maximum (MAX), minimum (MIN) and MEAN values of intensity against perspective angle that are measured along the (a) Y-axis and (b) X-axis of the raw (R) and the normalised (N) Low-energy (L) X-ray Line-scan image.
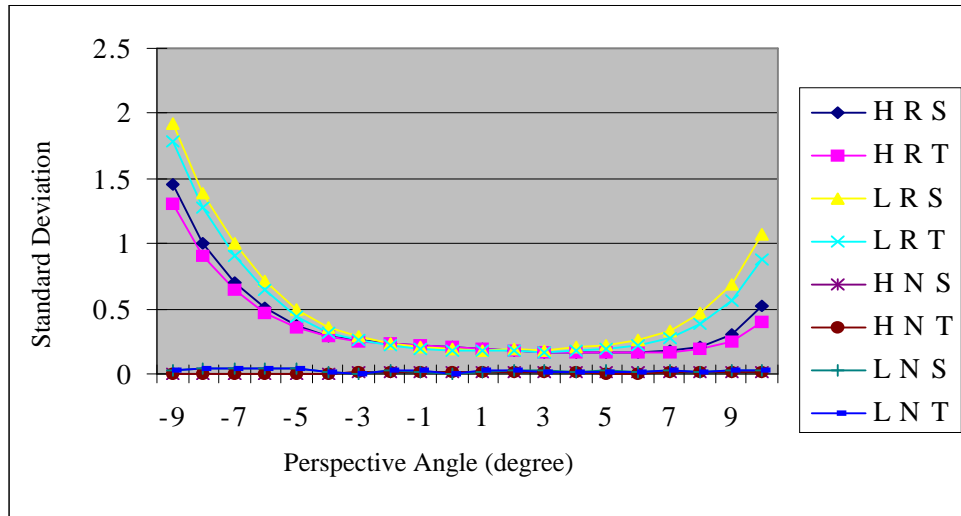
Fig. 3.7. Plots of spatial noise (S) and temporal noise (T) in standard deviation unit against perspective angle that are measured from the raw (R) and the normalised (N) High-energy (H) and Low-energy (L) X-ray Line-scan image.

The intensity plots produced by the raw data in *Fig. 3.5* and *Fig. 3.6* imply that the resultant line-scan images contain a greater amount of spatial noise than temporal noise. However, the standard deviation measurement presented in *Fig. 3.7* indicates that both noise sources are closely similar in both *Low* energy and *High* energy levels. These conflicting results suggest that there may be a few photosites in the selected CCD column that behave as outliers and inflate the extremes of the intensity fluctuation, but without significantly affecting the overall degree of fluctuation. Despite the difference in magnitude between the two noise sources, the proposed normalisation algorithm demonstrated its effectiveness to compensate for both spatial and temporal noise. This result can be appreciated by comparing the intensity plots produced by the raw data and the normalised data in *Fig. 3.5* to *Fig. 3.7*. In addition to the quantitative analysis, X-ray images are presented in *Fig. 3.8* to *Fig. 3.10* to illustrate the positive visual effect of the normalisation algorithm.
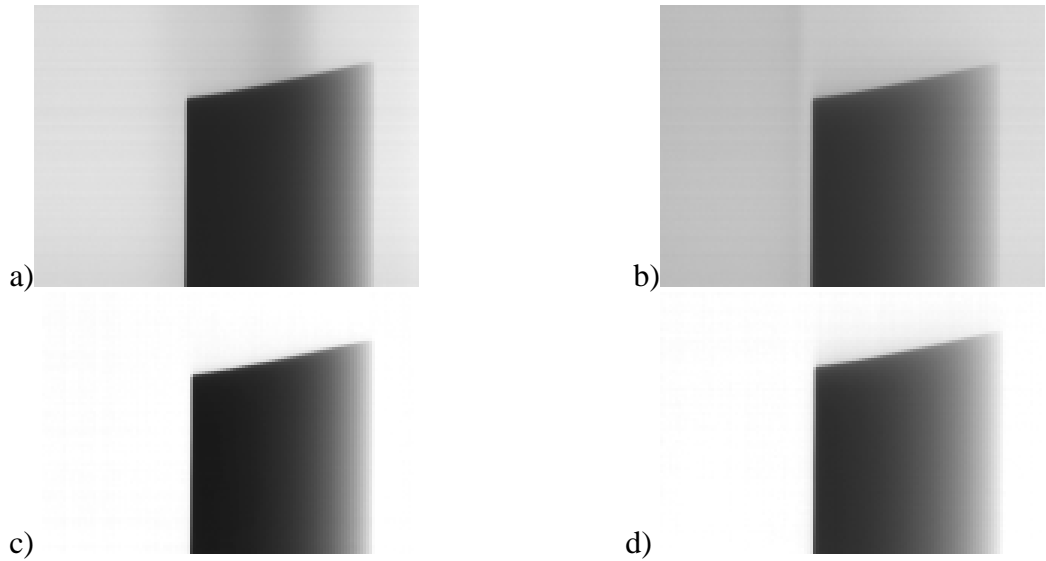
Fig. 3.8. Al linear wedge: (a) and (b) are the low-energy X-ray image and the high-energy X-ray images before normalisation while (c) and (d) are the low-energy and high-energy X-ray images after normalisation. All images were acquired from 0^0 perspective angle.
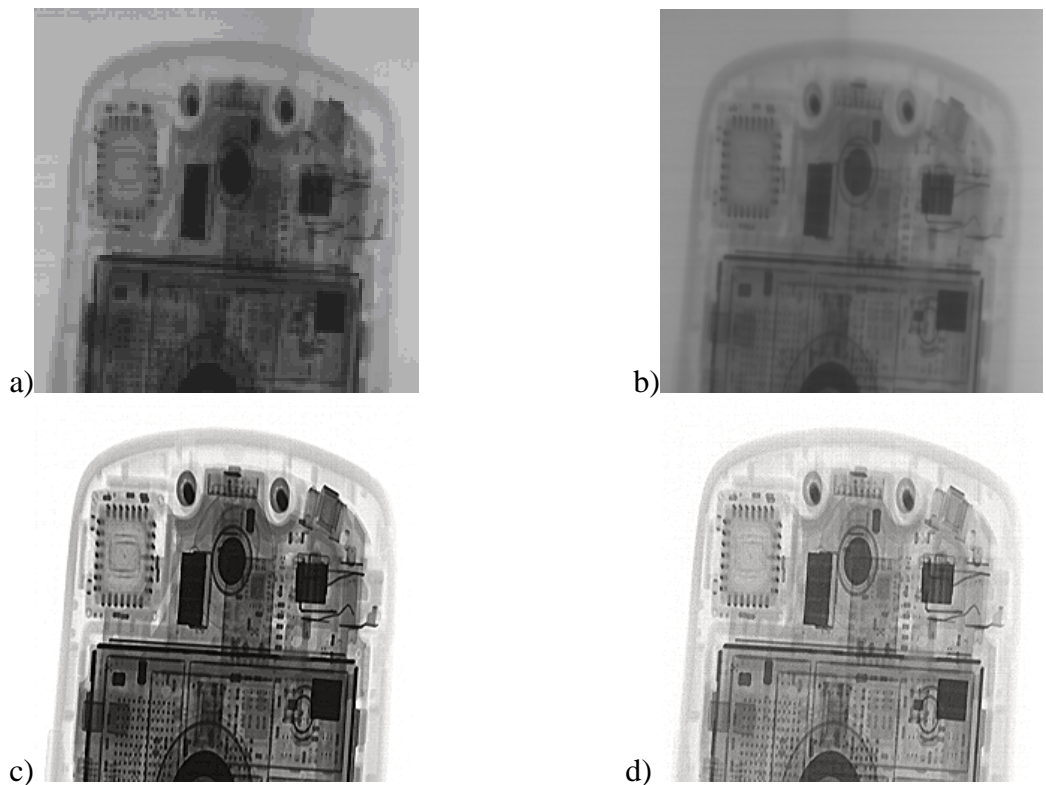
Fig. 3.9. Section of a mobile phone: (a) and (b) are the low-energy X-ray image and the high-energy X-ray image before normalisation while (c) and (d) are the low-energy and high-energy X-ray image after normalisation. All images were acquired from 0^0 perspective angle.

Before normalisation

After normalisation

-9^0 perspective angle

-5^0 perspective angle

0^0 perspective angle

5^0 perspective angle
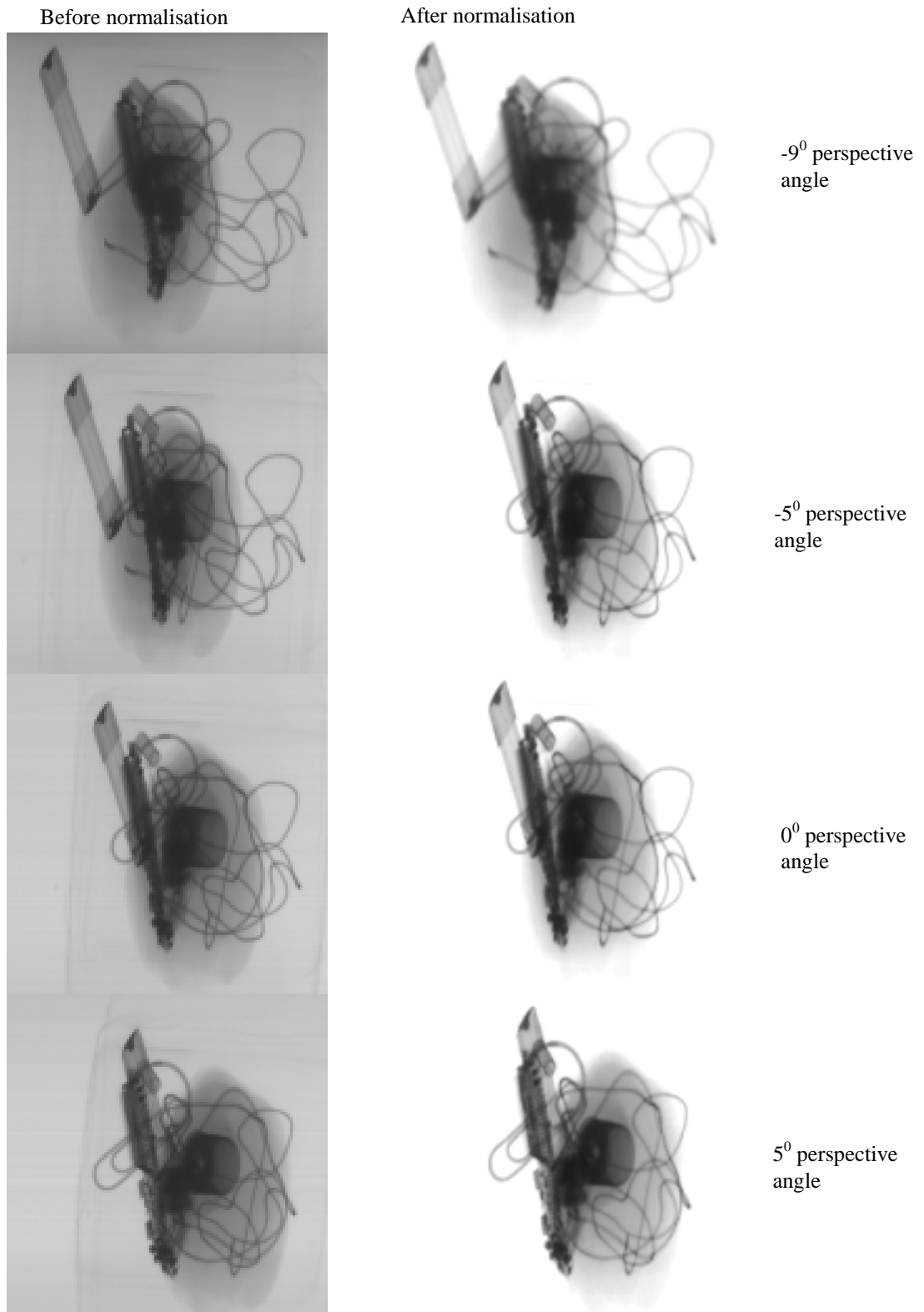
Fig. 3.10. Sample of perspective images produced by the multiple view line-scan X-ray image intensifier system. Images on the left column are the raw average images while their respective normalised results are presented on the right column. A full image sequence of 20 perspective images is organised in Appendix A.

Further observation of *Fig. 3.5* to *Fig. 3.7* reveals that the noise magnitude measured in the raw data increases concomitantly with the increase in perspective angle (with respect to the 0° perspective in both directions). Images that are acquired from negative perspective angles have recorded a greater noise magnitude than images that are acquired from positive perspective angles. Also, the noise magnitudes reach the minimum for images acquired from between 1° to 3° perspectives. These observations are somewhat expected and are consistent with the fact that a X-ray beam's intensity is not uniform throughout its entirety due to the "heel effect" produced by a typical X-ray source [117][118][40]. The results suggest that the anode of the X-ray source is located in the direction of the negative perspective. This finding is not a barrier to progress at this stage of the work because the variation in intensity over the perspective angle is compensated for by the normalisation algorithm.

A visual comparison on the *MEAN* plots of raw data in *Fig. 3.5* and *Fig. 3.6* suggest that the intensity strength of the *Low* and *High* energy images is very similar. Also, as evident in *Fig. 3.7*, the noise magnitudes produced by *Low* energy data are slightly greater than the ones produced by *High* energy data. The difference is expected and it is considered acceptable due to the marginal nature of differences. Nonetheless, these observations have demonstrated the success of generating two X-ray images containing similar intensity strength using the proposed imaging technique.

3.3.2 Image intensity variation

Image quality is improved by applying the normalisation method which mainly aims to remove the heel effect and the noise due to differences between the sensitivity of array detectors. However, significant noise is still presented in the resultant images. The source of this noise includes aspects of the mechanical design of scanning system, stability of the X-ray tube current and temperature sensitivity of intensifier etc. For example, the X-ray tube current of VTX-160 had a variation of 5 μA as measured by operational software purchased from X-TEK systems, Ltd. Dual energy line-scan X-ray

images of six-step wedges are shown in *Fig. 3.11 (a)* and *(b)* with several profile lines indicated by the dashed lines. The results of profile lines are in *Table 3.1* respectively.

(a)

(b)
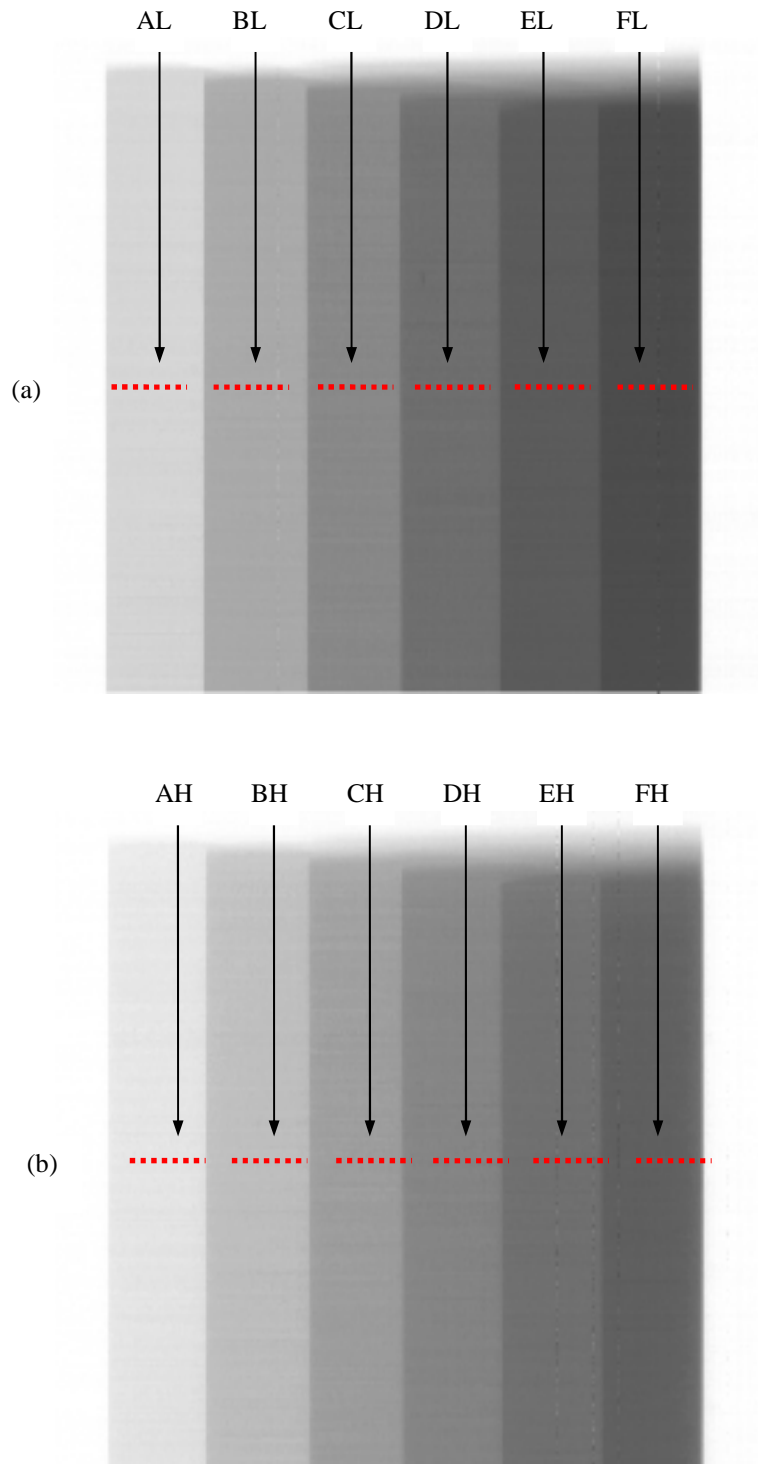
Fig. 3.11. PTEF step wedge (a) high and (b) low energy line-scan X-ray images.

	Mean	Min.	Max.	Stdev	Max.-Min.
AL	229	225	231	0.9	6
BL	185	189	192	0.7	7
CL	158	156	160	0.6	4
DL	132	128	135	0.6	7
EL	112	110	116	0.5	6
FL	95	91	97	0.5	6
AH	213	211	215	0.8	4
BH	170	167	172	0.7	5
CH	138	136	140	0.7	4
DH	109	108	111	0.6	3
EH	91	90	92	0.6	2
FH	77	75	81	0.5	6
Average	142	140	145	0.6	5

Table 3.1 Grey levels for the 'dashed' regions on the PTFE step wedge highlighted in Fig. 3.11.

3.4 Calibration of Materials discrimination

The difference in magnitude between the high-energy X-ray signal and the low-energy X-ray signal is exploited to broadly discriminate an inspected object into three material classes as function of atomic number. The organic class is for compounds with an average atomic number $Z_{average} \leq 10$, a mixture of organic and metallic material (or mixture) class is for compounds with $10 < Z_{average} < 20$ and the metallic class is for compounds with $Z_{average} \geq 20$. The resultant discrimination information is presented to the human operators by colour encoding the X-ray images. Typically organic, mixture and metallic materials are displayed as orange, green and blue, respectively.

Three materials discrimination transfer functions obtained from organic, mixture and metallic materials are required to formulate the colour encoding scheme. These functions are plots of the differential of *High* and *Low* energy X-ray data (*Hi-Lo*) versus the average of the *High* and *Low* energy X-ray data. Conventionally, a polymethyl methacrylate (*PMMA*) step-wedge, an aluminium (*Al*) step-wedge and an iron (*Fe*) step-wedge are employed to produce the three materials discrimination curves. However, it is observed that the discrete nature of the step-wedges limits the number of data points in the transfer functions, which may lead to erroneous colour encoding. This problem is minimised in this work by devising linear wedges. The general properties of the three wedges, shown in *Fig. 3.12*, are tabulated in *Table 3.2* where W, L, D_{min} and D_{max} is the width, the length, the minimum and the maximum thickness of the wedge (mm), respectively, and r is the density of the wedge (g/cm^3). The data are complied from the literature [119][37] and the effective atomic number of the *PMMA* wedge ($C_5H_8O_2$) is calculated by using the equation found in the literature [120].
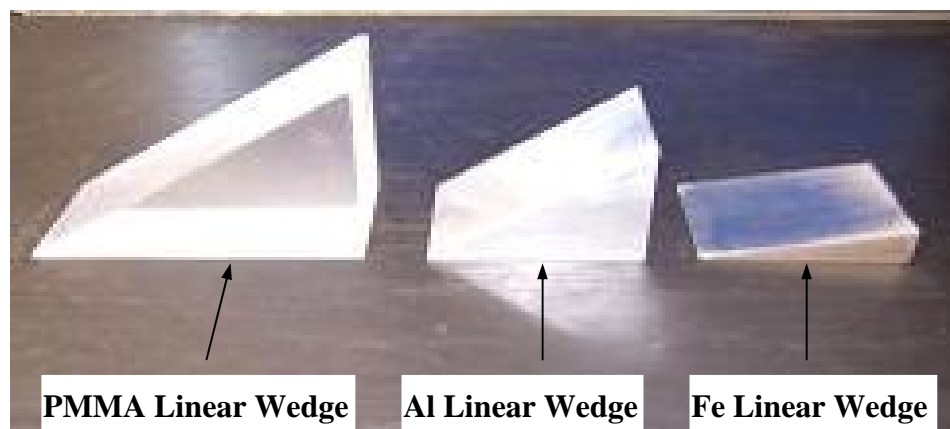
Fig, 3.12. PMMA, Al, and Fe linear wedges.

Material	Extrinsic Property				Intrinsic Property	
	W	L	D_{min}	T_{max}	ρ	Z_{eff}
PMMA	80	100	4.0	160	1.19	6.64
Al	80	100	1.0	100	2.70	13.00
Fe	80	100	0.5	20	7.86	26.00

Table 3.2. Properties of the experimental PMMA, Al and Fe linear wedges used in the experiments.

3.4.1 Experiment results and discussion

The resultant materials discrimination transfer functions are presented in *Fig. 3.13* The curve *A* and curve *B* are the two midpoint curves produced to establish two discrimination boundaries. This midpoint plotting method is approximately analogous to calculating the average effective atomic number, $Z_{average}$ between the *PMMA* and *Al* ($Z_{average}$ ~9.7) and; between the *Al* and *Fe* ($Z_{average}$ ~19.5). The area below curve *B* represents the signature region for organic materials, the area between curves *A* and *B* is the mixture materials' signature region while the area above curve *A* is the metallic region. Two lookup tables are produced for each midpoint curve. Using these lookup tables, the colour encoding algorithm began with categorising the raw image data of the object under inspection (pixel-by-pixel) into one of the three material classes. Each averaged image data is assigned to the appropriate 24-bit *RGB* colour intensity by utilising the industry 'standard' colour palettes. A *RGB* model to *HSI* model converter is employed to aid perceptual colour adjustment. A lookup table is established for colour encoding the X-ray image. The lookup table involves *High* and *Low* energy information of X-ray image; *R*, *G*, and *B* colour intensity, and *H*, *S*, and *I* information. *Fig. 3.14* depicts examples of the resultant colour encoded X-ray images.
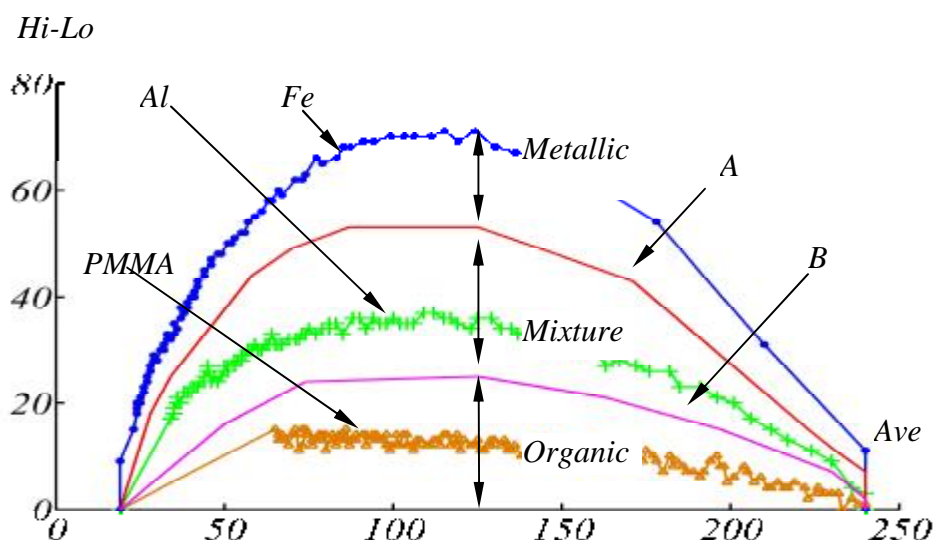
Fig. 3.13. Materials discrimination transfer functions for the PMMA, Al and Fe linear wedges.
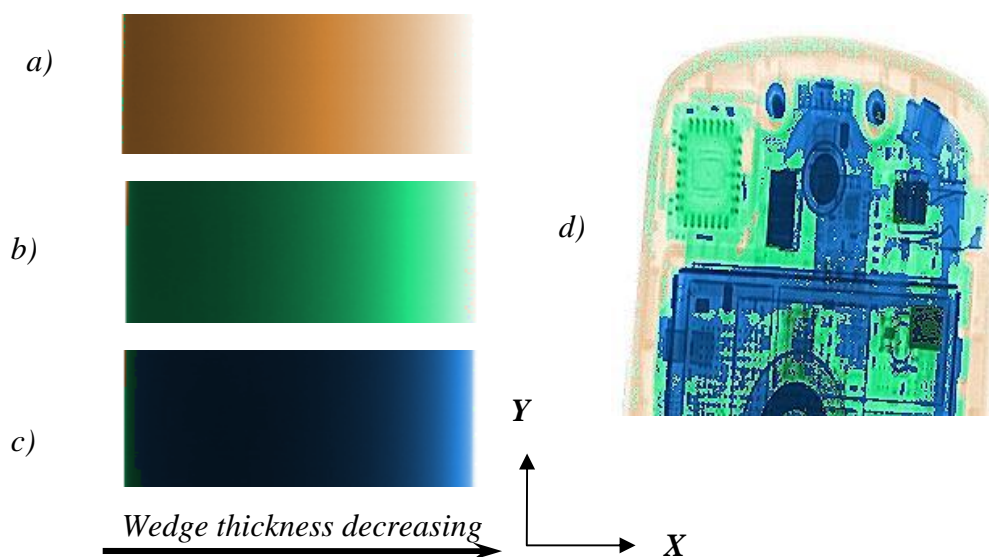
Fig. 3.14. Colour encoded X-ray images of the (a) PMMA linear wedge, (b) Al linear wedge, (c) Fe linear wedge and (d) mobile phone. All images were acquired from a 0^0 perspective angle.

In addition, four views selected from a twenty view sequence (See Appendix B) are illustrated in *Fig. 3.15*. The imaged objects included a paper clip, a printed circuit board and a fuse. In addition a 0.303" calibre cartridge case is arranged to resemble a detonator inserted in a dense organic material to simulate plastic explosive. The end view of the cartridge case appears as a dark grey disc in the amorphous image of a moulded organic material. These objects are located, in sequence, from foreground to background over a relative depth of approximately 15 cm. The sequential parallax information inherent in these images may be appreciated by observing the relative displacement of the corresponding or conjugate object features in successive views. It can also be appreciated that colour shifts occur due to the changing relative interposition of background and foreground objects throughout the sequence (i.e. the blue wire becoming green as it is masked by the organic background). The potential for colour change as a function of the X-ray beam path through the object under inspection is a fundamental property of dual-energy transmission imaging.

-9⁰ perspective angle

-4⁰ perspective angle

0⁰ perspective angle

5⁰ perspective angle

Y

X
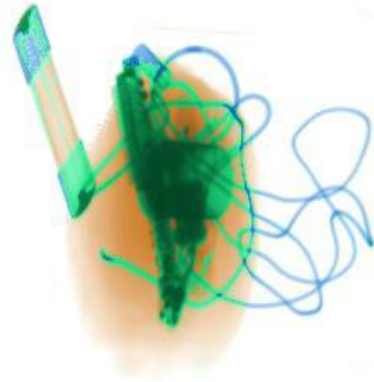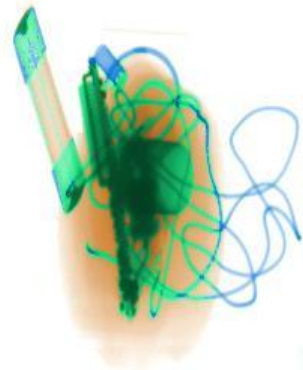
Fig. 3.15. Sample perspective colour images produced by the multiple view line-scan X-ray image intensifier system.

3.4.2 Colour encoding uncertainty for overlapping materials

To illustrate colour encoding transitions due to overlapping different materials an *Al* wedge was placed on top of a thick (72 mm) *PMMA* plate and a thin (12 mm) *PMMA* plate. A single perspective view from this experiment is shown in *Fig. 3.16*. In this arrangement the attenuation profile (in the horizontal) of the linear wedge changes while maintaining a constant attenuation for the thick and the thin *PMMA* material. Two line profiles, indicated by the dashed lines, in *Fig. 3.16* are plotted in materials discrimination space in *Fig. 3.13*. The colour encoding transitions from orange to green are indicated by the crossover regions in *Fig. 3.17*.
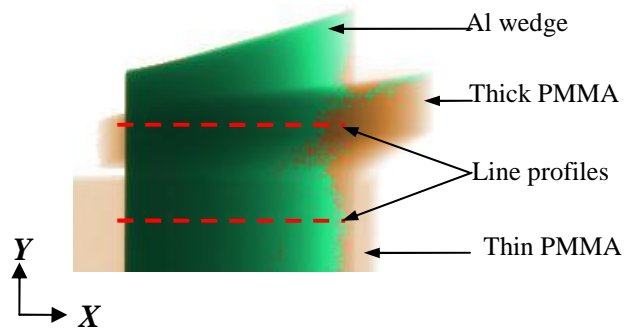
Fig. 3.16. Illustration of colour changes as a function of attenuation introduced by an Al linear wedge using thick (72 mm) and thin (12 mm) PMMA plates.
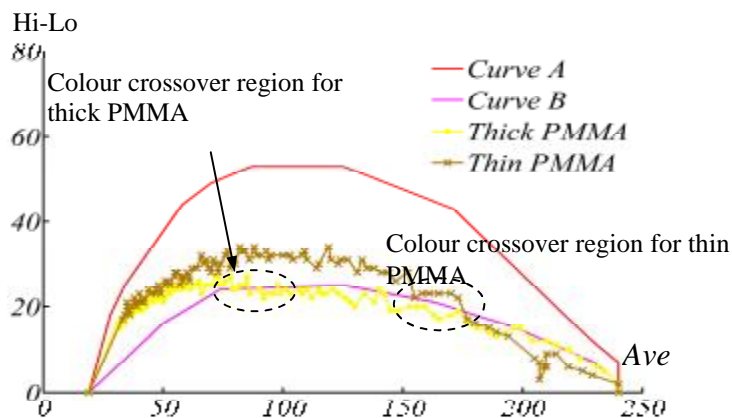
Fig. 3.17. Materials discrimination space to illustrate the colour changes as a function of attenuation introduced by the Al linear wedge using thick and thin PMMA plates.

The resultant colour encoding of a dual-energy X-ray image for multi-layered objects is a function of the X-ray beam angle associated with the individual pixels which comprise the resultant image. The cluttered images routinely encounted by screeners at airports exhibit this fundamental property. Thus threat substances may be masked and 'colour occluded' by the clutter of everyday items in luggage as illustrated in *Fig. 3.13*. Plastic explosives, which can be modelled into almost any shape, are the pre-eminent threat to existing luggage screening systems [121] [122]. The inability to separate overlapping items from the transmission X-ray signal poses problems when plastic explosives are hidden behind/in front or within an object of high attenuation (e.g., metal). Based on the broad definition of the colour encoding scheme described in above section, there are many instances where plastic explosives would not be classified as organic further exacerbating the screening task.

CHAPTER FOUR: MATERIALS DISCRIMINATION

4.1 Introduction

This chapter initially reports an empirical investigation of the K-II technique for discrimination of a material of known-thickness without any masking material present. To investigate the potential for discriminating masked target materials automatically further work combines the K-II technique with a W-E subtraction technique to extract the effective atomic number and surface density of any masking objects present.

4.2 K-II Technique

The K-II technique enables discriminating unmasked materials with known thickness. The K-II technique exploits the interrelationship of effective atomic number, mass density, and thickness in a total amount of attenuation produced by high-energy and low-energy X-ray inspections. The prototype of the K-II technique is derived from the ρZ projection method [15][56] and the direct reconstruction of the effective atomic number by a method of multi-energy radiography [123][124][125].

4.2.1 Numerical translation of the ρZ projection method

The ρZ projection method was initially introduced by B. J. Heismann, J. Leppert, and K.Stierstorfer in August, 2003. It employs an energy-solving X-ray method with Computed Tomography (CT) measurement to obtain the mass density ρ and effective atomic number Z of a target material. With two measurements of the detected image intensity I_1 and I_2, the full numerical treatment yields $\rho(I_1, I_2)$ and $Z(I_1, I_2)$ with a continuous X-ray spectrum $S(E)$ and a detector sensitivity $D(E)$. It is shown:

$$m = \frac{\lim}{d \to 0}[-\frac{1}{d}\ln(\frac{I}{I_o})] \,, \qquad\qquad \text{Equ 4-1}$$

$$\frac{I}{I_o} = \int W(E) \times \exp(-(a \times \frac{Z^k}{E^l} + b) \times r \times d)dE \,, \qquad\qquad \text{Equ 4-2}$$

with the weighting function

$$W(E) = \frac{S(E) \times D(E)}{\int S(E) \times D(E) dE} \ . \qquad\qquad \text{Equ 4-3}$$

Where μ is the attenuation coefficient, d is the thickness along the X-ray inspection path, I is the detected image intensity, I_o is the original image intensity, E is the X-ray tube energy, Z is the effective atomic number, ρ is the mass density, and α, β, k, and l are all treated as constants. Classically, l has a value of 3. According to a personal communication with B. J. Heismann, the weighting function of the ρZ projection method is associated with the physical performance of the devices. This function can be considered constant when the devices' parameters remain unchanged throughout the investigation. Thus, it is suggested that the weighting function can be replaced by a polynomial equation.

Considering polychromatic X-ray spectrums [126][127][128], a 3rd order polynomial equation is employed to simulate the weight function in *Equ 4-2*. With the dual-energy X-ray setup described in Chapter three and the classical value of l in *Equ 4-2*, the following is obtained:

$$I_1 = I_0 \int_{60}^{95} (a_1 \times E_1^3 + b_1 \times E_1^2 + c_1 \times E_1 + d_1) \times \exp(-(a\frac{Z^{k_1}}{E_1^3} + b) \times r \times d) dE_1 , \ \text{Equ 4-4}$$

$$I_2 = I_0 \int_{100}^{145} (a_2 \times E_2^3 + b_2 \times E_2^2 + c_2 \times E_2 + d_2) \times \exp(-(a\frac{Z^{k_2}}{E_2^3} + b) \times r \times d) dE_2 , \ \text{Equ 4-5}$$

where I_1, I_2 are the detected image intensity at low-energy and high-energy X-ray inspections, respectively. E_1 is the low-energy X-ray (between 60 *keV* and 95 *keV)* and E_2 is the high-energy X-ray (between 100 *keV* and 145 *keV*). Integrating *Equ 4-4* and *Equ 4-5* using a professional mathematics tool- Mathematica yields:

$$\frac{I_1}{I_o} = \exp(\frac{68490625 \times a_1 \times b \times r \times d}{4} + \frac{641375 \times b_1 \times b \times r \times d}{3}$$

$$+ \frac{5425 \times c_1 \times b \times r \times d}{2} + 35 \times d_1 \times b \times r \times d$$

$$+ 35 \times a_1 \times a \times Z^{k_1} \times r \times d + \frac{7 \times c_1 \times a \times Z^{k_1} \times r \times d}{1140}$$

$$+ \frac{217 \times d_1 \times a \times Z^{k_1} \times r \times d}{2599200} + b_1 \times a \times Z^{k_1} \times r \times d \times \log(\frac{19}{12}))$$

, Equ 4-6

$$\frac{I_2}{I_o} = \exp(682875 \times b_2 \times b \times r \times d + \frac{11025 \times c_2 \times b \times r \times d}{2}$$

$$+ 45 \times d_2 \times b \times r \times d + \frac{45 \times 7601125 a_2 \times b \times r \times d}{4}$$

$$+ \frac{9 \times c_2 \times a \times Z^{k_2} \times r \times d}{2900} + \frac{441 \times d_2 \times a \times Z^{k_2} \times r \times d}{16820000}$$

$$+ \frac{45 \times 7601125 \times a_2 \times a \times Z^{k_2} \times r \times d}{4} + b_2 \times a \times Z^{k_2} \times r \times d \times \log(\frac{29}{20}))$$

, Equ 4-7

Lumping together the constant and parameters in *Equ 4-6* and *Equ 4-7* enables a simpler notation to be presented:

$$\frac{I_1}{I_o} = \exp(A_1 \times r \times d + B_1 \times r \times d \times Z^{k_1}),$$

Equ 4-8

$$\frac{I_2}{I_o} = \exp(A_2 \times r \times d + B_2 \times r \times d \times Z^{k_2}).$$

Equ 4-9

Equ 4-8 and *Equ 4-9* are the numerical translation of the ρZ projection method where A_1, B_1, k_1 and A_2, B_2, k_2 are related to the constants in *Equ 4-6* and *Equ 4-7*. The simplification by the numerical translation provides a foundation for developing a practical approach to extract atomic number and mass density information.

4.2.2 Development of the K-II technique

Considering the numerical translation format of the ρZ projection method in *Equ 4-8* and *Equ 4-9*, it may be appreciated that the measurement of the image intensity is only dependent upon the material parameters; effective atomic number, mass density and thickness along the X-ray inspection path. Using the same experimental setup, the material parameters are determined by the total amount of attenuation measured at each energy level. Hence, a basic model of the K-II may be established as:

$$A_{IL} = Z^{k_{IL}} \times r_S, \qquad\qquad \text{Equ 4-10}$$

$$A_{IH} = Z^{k_{IH}} \times r_S, \qquad\qquad \text{Equ 4-11}$$

where A_{IL} and A_{IH} are attenuation factors for the low-energy and high-energy detected image intensity *IL and IH* respectively; k_{IL} and k_{IH} are treated as system constants for different energies; and ρ_S is surface density, dimensionality $[\rho_S] = g/cm^2$. The unknowns in the equations (i.e, attenuation factors and constants) can be computed by scanning two (or more) materials of known parameters. After the unknowns are determined, the Z_{eff} and ρ_S of any material can be estimated via numerical approach such as the Newton-Raphson iteration method. The main drawback of using an iteration method is that it is computationally expensive and convergence may be difficult to achieve in practice [129][130][131]. Hence, it is proposed in this research programme to transform *Equ 4-10* and *Equ 4-11* in such a manner that they can be equated and hence optimising the search. The transformation produces the following equations:

$$\frac{r_S}{Z^k} = N_{IL} \times Z^{K_{IL}}, \qquad\qquad \text{Equ 4-12a}$$

$$\frac{r_S}{Z^k} = N_{IH} \times Z^{K_{IH}}, \qquad\qquad \text{Equ 4-12b}$$

Hence

$$N_{IL} \times Z^{K_{IL}} = N_{IH} \times Z^{K_{IH}}, \qquad\qquad \text{Equ 4-13}$$

where k, N_{IL}, N_{IH}, K_{IL}, K_{IH} are unknowns derived from *Equ 4-10* and *Equ 4-11*. These unknowns are determined through a calibration procedure which involves scanning a number of materials with known parameters. This transformation establishes a direct relationship between the measurements recorded at the low and high-energy levels, in which only one Z_{eff} value can satisfy *Equ 4-13*. This proposal exploits the dual-energy data to offer a pragmatic and cost-effective (computationally) solution to the computation of Z and ρ_S with limited but justifiably high accuracy.

4.2.3 Calibration of the K-II technique

Five different wedges are utilised in the calibration of the K-II technique:

- plastic step wedge (*Pl, ($C_5O_2H_8$)n, ρ1=1.19 g/cm3, Z=6.46*);

- Teflon step wedge (*PTFE, CnF_2n, ρ2=2.2 g/cm3, Z=8.435*);

- aluminium step wedge (*Al, Al, ρ3=2.7 g/cm3, Z=13*);

- titanium step wedge (*Ti, Ti, ρ4=4.5 g/cm3, Z=22*);

- steel *linear* wedge (*Fe, Fe, ρ5=7.8 g/cm3, Z=26*).

Wedges of known thicknesses are scanned as illustrated in *Fig. 4.1*. The wedges (step and linear) are configured with respect to a dual-energy X-ray source and X-ray detector modules as illustrated in *Fig. 4.2*. Multiple-view images of the wedges are obtained along the *X*-axis (motion axis). Thus, the changes in the length along the inspection path through the step and linear wedges in the *Y*-axis are minimised. The effective thickness d_{eff} of each thickness d as a function of the X-ray inspection angles is:

$$d_{eff} = \frac{d}{\cos q},$$
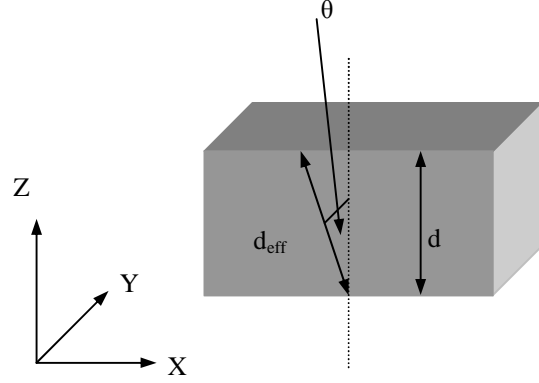
where d is the thickness (normal to plane of translation) of the step or linear wedges and θ is the X-ray inspection angle. The collection of calibration data is repeated to ensure that an accurate collection of 'thickness samples' are scanned to reduce aliasing effects.

The wedges' effective atomic number Z_{eff}, mass density ρ and thickness d along the wedge are applied to derive the coefficients of *Equ 4-12* and *Equ 4-13*:

$$IL = IH = 1: \qquad \frac{r_S}{Z_{eff}^{\ k}} = N_{IL1} \times Z_{eff}^{\ K_{IL1}}; \qquad \frac{r_S}{Z_{eff}^{\ k}} = N_{IH1} \times Z_{eff}^{\ K_{IH1}},$$

$$IL = IH = 2: \qquad \frac{r_S}{Z_{eff}^{\ k}} = N_{IL2} \times Z_{eff}^{\ K_{IL2}}; \qquad \frac{r_S}{Z_{eff}^{\ k}} = N_{IH2} \times Z_{eff}^{\ K_{IH2}},$$

……

……

$$IL = IH = 255: \qquad \frac{r_S}{Z_{eff}^{\ k}} = N_{IL255} \times Z_{eff}^{\ K_{IL255}}; \qquad \frac{r_S}{Z_{eff}^{\ k}} = N_{IH255} \times Z_{eff}^{\ K_{IH255}},$$

where k, N_{ILi}, N_{IHi}, K_{ILi}, and K_{IHi}, i=1, 2, 3 ……, 255, are determined by using *Levenberg-Marquardt* polynomial least square fitting algorithm.

Step Wedge   Linear Wedge

Incident X-ray
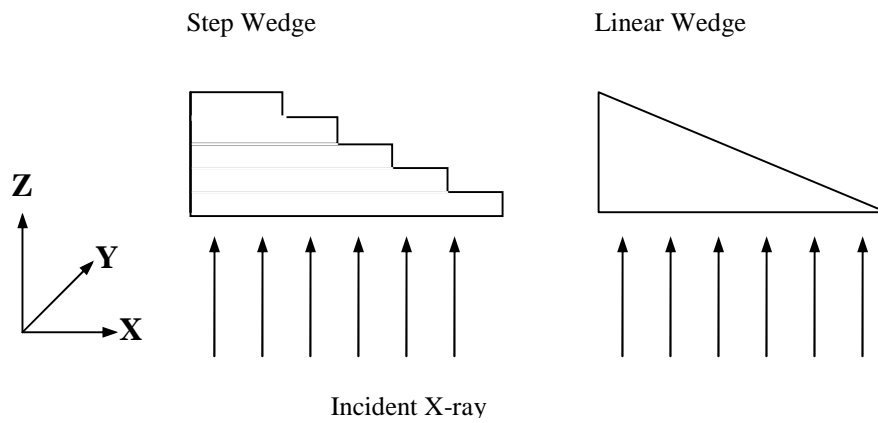
Fig. 4.1. The arrangement of the step and the linear wedges for the calibration procedure.

Array Detectors

Slit Collimator

Wedge Position

Tray Plane

Filter

Spot X-ray Source
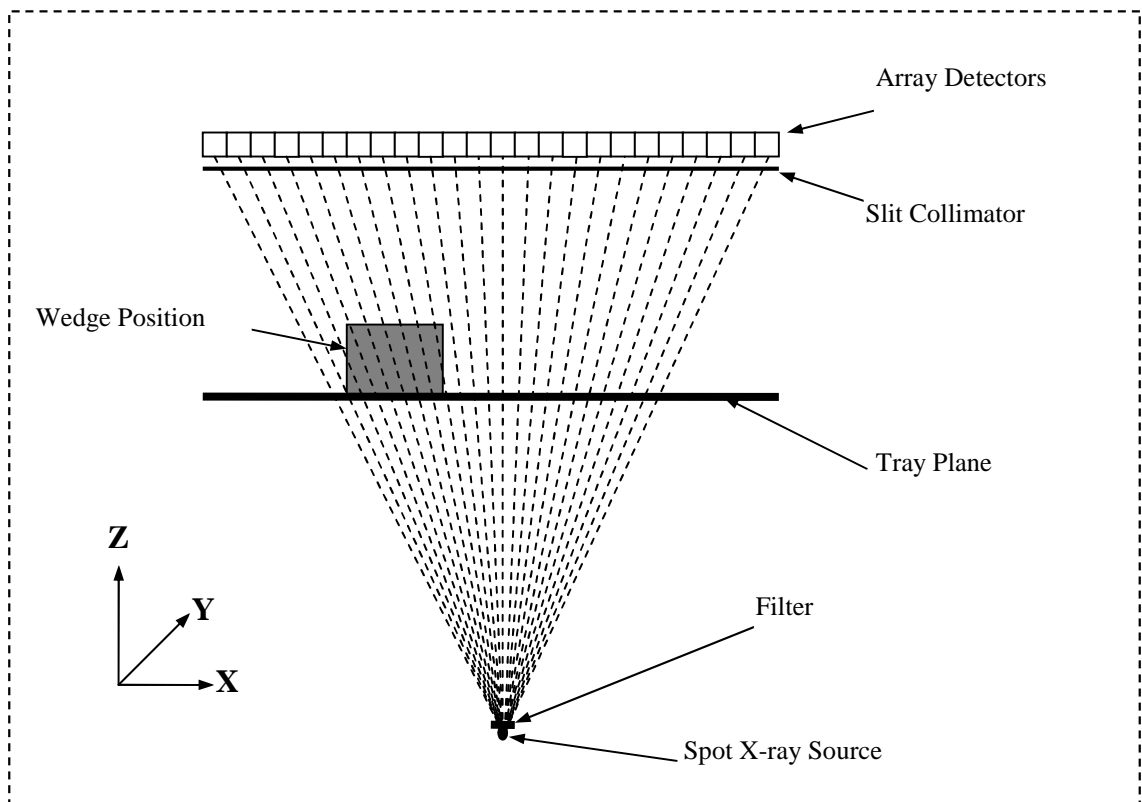
Fig. 4.2. X-ray image intensifierd CCD camera or detector array.

4.2.4 Calibration results for the K-II technique

The calibration procedure utilises a *Fe* linear wedge (from 0.1 mm to 10 mm) and four other step wedges manufactured from *Pl*, *PTFE*, *Al*, and *Titanium* respectively. The dimensions of the step wedges are stated in *Table 4-1*. Results for the dual-energy calibration are obtained by scanning the whole *Fe* linear wedge and 5 steps each of the four other step wedges. Regression of results, by applying 4th order polynomial equations, is illustrated in *Fig. 4.3 (a)* and *Fig. 4.3 (b)*.

	Pl (mm)	PTFE (mm)	Al (mm)	Ti (mm)
Step 1	8.0	6.7	4.0	1.0
Step 2	21.0	13.3	6.0	2.0
Step 3	31.0	20.0	8.0	3.0
Step 4	63.0	33.3	15.0	4.0
Step 5	104.0	52.2	35.0	5.0

Table 4-1 Step sizes of the Pl, PTFE, Al, and Ti step wedges.
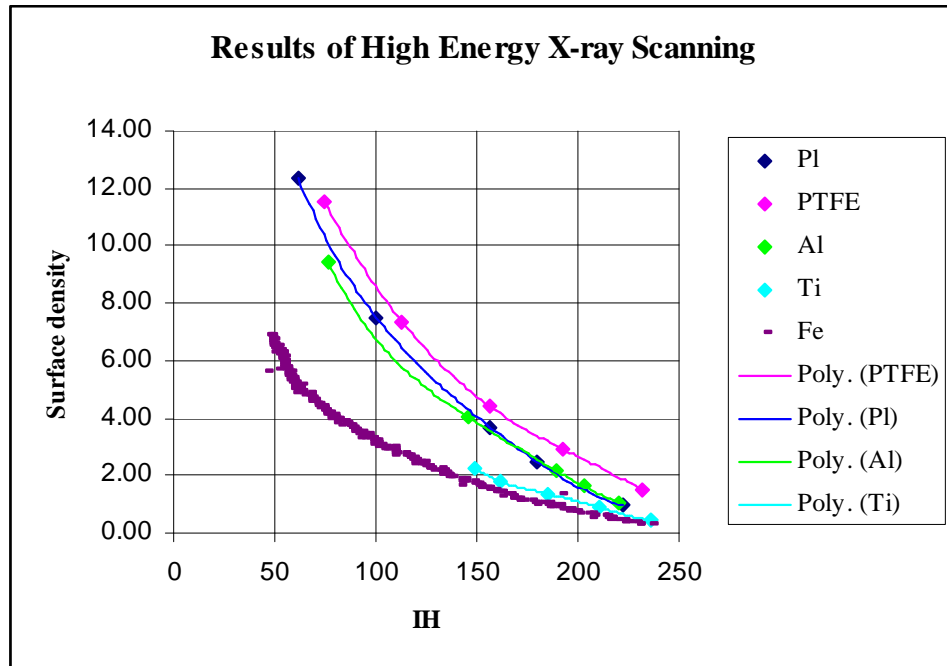
Fig. 4.3. (a) Results for high energy X-ray scanning; five steps of each step wedge and a linear wedge.
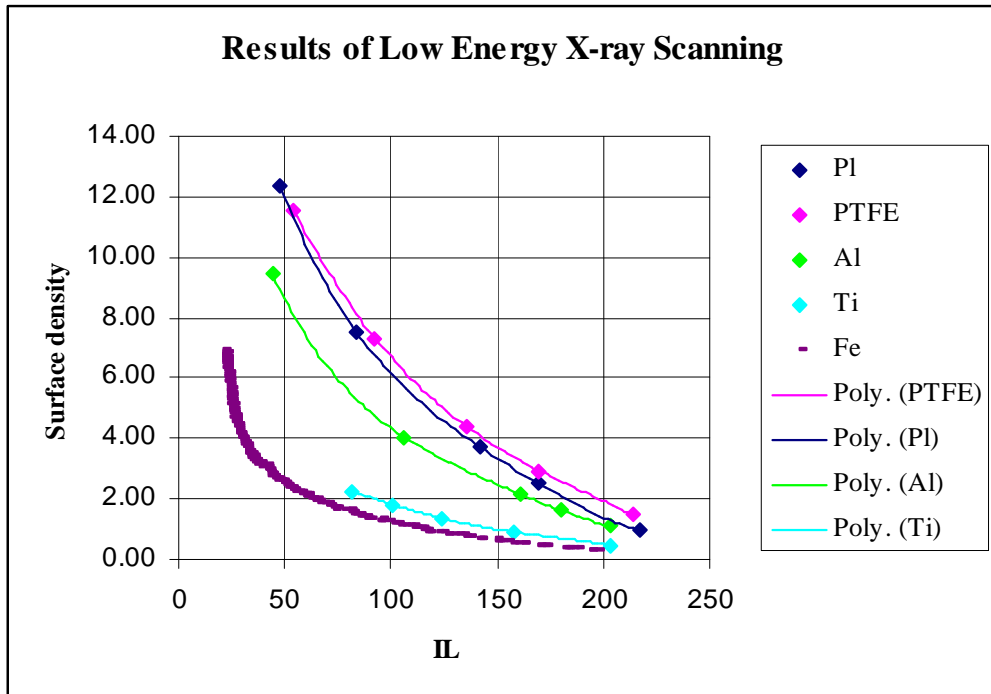
Fig. 4.3. (b) Results for low energy X-ray scanning; five steps of each step wedge and a linear wedge.

The coefficients of N_{ILi}, N_{IHi}, K_{ILi}, and $K_{IHi,}$ $i = 1, 2, 3$ ……, 255, are determined from the polynomial least square fitting *Levenberg-Marquardt* algorithm. Results (*i*=50, 100, 150, and 200) are listed in *Table 4-2* and *Table 4-3*. The empirical results for coefficient *k* is constant 25. Substituting the value of coefficients into *Equ 4-12* and *Equ 4-13* enables the range of material thickness along the inspection path to be estimated. *Fig. 4.4*, *Fig. 4.5* and *Fig. 4.6* illustrate the deviation of the calculated thickness from the true thickness of the *Pl*, *Al*, and *Ti* step wedges. The minimum and maximum residuals for the estimation of *Pl*, *Al*, and *Ti* step wedges thickness' are {-4.3, +2.38} mm, {-2.1, +0.37}mm, and {-0.38, +0.39}mm respectively.

i	Low Energy			High Energy		
	k	$N_{ILi}\times10$	K_{ILi}	k	$N_{IHi}\times10$	K_{IHi}
50	25	21.70	-26.35	25	98.4	-25.85
100	25	13.00	-26.40	25	52.5	-25.85
150	25	7.01	-26.40	25	2.71	-25.87
200	25	5.77	-26.62	25	1.86	-25.97

Table 4-2 Empirical results for the coefficients k, NILi, and KILi.

Z	Signal		Signal + Noise		Z	$\lvert \Delta Z \rvert$
	High	Low	High	Low		
6	64	51	65	50	5.8	0.2
6	230	228	231	227	6	0
6	151	139	152	138	5.9	0.1
13	82	51	83	50	13.2	0.2
13	230	221	231	220	13.1	0.1
13	179	140	180	139	13.1	0.1
26	120	51	121	50	26.4	0.4
26	230	188	231	187	26.3	0.3
26	176	101	177	100	26.4	0.4

Table 4-3 Effect of Noise on Atomic Number Calculation.

The accuracy of the K-II method is limited by a boundary condition, which depends on the system noise. It can be deduced from *Fig 3.7* and *Table 3-1* that the noise magnitude after normalisation for both high and low energies is less than 1 grey level. Hence, ±1 grey level is used as the noise magnitude for deciding the boundary condition over a range of atomic number. Table 4-3 tabulates the empirical result for three atomic numbers. "Signal" refers to the unmodified image intensity while "Signal + Noise" denotes the addition of the noise magnitude. It can be observed that the deviation in atomic number as a result of adding noise is less than 0.5 per atomic number. Hence it is decided that "0.5" is chosen as the boundary termed minimum resolvable atomic number increment. Please refer to Appendix D for the tabulation of the calibration results.
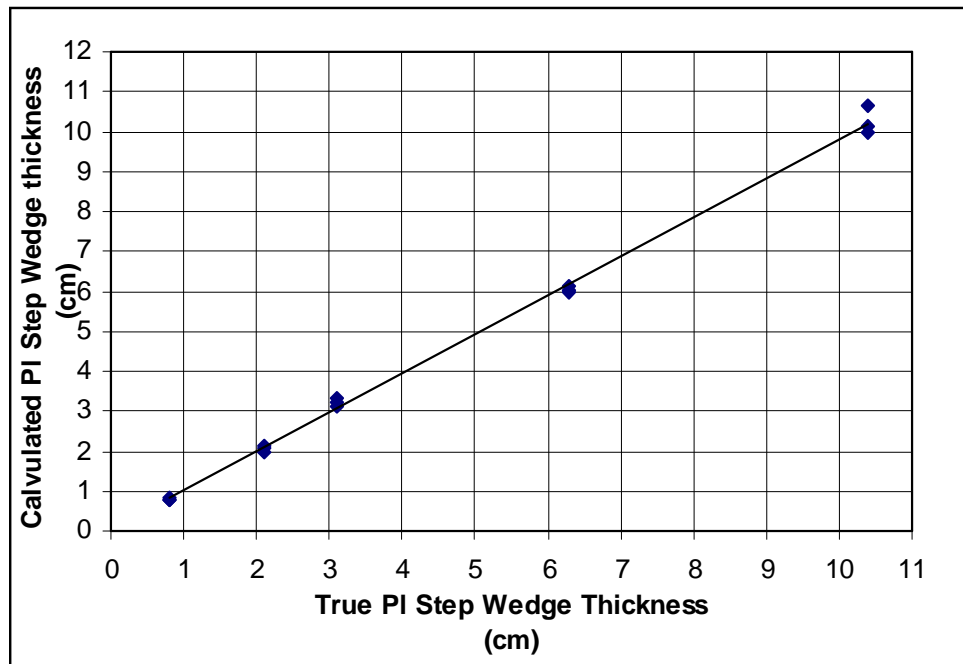
Fig. 4.4. The deviation of the calculated Pl step wedge thicknesses from their true values.
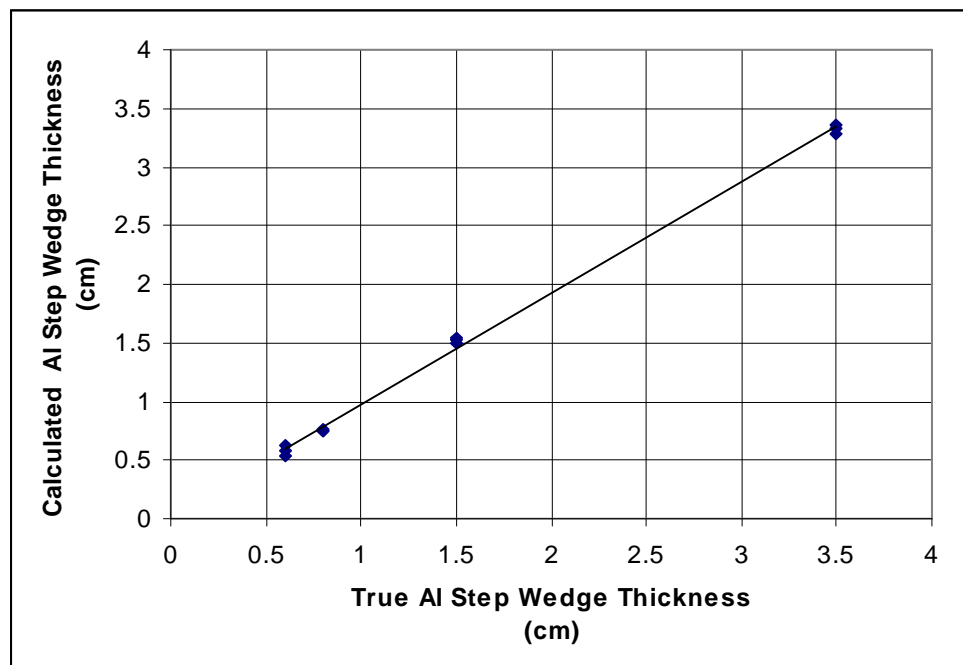
Fig. 4.5. The deviation of the calculated Al step wedge thickness from the true value.
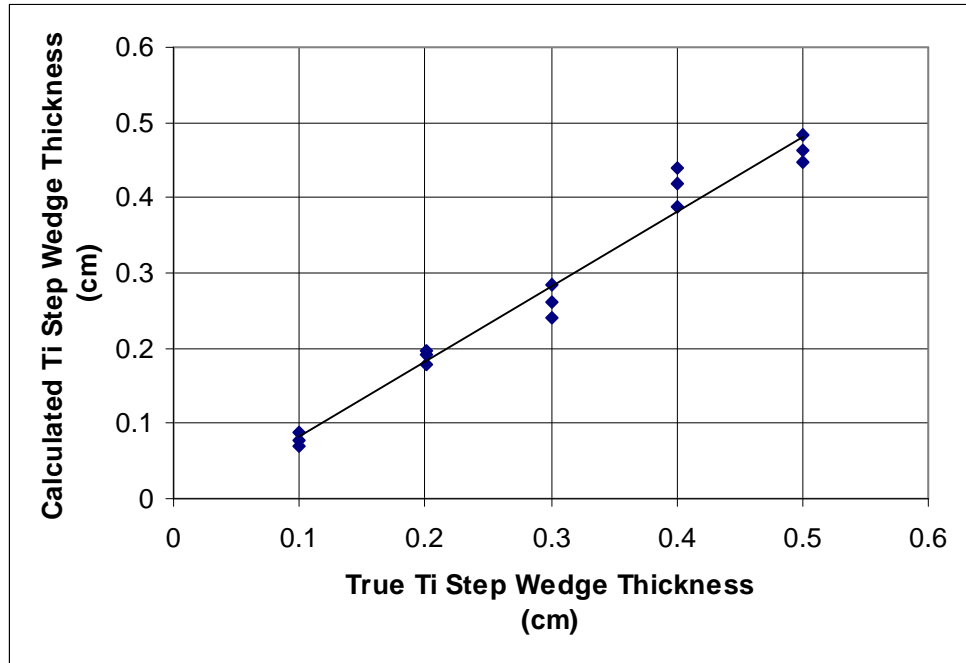
Fig. 4.6. The deviation of the calculated Ti step wedge thicknesses from their true values.

4.2.5 Experiments employing the K-II technique

The K-II technique is restricted to materials with known thicknesses and without the presence of masking materials. This phase of experimental work is conducted manually to evaluate the influence of material categories, thickness, and X-ray inspection angle to examine the reliability and precision of K-II technique in discrimination.

Influence of material categories

The material categories, which are introduced by prior researchers and widely adopted in the security industry, are divided into three groups, namely; organic, mixture and metal. The selection of different material samples enabled each of the three groups to be tested. Series materials enables all categories of material, with their respective thicknesses are selected for experiments and the results are stated in *Table 4-4*. The

deviation of calculated effective atomic number and mass density from their true values are illustrated in *Fig. 4.7* (a) and (b).

S	Material	Chemical formula	d (cm)	Z	K-Z	$\lvert \Delta Z \rvert$	ρ (g/cm^3)	K-ρ (g/cm^3)	$\lvert \Delta\rho \rvert$ (g/cm^3)
01	PPOm	C_8H_8O	3.30	6.10	6.30	0.20	1.06	1.08	0.02
02	PEI	$C_{37}H_{24}O_6N_2$	2.50	6.30	6.60	0.30	1.27	1.39	0.12
03	PMMA	$C_5H_8O_2$	4.90	6.46	6.10	0.36	1.10	1.05	0.05
04	POMC	CH_2O	3.60	6.95	6.90	0.05	1.41	1.44	0.03
05	PVDF	$C_2H_2F_2$	3.60	7.88	7.60	0.28	1.76	1.79	0.03
06	PTFE	C_2F_4	2.67	8.44	8.40	0.04	2.20	2.23	0.03
07	Silicon Nitride (cold pressed)	Si_3N_4	0.50	12.10	12.60	0.50	2.40	2.78	0.38
08	Silicon Nitride (hot pressed)	Si_3N_4	0.50	12.10	12.60	0.50	3.11	3.42	0.32
09	Al	Al	1.50	13.00	13.30	0.30	2.70	2.57	0.13
10	Titanium	Ti	0.30	22.00	22.20	0.20	4.50	4.46	0.04
11	Iron	Fe	0.15	26.00	26.30	0.30	7.78	8.05	0.27
12	Copper	Cu	0.1	29.00	28.60	0.40	8.96	9.20	0.24

Table 4-4 Emperical results for influence of material categories.

*S: Sample;   *d: Thickness;
*Z: True atomic number;   *ρ: True mass density;
*K-Z: K-II technique calculated atomic number;   *K-ρ: K-II technique calculated mass density.

(a)
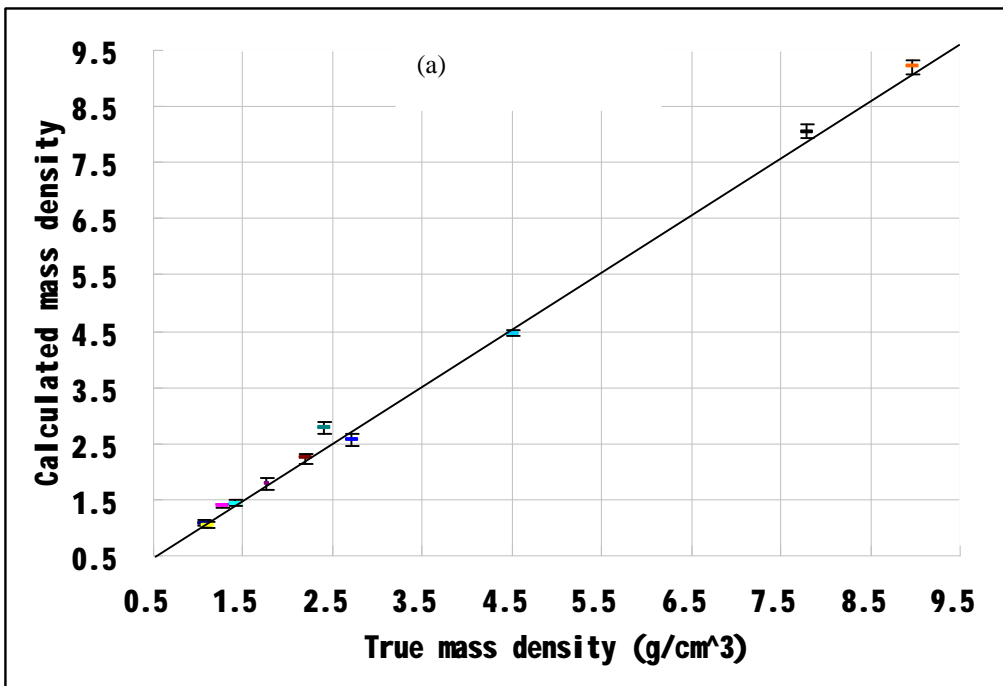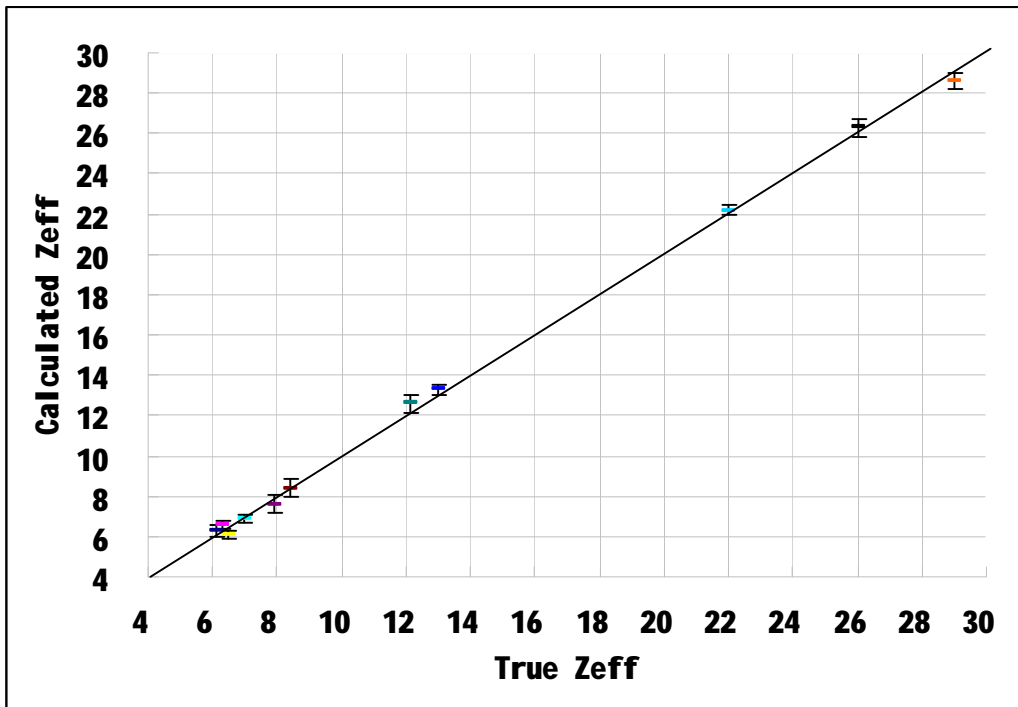
(b)

Fig. 4.7. The deviation of the calculated (a) effective atomic number and (b) the mass density from their true values

Influence of thickness

Three step wedges manufactured from *Pl*, *Al*, and *Ti* respectively are selected for further experiments. For the true thickness of each step, the deviations of the computed effective atomic number $|\Delta Z|$ and mass density $|\Delta\rho|$ from their true values are presented in *Table 4-5* and of each thickness of samples are illustrated in *Fig. 4.8*.

S	Material	d (cm)	Z	K-Z	$|\Delta Z|$	ρ (g/cm3)	K-ρ (g/cm3)	$|\Delta\rho|$ (g/cm3)
01	PMMA	0.80	6.46	6.00	0.46	1.19	1.13	0.06
02	PMMA	3.10	6.46	6.50	0.04	1.19	1.19	0.00
03	PMMA	6.30	6.46	6.00	0.46	1.19	1.14	0.05
04	PMMA	10.40	6.46	6.00	0.46	1.19	1.14	0.05
05	Al	0.60	13.00	13.50	0.50	2.70	2.42	0.28
06	Al	0.80	13.00	13.50	0.50	2.70	2.58	0.12
07	Al	1.50	13.00	13.50	0.50	2.70	2.68	0.02
08	Al	3.50	13.00	13.00	0.00	2.70	2.54	0.16
09	Titanium	0.20	22.00	22.50	0.50	4.50	4.00	0.50
10	Titanium	0.30	22.00	22.50	0.50	4.50	4.00	0.50
11	Titanium	0.40	22.00	21.50	0.50	4.50	4.95	0.45
12	Titanium	0.50	22.00	22.00	0.00	4.50	4.36	0.14

Table 4-5 Emperical results for the influence of material thickness.
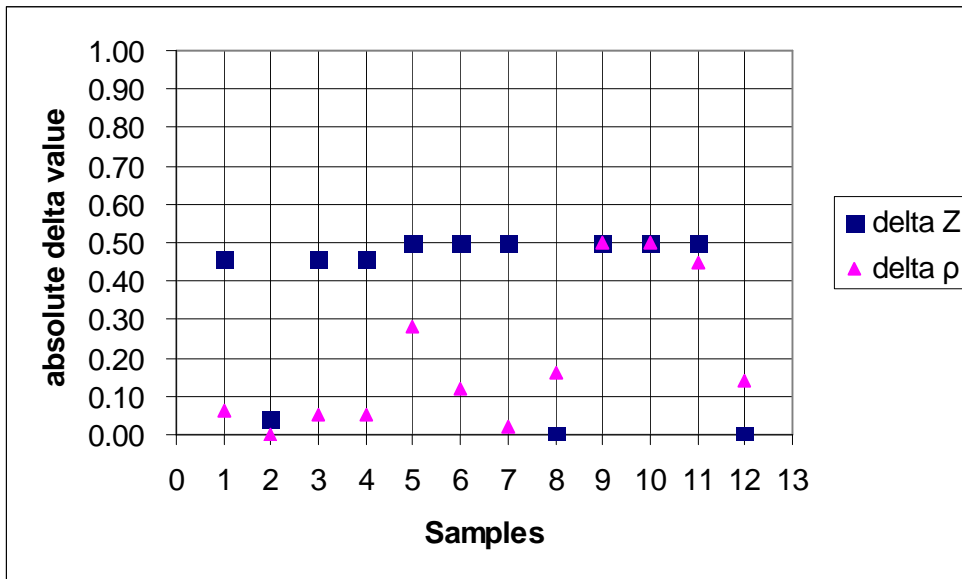
Fig. 4.8. $\left|\Delta\right|$ **for samples varying in thickness.**

Influence of the X-ray inspection angle

Pl, Al, and *Ti* rectangular plates are placed at three different angles,-3°, 0°, and $+4^{o}$ about the *Y*-axis to establish any effect on the computed values of $\left|\Delta Z\right|$ and $\left|\Delta\rho\right|$. The results are presented in *Table 4-6* and $\left|\Delta Z\right|$ and $\left|\Delta\rho\right|$ are illustrated in *Fig. 4.9*.

S	Material	angle (o)	Z	K-Z	$\left|\Delta Z\right|$	ρ (g/cm3)	K-ρ (g/cm3)	$\left|\Delta\rho\right|$ (g/cm3)
01	PMMA	0	6.46	6.00	0.46	1.19	1.17	0.02
02	Al	0	13.00	13.50	0.50	2.70	2.51	0.19
03	Titanium	0	22.00	22.50	0.50	4.50	4.29	0.21
04	PMMA	-3	6.46	6.00	0.46	1.19	1.21	0.02
05	Al	-3	13.00	13.50	0.50	2.70	2.50	0.20
06	Titanium	-3	22.00	22.50	0.50	4.50	4.39	0.11
07	PMMA	+4	6.46	6.00	0.46	1.19	1.12	0.07
08	Al	+4	13.00	13.50	0.50	2.70	2.58	0.12
09	Titanium	+4	22.00	22.50	0.50	4.50	4.14	0.36

Table 4-6 Emperical results for influence of X-ray inspection angle.
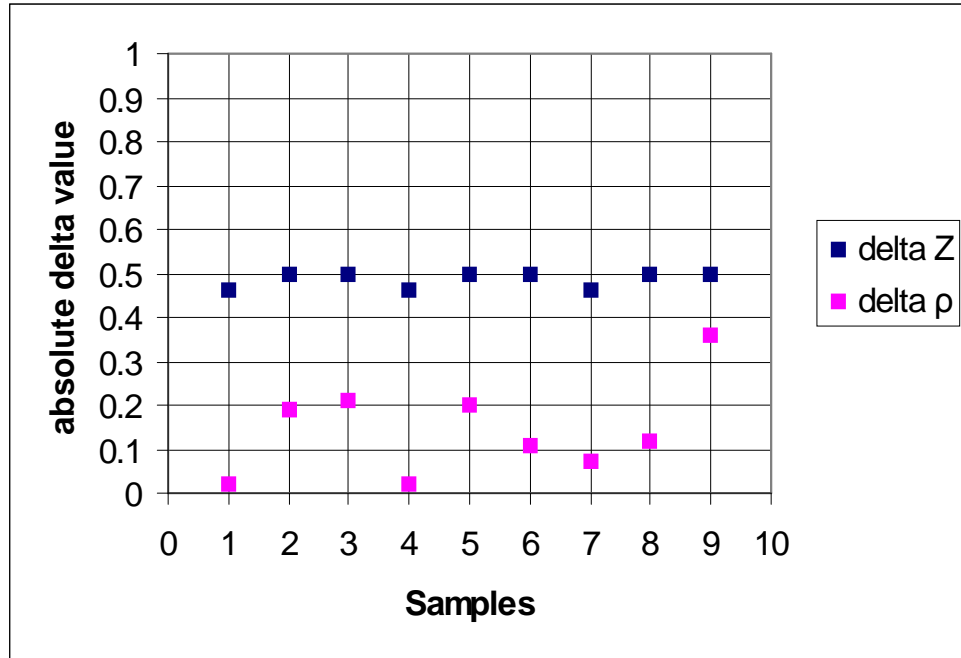
Fig. 4.9. │ Δ │ **for samples at different X-ray inspection angles.**

4.2.6 Summary

The K-II technique is developed for measuring material effective atomic number Z_{eff} and mass density ρ of a scanned object with a known thickness. Its main feature is to simulate the interdependence of atomic number, mass density and thickness for a certain amount of X-ray attenuation. This method, unlike the *BMS* method, which is limited to discriminating the effective atomic number of a material within a boundary from say 6 to 13, is able to discriminate a wide range of materials. In this research, the focus is on common materials typically exhibiting atomic numbers less than 30. Quantitative data are collected from a series of experiments to evaluate the influence of material categories, thickness and X-ray inspection angle.

In material categories experiment, which atomic numbers are ranged from 6 to 29. The absolute precisions of ΔZ=0.29 with a standard deviation 0.15 and $\Delta\rho$=0.14 g/cm^3 with

a standard deviation 0.13. The mean accuracy of the calculated material effective atomic number and mass density are 97.30% and 95.08% respectively.

Thicknesses of selected samples ranged from 0.2 cm to 10.4 cm. The absolute precisions of ΔZ=0.37 with a standard deviation 0.21 and $\Delta \rho$=0.19 g/cm^3 with a standard deviation 0.19. The mean accuracy of the calculated material effective atomic number and mass density are 96.64% and 94.14% respectively.

For the influence of X-ray inspection angle, tested at -3°, 0°, and +4°, it is found that the absolute precisions of ΔZ=0.34 with a standard deviation 0.01 and $\Delta \rho$=0.09 g/cm^3 with a standard deviation 0.05. The mean accuracy of calculated material effective atomic number and mass density are 96.88% and 94.76% respectively.

Considering all influences, the K-II technique produces mean absolute precisions of ΔZ=0.33 with a standard deviation 0.12 and $\Delta \rho$=0.14 g/cm^3 with a standard deviation 0.12 and mean accuracy of calculated material effective atomic number and mass density are 96.94% and 94.66% respectively. Furthermore, experiments on Silicon Nitride (hot pressed) and Silicon Nitride (cold pressed) validated that the K-II technique enables distinguishing the samples with the same effective atomic number and different mass density.

The conventional materials discrimination curves employ average atomic number to generate the material classification boundaries and resultant colour encoding scheme. The average atomic number is computed by the simplest numerical calculation, which is different from material effective atomic number. Using average atomic number might produce very significant noise in materials discrimination space and consequently uncertainty in X-ray image colourisation. Calculating several selected points on the conventional materials discrimination curves shown in *Fig 4.10*, the results are shown in *Table 4-7*. It is established that the results calculated by utilising the K-II technique are closer to the true values than the results calculated by utilising the conventional materials discrimination curves: the accuracy of the discrimination results can be improved up to 98.85%. Accordingly, the improvement in discrimination accuracy, the

resultant colour artefacts can be potentially reduced, especially for images of objects comprised of materials exhibiting atomic numbers around the boundaries of the materials discrimination curves. This important consideration is further discussed in the Chapter five.

The K-II technique is a quantitative method. Its performance is strongly dependent on the stability of system. Consequently improvements to the imaging chain to reduce noise will improve the performance of the K-II technique in materials discrimination. Mathematically, the K-II technique employs polynomial equations to simulate the emitted and detected X-ray spectrum. Thus manufacturer's data concerning emitted X-ray spectrum, collimation, intensification, and detection efficiency could be used to replace the numerical simulation in the K-II technique and potentially improve the computation of effective atomic number. The K-II technique itself is limited by the requirement for material thickness to be known. Without knowing material thickness, the K-II technique is only able to discriminate material effective atomic number and surface density.
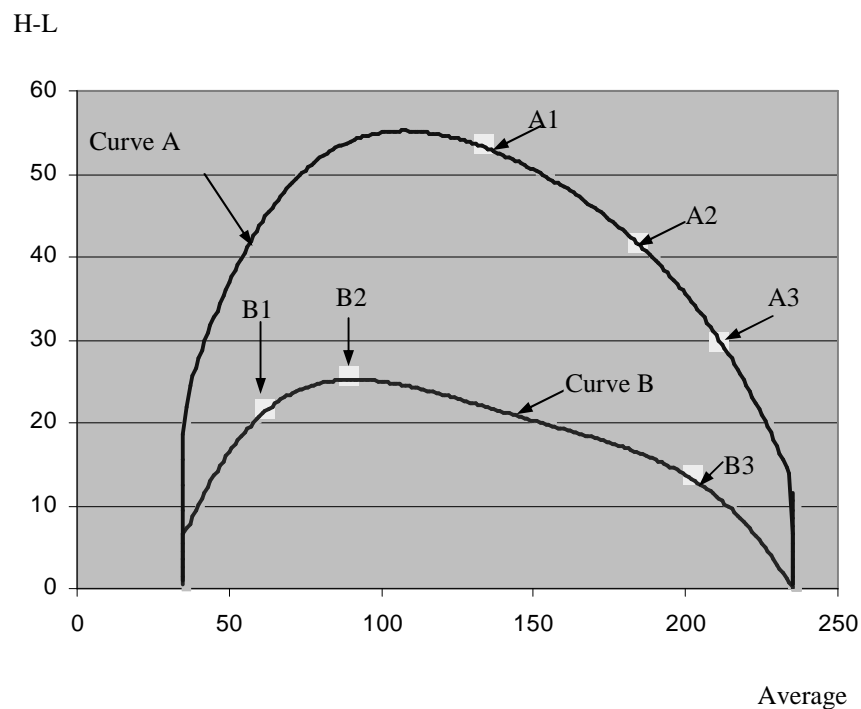
Fig. 4.10. Conventional materials discrimination curves with selected curves.

	Calculated Z_{eff}	MDC measured Z_{eff}	$\lvert \Delta Z \rvert$	%	K-II technique measured Value	$\lvert \Delta Z \rvert$	%
A1	18.35	19.50	1.15	93.73	18.00	0.35	98.09
A2	18.29	19.50	1.21	93.38	18.50	0.21	98.85
A3	18.27	19.50	1.23	93.26	19.00	0.73	96.01
B1	10.39	9.73	0.66	93.64	10.00	0.39	96.24
B2	10.37	9.73	0.64	93.82	10.00	0.37	96.43
B3	10.26	9.73	0.53	94.83	10.00	0.36	96.49

Table 4-7 Results for the K-II technique on selected points on conventional materials discrimination curves.

4.3 W-E Technique

The W-E technique enables the extraction of the surface density and material effective atomic number from overlapping objects. The W-E technique is a derivative of the relative mass increment and electron fraction, which may be applied to extract the surface density of layers according to the image intensity of the related area. Consequently, the material effective atomic number can be obtained by applying the surface density into the formula for effective atomic number calculation.

4.3.1 Extraction of surface density

Surface density is mass divided by surface area, which also equates to density multiplied by thickness.

Consider the overlapping materials *A*, *B*, and *C* as illustrated in *Fig. 4.11*, the X-ray propagated through thickness D_A of layer *A*, thickness D_A+D_B of layer *A* and *B*, and thickness $D_A+D_B+D_C$ of layer *A,B* and *C* can be utilised to compute the mass of the materials. Assuming, materials *A*, *B*, and *C* had mass density ρ_A, ρ_B, and ρ_C respectively. The mass (*W*) of material *A*, *B*, and *C* per unit area (*S*) are:

$$W_A = r_A \times D_A \times S, \qquad\qquad\qquad\qquad\qquad \text{Equ 4-14 (a)}$$

$$W_B = r_B \times D_B \times S, \qquad\qquad\qquad\qquad\qquad \text{Equ 4-14 (b)}$$

$$W_C = r_C \times D_C \times S. \qquad\qquad\qquad\qquad\qquad \text{Equ 4-14 (c)}$$

For layer *A* and *B* and layer *A*, *B* and *C*, the mass per unit area are:

$$W_{AB} = W_A + W_B = r_{AB} \times (D_A + D_B) \times S, \qquad\qquad \text{Equ 4-15 (a)}$$

$$W_{ABC} = W_{AB} + W_C = r_{ABC} \times (D_A + D_B + D_c) \times S. \qquad \text{Equ 4-15 (b)}$$

Substituting *Equ 4-14* (a), (b), and (c) into *Equ 4-15* (a) and (b), they are:

$$r_{AB} \times (D_A + D_B) \times S = r_A \times D_A \times S + r_B \times D_B \times S, \qquad \text{Equ 4-16 (a)}$$

$$r_{ABC} \times (D_A + D_B + D_c) \times S = r_{AB} \times (D_A + D_B) \times S + r_C \times D_C \times S. \qquad \text{Equ 4-16 (b)}$$

Replacing mass density by multiplying thickness with surface density *PS* and dividing unit area (*S*) in *Equ 4-16* (*a*) and (*b*), they were:

$$PS_{AB} = PS_A + PS_B, \qquad\qquad\qquad\qquad\qquad \text{Equ 4-17 (a)}$$

$$PS_{ABC} = PS_{AB} + PS_C. \qquad\qquad\qquad\qquad\qquad \text{Equ 4-17 (b)}$$

Applying the K-II technique, the surface density PS_A, PS_{AB}, and PS_{ABC} can be obtained according to the measured output image intensities of I_A, I_{AB}, and I_{ABC}. Substituting the obtained surface density into *Equ 4-17* (*a*) and (*b*), PS_B and PS_C can be obtained as well.
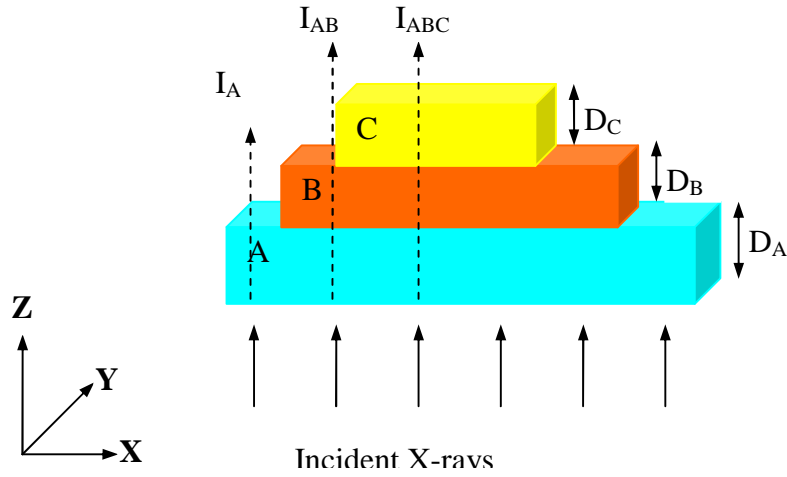
Fig. 4.11. Overlapping materials A, B, and C.

4.3.2 Derivation of effective atomic number for layered structure

Material effective atomic number is calculated by taking the fraction proportion of each atom in the compound and multiplying that by the atomic number of the atom. The formula of effective atomic number is:

$$Z = \sqrt[3.1]{f_1 \times Z_1^{3.1} + f_2 \times Z_2^{3.1} + f_3 \times Z_3^{3.1} \dots} \, , \qquad \text{Equ 4-18}$$

where *fn* is the fraction of the total number of electrons associated with each element, and Z_n is the atomic number of each element. For the mass [132] per unit area, it is:

$$W_{mass} = N_{atom} \times W_{atom} = r \times t \times S \, , \qquad \text{Equ 4-19}$$

where N_{atom} is the total number of atoms in the volume ($t \times S$) and W_{atom} is the mass per atom. More than 99.9% of an atom's mass is concentrated in the nucleus [133], with protons and neutrons having about equal mass. Thus, atom weight is:

$$W_{atom} \approx 2 \times Z \times W_{proton} \, , \qquad \text{Equ 4-20}$$

where W_{proton} is a constant (1.6726×10^{-24} g). Substituting *Equ 4-20* in *Equ 4-19*:

$$r \times t \times S \approx N_{atom} \times 2 \times Z \times W_{proton} \, . \qquad \text{Equ 4-21}$$

For an atom, this involves the same quantity of electrons and protons. The total electrons in W $_{atom}$ are:

$$N_{electron} = \frac{r \times t \times S}{2 \times Z \times W_{proton}} \, . \qquad \text{Equ 4-22}$$

Substituting *Equ 4-22* into *Equ 4-18*, produces a formula to calculate effective atomic number for overlapping materials:

$$Z = \sqrt[3.1]{PS_1 \times Z_1^{3.1} + PS_2 \times Z_2^{3.1} + PS_3 \times Z_3^{3.1} ......} ,$$
<div align="right">Equ 4-23</div>

where PS_n is the fraction of the total number of surface density associated with each objects, and Z_n is the effective atomic number of each object. For overlapping material *A*, *B*, and *C* as illustrated as *Fig. 4.11*, the effective atomic number Z_{ABC} is:

$$Z_{ABC} = \sqrt[3.1]{PS_{AB} \times Z_{AB}^{3.1} + PS_C \times Z_C^{3.1}} ,$$
<div align="right">Equ 4-24</div>

$$Z_{AB} == \sqrt[3.1]{PS_B \times Z_B^{3.1} + PS_A \times Z_A^{3.1}} ,$$
<div align="right">Equ 4-25</div>

where Z_A, Z_{AB}, Z_{ABC}, PS_A, PS_{AB}, and PS_{ABC} can be obtained by utilising the K-II technique with measured output image intensities of I_A, I_{AB}, and I_{ABC}. Subsequently combining the obtained results from K-II technique with surface density subtraction, PS_A, PS_B, and PS_C can be computed. Substituting subtracted surface densities and effective atomic numbers into *Equ 4-24* and *Equ 4-25*, enables the computation of Z_B and Z_C.

4.4 Experiments on Materials Discrimination of Layered Structures

The target is masked under several layers as illustrated in *Fig. 4.12*. The overlapping effect is accounted for by applying the K-II technique and W-E subtraction technique. The experiment is conducted manually to validate the K-II technique and W-E technique. The overlapping materials utilised in this experiments with their measured thicknesses are listed in *Table 4-8*. All three categories of materials are included to enable overlapping conditions to be tested. For example, the target object masked by an organic category material can be used to represent the situation of plastic explosive masked by clothes, shoes, glass, or books; the target object masked by a mixture category material may be used to indicate the situation of a threat masked by ceramic, *PVC* board, or rubber; the target masked by a metal category material may be used to simulate a threat hidden in a stainless steel can.
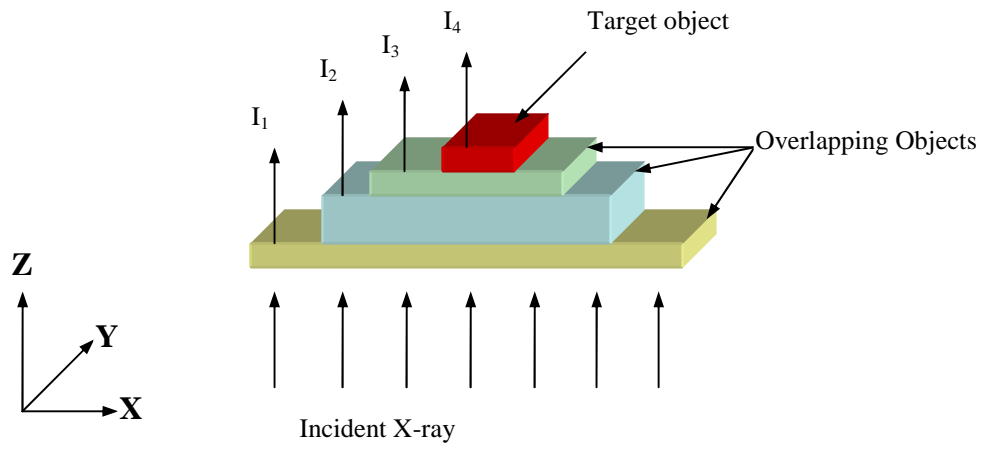
Fig. 4.12. Illustration of the target object and different overlapping objects.

Object	Chemical Formula	Z	ρ (g/cm^3)	Thickness (cm)
A	POMC	6.95	1.41	1.10
B	PVDF	7.88	1.76	1.20
C	TI	22.00	4.50	0.10
D	TI	22.00	4.50	0.20
E	PTFE	8.44	2.20	0.90
F	PPOM	6.10	1.06	1.10
G	PVC	13.9	1.40	0.40
H	AL	13.00	2.70	0.40
I	CU	29.00	8.96	0.10
J	SN (Hot pressed)	12.10	3.11	0.50
K	PMMA	6.46	1.19	2.10
L	PEI	6.30	1.27	1.00

Table 4-8 Overlapping materials.

4.4.1 Target: organic material (POMC)

A POMC plate is selected as a target object as its effective atomic number is similar to plastic explosive, as described in Chapter two. It is masked with one-layer, two-layers, three-layers, and four-layers of materials as illustrated in *Fig. 4.12*. Examples of the low-energy and the high-energy X-ray image for the target object masked by a single object and multiple-layer objects are illustrated in *Fig. 4.13* and *Fig. 4.14*.
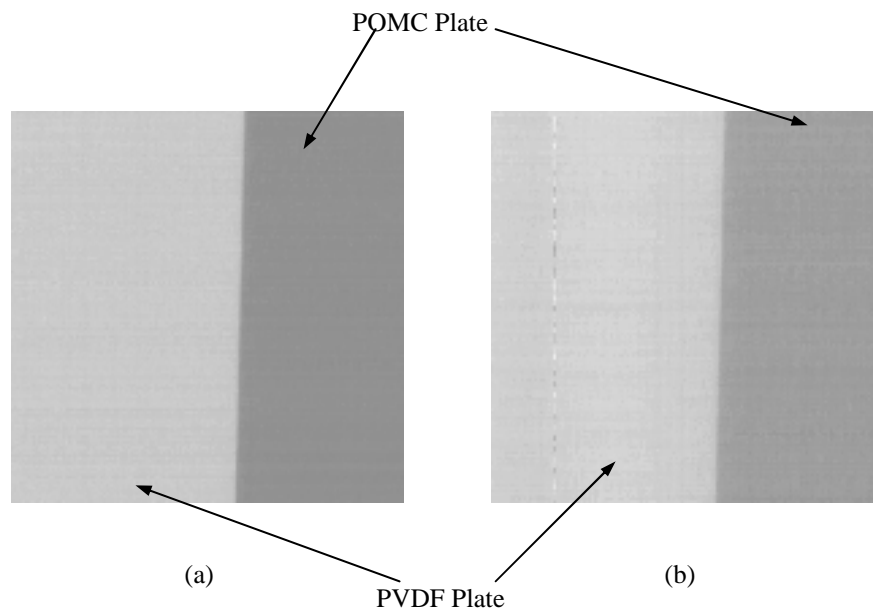
Fig. 4.13. Low (a) and high (b) energy X-ray images for a target object overlapping a single object (object B).

PVDF Plate

Ti Plate

PVC Plate

POMC Plate

(a)   (b)
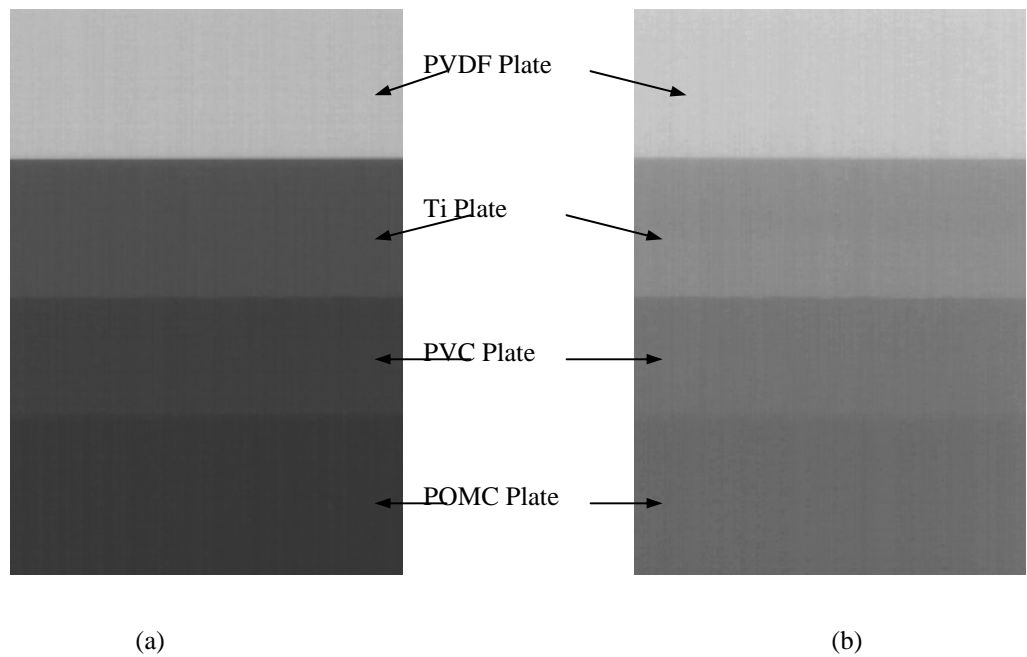
Fig. 4.14. Low (a) and high (b) energy X-ray images for target object overlapping multiple-layer objects (object B, C, and G)

The target object is discriminated from the masking objects and effective atomic number and surface density of the target object are computed by applying the K-II technique and the W-E technique. With the measured thickness of the target object, the mass density can be obtained. The results are shown in *Table 4-9*.

	OMC	Z	Z_C	$|\Delta Z|$	ρ (g/cm3)	ρ_C (g/cm3)	$|\Delta\rho|$ (g/cm3)
T overlapping B	Or	6.95	7.00	0.05	1.41	1.41	0.00
T overlapping G	Mi	6.95	6.50	0.45	1.41	1.37	0.04
T overlapping H	Mi	6.95	7.50	0.55	1.41	1.52	0.11
T overlapping F	Or	6.95	6.50	0.45	1.41	1.37	0.04
T overlapping B, E	Or	6.95	7.00	0.05	1.41	1.43	0.02
T overlapping H, I	Mi, Me	6.95	7.50	0.55	1.41	1.42	0.01
T overlapping B, C	Or, Me	6.95	7.00	0.05	1.41	1.41	0.00
T overlapping F, G	Or, Mi	6.95	6.50	0.45	1.41	1.37	0.04
T overlapping B, G	Or, Mi	6.95	7.50	0.55	1.41	1.50	0.09
T overlapping E, F, G	Or, Mi	6.95	6.50	0.45	1.41	1.37	0.04
T overlapping B, G, J	Or, Mi, Me	6.95	7.50	0.55	1.41	1.50	0.09
T overlapping B, G, J, I	Or, Mi, me	6.95	7.50	0.55	1.41	1.50	0.09

*T: Target object   *OMC: Overlapping material category
*Or: Organic material category   *Mi: Mixture material category
*Me: Metal material category   *Z_C: Calculated material effective atomic number
*ρ_C: Calculated material mass density

Table 4-9 The calculated results of material effective atomic number and mass density for POMC plate target for various overlapping materials.

4.4.2 Target: mixture material (Al)

An *Al* plate is selected as the target object to test the ability of K-II technique and W-E technique to discriminate the mixture material category from the overlapping objects. The *Al* plate is masked by one-layer, two-layers, and three-layer objects. With the measured thickness, the effective atomic number and mass density are extracted by applying the K-II technique and W-E technique. The results are shown in *Table 4-10*.

	OMC	Z	Z_C	$|\Delta Z|$	ρ (g/cm3)	ρ_C (g/cm3)	$|\Delta\rho|$ (g/cm3)
T overlapping A	Or	13.00	13.00	0.00	2.70	2.90	0.20
T overlapping B	Or	13.00	12.50	0.50	2.70	3.10	0.40
T overlapping A, I	Or, Me	13.00	13.00	0.00	2.70	2.90	0.20
T overlapping B, J	Or, Mi	13.00	12.50	0.50	2.70	3.10	0.40
T overlapping B, D	Or, Me	13.00	12.50	0.50	2.70	3.10	0.40
T overlapping B, D, J	Or, Mi, Me	13.00	12.50	0.50	2.70	3.10	0.40

Table 4-10 The calculated results of material effective atomic number and mass density for an Al plate target under various overlapping materials.

4.4.3 Target: metal material (Ti)

A target object of *Ti* plate is masked by one-layer, two-layer, and three-layer objects. With the measured thickness, the effective atomic number and mass density are extracted by apply K-II technique and W-E technique. The results are shown in *Table 4-11*.

	OMC	Z	Z_C	$|\Delta Z|$	ρ (g/cm3)	ρ_C (g/cm3)	$|\Delta\rho|$ (g/cm3)
T overlapping A	Or	22	22.8	0.8	4.5	4.2	0.3
T overlapping B	Or	22	22.7	0.7	4.5	5.0	0.5
T overlapping H	Me	22	22.0	0.0	4.5	4.8	0.3
T overlapping E	Mi	22	22.8	0.8	4.5	4.2	0.3
T overlapping A, B	Or	22	22.8	0.8	4.5	4.2	0.3
T overlapping B, H	Or	22	22.0	0.0	4.5	4.8	0.3
T overlapping A, B, E	Or	22	22.8	0.8	4.5	4.2	0.3
T overlapping B, H, J	Or, Me	22	22.0	0	4.5	4.8	0.3

Table 4-11 The calculated results of material effective atomic number and mass density for Ti plate target under various overlapping materials.

4.4.4 Summary

Considering the overall accuracy on calculating material effective atomic number and mass density of target objects mean absolute precisions of ΔZ=0.4 with a standard deviation 0.31 and $\Delta\rho$=0.24 g/cm^3 with a standard deviation 0.16 are recorded and the mean accuracy of calculated material effective atomic number and mass density are 96.53% and 92.35% respectively.

Comparing discrimination with and without mask, the overall performance is not significantly affected. This performance indicates that the W-E technique is workable and is able to assist the K-II technique to discriminate materials overlapped by several layers of different materials. However, the precision of discriminating a masked target is more dependent on system stability than discriminating without mask due to the noise propagation. A target object A (Z_A=6, PS_A=0.5) masked by one object B (Z_B=8, PS_B=0.5), assuming the calculated Z_{AB} is 7.55, which may, has an error of 0.4 greater than its true value. Subtracting object B, the effect atomic number of object A would be calculated as Z_A=7.1 which has 1.1 absolute difference from its true value. The accuracy drops to

81.67% which is lower than average recorded performance. It is also found that the greater atomic number difference between object *A* and *B*, the larger error might be produced during the extraction of target object.

In comparison with the conventional materials discrimination curves method and the *BMS* method, the W-E technique combined with K-II technique is able to obtain the correct material information for each layer of the overlapping structure. This feature is especially important for the security industry. In the case of an object masked by a steel container, the conventional materials discrimination curves might fail to discriminate the object from the container as it cannot subtract the overlapping structure and the *BMS* method cannot discriminate the object successfully due to its limited atomic number window. The false negative can cause a serious problem if there is for example an explosive in the container. However, both the W-E technique and the K-II technique are highly dependent on the stability of the system. An optimised scanning system is a key factor to achieving a successful discrimination by utilising the W-E technique and the K-II technique. In addition, either the K-II technique or the W-E technique has to employ with measured thickness to produce the effective results. In Chapter five, a method, which enables estimating the thickness of objects, is introduced. Combining the W-E technique and the K-II technique with the estimated thickness, give a potential way forward to realise the improved materials discrimination performance.

CHAPTER FIVE: THICKNESS ESTIMATION AND COLOUR ENCODING OF DISCRIMINATED MATERIALS INFORMATION

5.1 Introduction

This chapter describes the development of the thickness estimation technique using laminograms which are produced by employing the KDEX imagery. Associating the estimated thickness with the surface density, which is computed employing the K-II technique and the W-E technique mass density can be extracted. Consequently, the mass density coupled with effective atomic number enables discriminating the target materials from masks. Furthermore, a new colour scheme is introduced to highlight potential threat information in order to differentiate between threats and harmless organic materials. Empirical evidence is organised to demonstrate the effectiveness of the research proposal to discriminate the threats from multi-layered or complex structures.

5.2 Estimation of Object Thickness

Working with the K-II technique and the W-E technique, materials' effective atomic number and surface density are able to be computed. Surface density, itself, does not help discriminating materials until the thickness information is associated to produce mass density. With thickness information, mass density, which describes physical morphology of the absorbing material, can be derived from the surface density directly according to a linear function. Together with the computed material effective atomic number, which describes chemical classification of absorbing material, it enables discriminating the target materials in X-ray image of luggage (i.e. explosives) according to the *Fig. 2.3* illustrated in Chapter Two. In particular, the correct isolation of innocuous organic materials from threats is largely determined by density. In terms of successful materials discrimination process, the thickness information is indispensable.

In this research programme, the laminography technique is investigated to estimate the thickness of target object with the multiple-view X-ray image sequence.

5.2.1 Computed laminography in multiple-view X-ray imaging.

Different from traditional transmission X-ray and computed tomography (CT), computed laminography enables obtaining all object layers with only one measurement by sorting the data [134][135]. The computed laminography, which utilises similar setup of multiple-view X-ray imaging, is illustrated in *Fig. 5.1*.
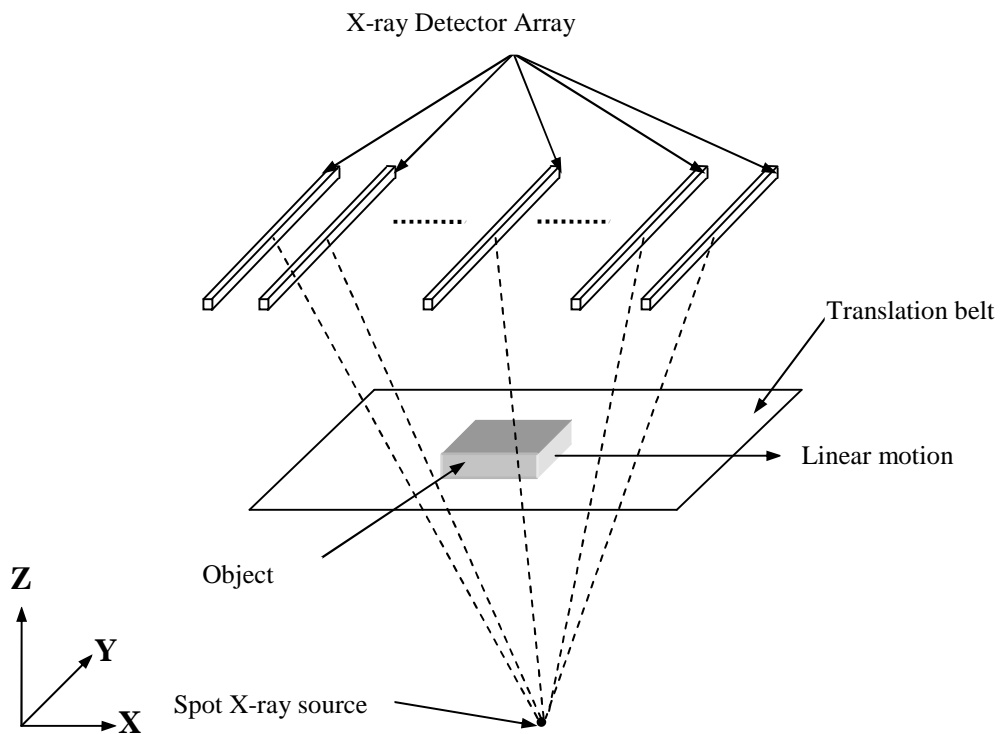

Fig. 5.1. Source/sensor configuration for computed laminography.

Laminograms may be obtained from multiple-view X-ray images assuming appropriate imaging geometry by applying the following equation:

$$L(x, y, m, D) = \frac{\sum\limits_{i=1}^{nInput} I_i(x + (i - m)D, y)}{nInput} ,$$ Equ 5-1[27]

where I_i refer to images from different view angle, $I_m(x,y)$ refers to the intensity of the pixel at position x, y in middle angle image (0°). D is the possible disparity between two images. $L(x,y,m,D)$ refers to the intensity of the pixel at position x, y of laminogram calculated using disparity D reference to the middle image. Accordantly, laminography technique enables estimating the target object's thickness by counting the laminograms between the focused features (corner, edge, and intense point on the surface) of selected region or objects. For example, selected features on the layered structure (i.e. A, B, and C), as illustrated in *Fig. 5.2*, can assist to estimate the thickness by observing and determining the laminograms where the selected features focus. As described in Section 2.4 that the success of the technique is limited the minimum depth increment of the imaging geometry. Hence, it should be noted the technique will inherently fail if the total thickness of several overlapping objects is less than or near to the minimum depth increment.
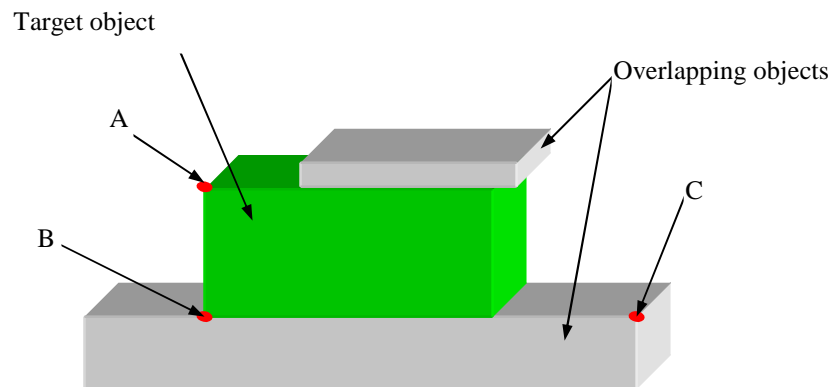

Fig. 5.2. Overlapping structure for the thickness estimation by laminography.

5.2.2 Experiments on laminography thickness estimation.

The system setup for this investigation is: 3° angle separation between adjacent views; 30 cm distance between X-ray source and detectors; 5 perspective views are selected: $+6^o$, $+3^o$, 0°, -3°, and -6°; sample size of scanning is 0.026cm. The minimum depth increment between two adjacent layers is 0.99 cm yielding a total of 30 laminograms. In the context of this research, the error band of the estimated thickness is ±0.5 cm. This investigation is divided into four separate experiments.

(a) Experiment 1: Experiment on thick objects

The experiment involved scanning a *PTFE* stepwedge with a step size of 0.9 cm (see *Fig. 5.3*) and one out of five resultant perspectives X-ray images are shown in *Fig. 5.4 (a)*.
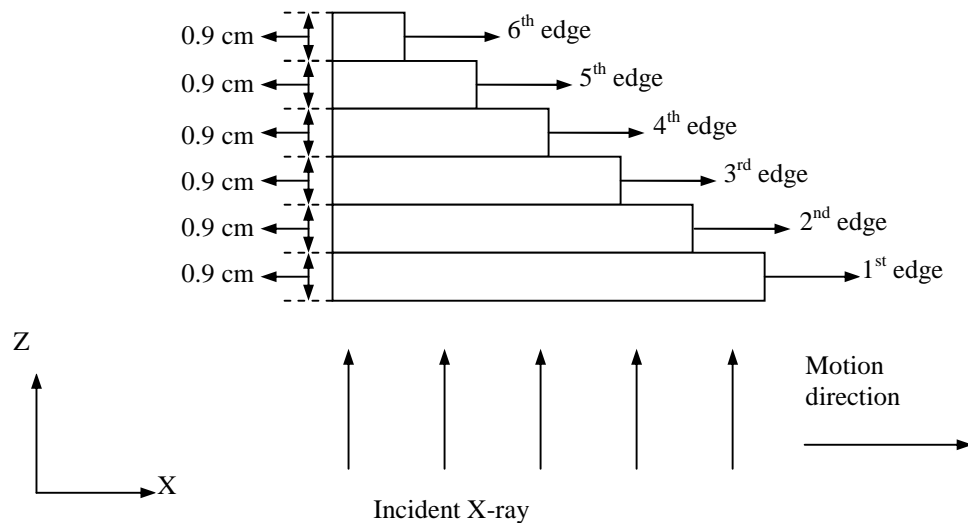

Fig. 5.3. Dimensions of the PTFE step wedge.

0°
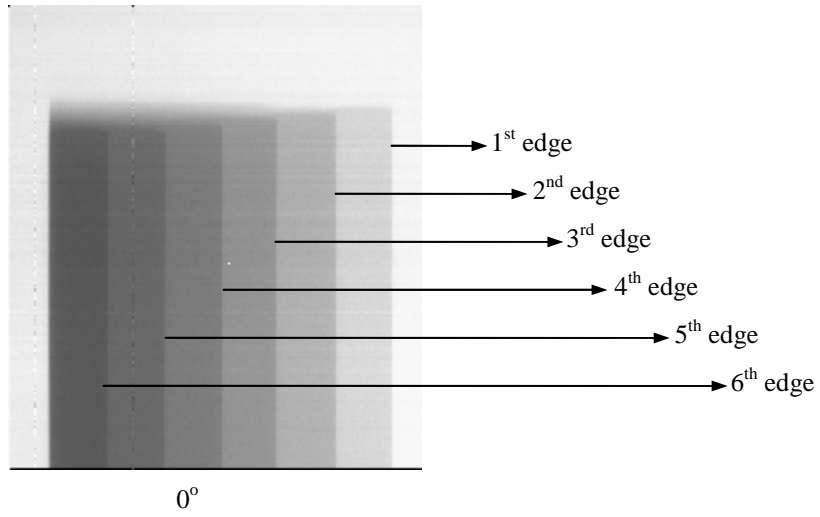
Fig. 5.4. (a) Multiple-view X-ray images of PTFE step wedges.

2nd laminogram


4th laminogram
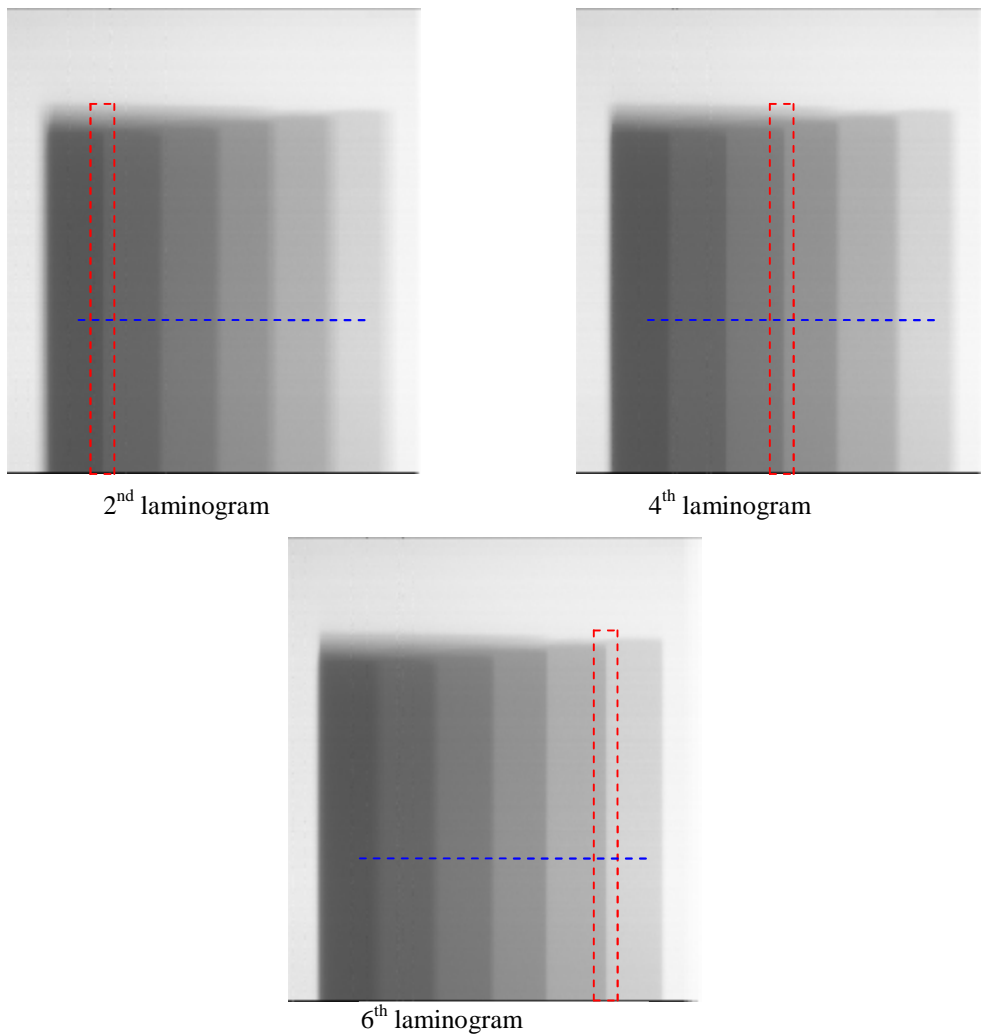
6th laminogram

Fig. 5.4. (b) 2nd, 3rd, 4th, 5th, 6th, and 7th laminograms of PTFE step wedge

Line profile of 2nd laminogram

Square of first derivative ($[dy/dx]^2$) of the line profile
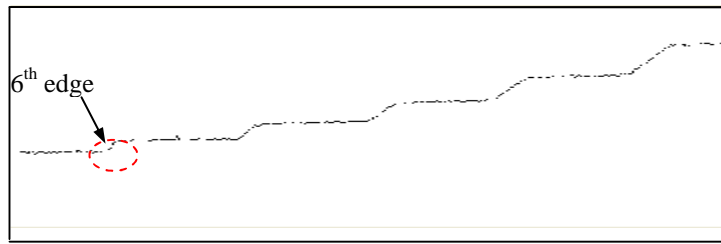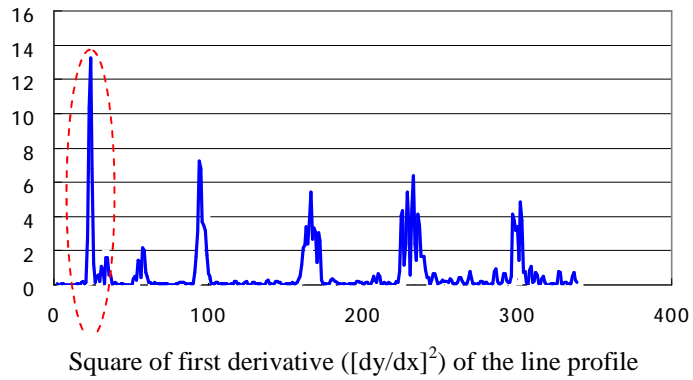
Fig.5.5. Line profile of 2nd laminograms and the square of its first derivative.
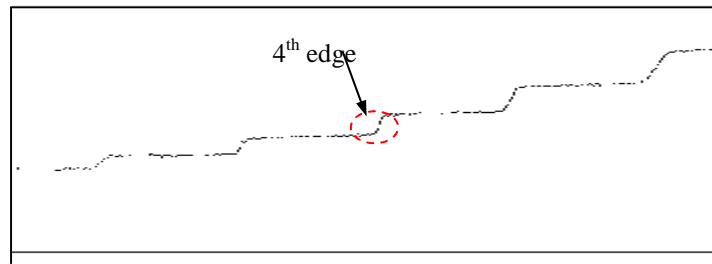
Line profile of 4th laminogram

Square of first derivative ($[dy/dx]^2$) of the line profile
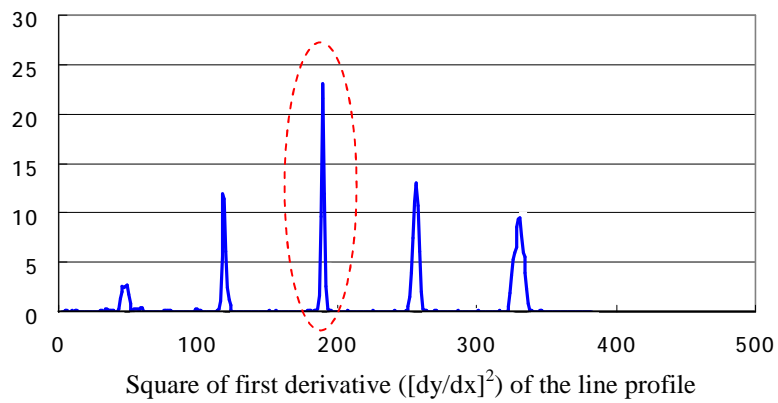
Fig.5.6. Line profile of 4'" laminograms and the square of its first derivative.

Line profile of 6th laminogram

Square of first derivative ($[dy/dx]^2$) of the line profile
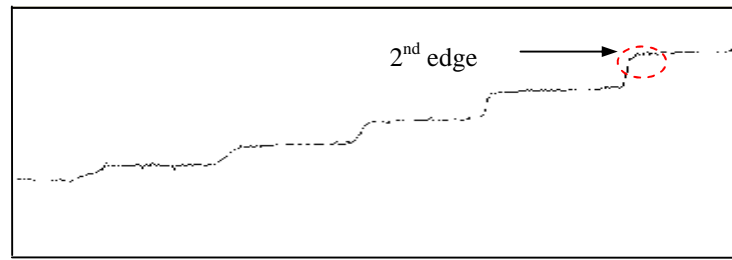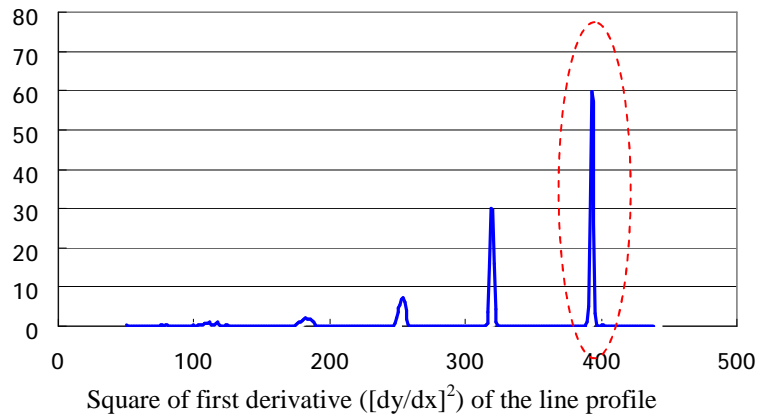
Fig.5.7. Line profile of 6th laminograms and the square of its first deviation.

In *Fig.5.4(b)*, the focused edges in each laminogram have been marked by red dashed rectangle. To aid the visualisation, the line profiles and the square of first deviation of the line profile of 2nd, 4th, and 6th laminograms are presented in *Fig. 5.5, Fig.5.6,* and *Fig.5.7*. The marked edges in *Fig.5.4(b)* produce larger peak value of the square of first derivation the other edges. The estimated thickness is 0.99 cm with the error band is ±0.5 cm. *Fig 5.8* illustrates the deviation of calculated thickness from the true thickness of the *PTFE* step wedge. The error of the estimated thickness increased proportionally with the true thickness.
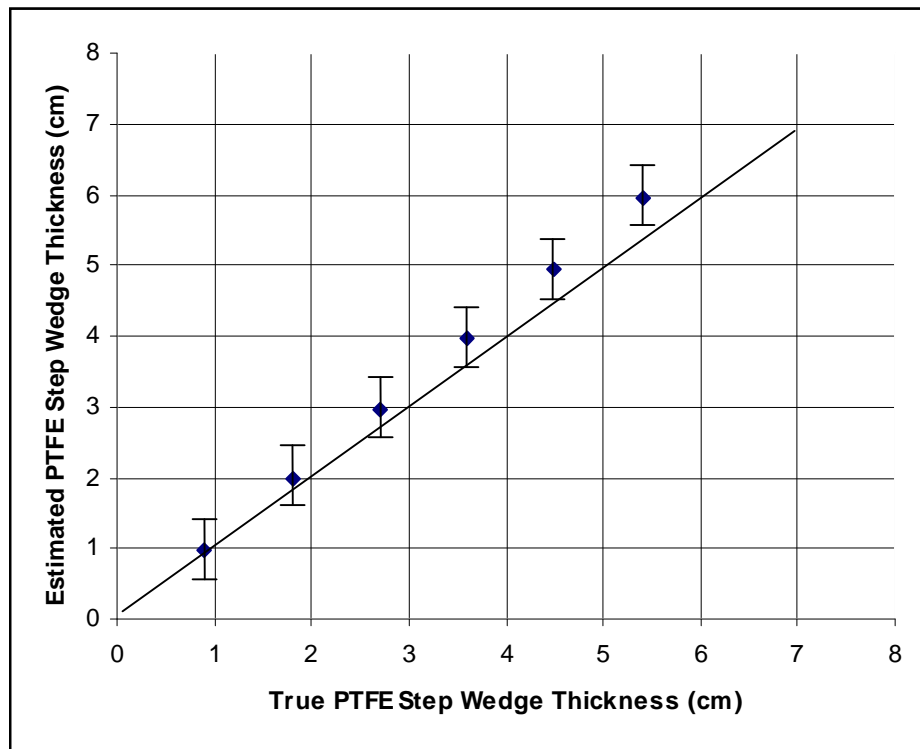
Fig. 5.8. The deviation of the calculated PTFE step wedge thickness from the true value.

(b) Experiment 2: Experiment on thin objects

This experiment involves a Titanium step wedge with a step thickness of 0.1 cm, which is much smaller than the minimum depth increment (by almost 10 times). It can be appreciated from the X-ray images and line profiles in *Fig. 5.9* that the whole titanium step wedge are focused on 13th laminogram. Also included the 15th laminogram for comparison. In this case, it is unable to estimate the thickness of each step of the Titanium step wedge.

13th laminogram   (a)   15th laminogram

Line profile of 13th laminogram

Line profile of 15th laminogram
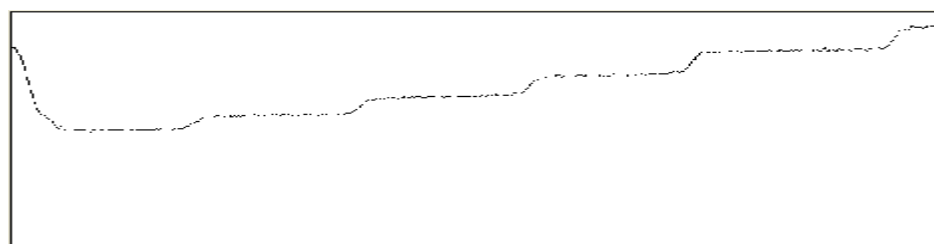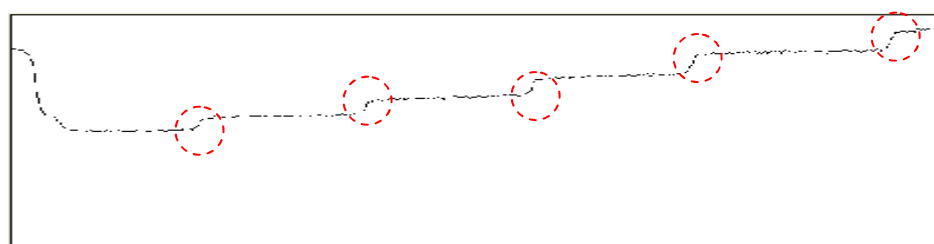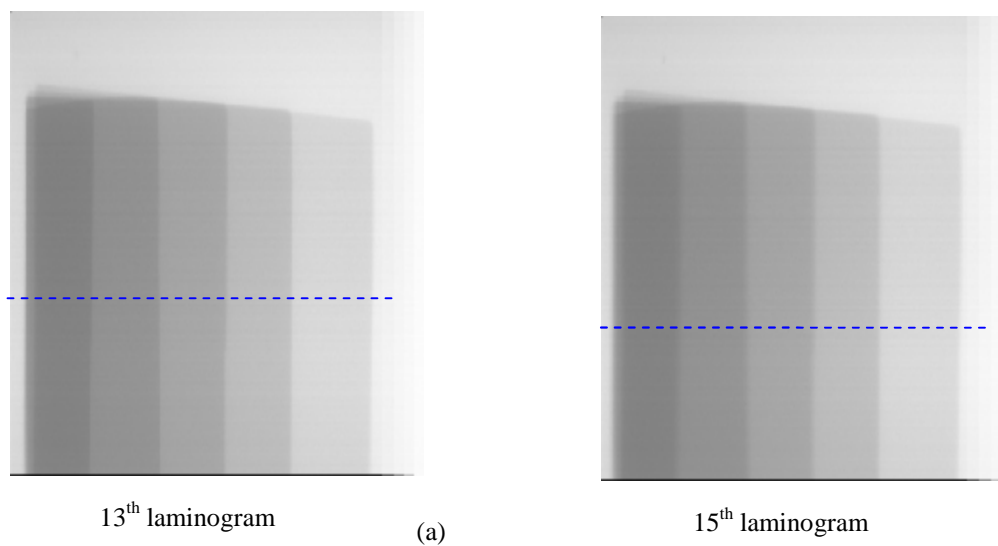
(b)

Fig. 5.9. (a) 13th and 15th laminograms of the Titanium step wedge and (b) line profile of the 13th and 15th laminograms.

(c) Experiment 3: Experiment on overlapping thin and thick objects

This experiment involves creating a five layered structure using both thin and thick objects. The structure consists of a *PVDF* plate (*d*=1.2cm), copper plate (*d*=0.1cm), *POMC* plate (*d*=1.1cm), *PVC* plate (*d*=0.4cm), and silicon nitride plate (*d*=0.5cm). The resultant X-ray images are shown in *Fig. 5.10*. The minimum depth increment is greater than the thickness of copper plate, *PVC* plate, and silicon nitride plate. The edges of each layer are marked by red rectangular box. It can be observed from *Fig. 5.11* that the edges of the *PVDF* and the copper plate are focused on the 15th laminogram; edge of the *POMC* plate is focused on the 16th laminogram; and edges of the *PVC* and the silicon nitride plate are focused on the 17th laminogram. Hence, the estimated thickness of the *PVDF* plus copper plate is 0.99 cm, the *POMC* plate was 0.99 cm, and the *PVC* plate plus the silicon nitride plate is 0.99 cm.
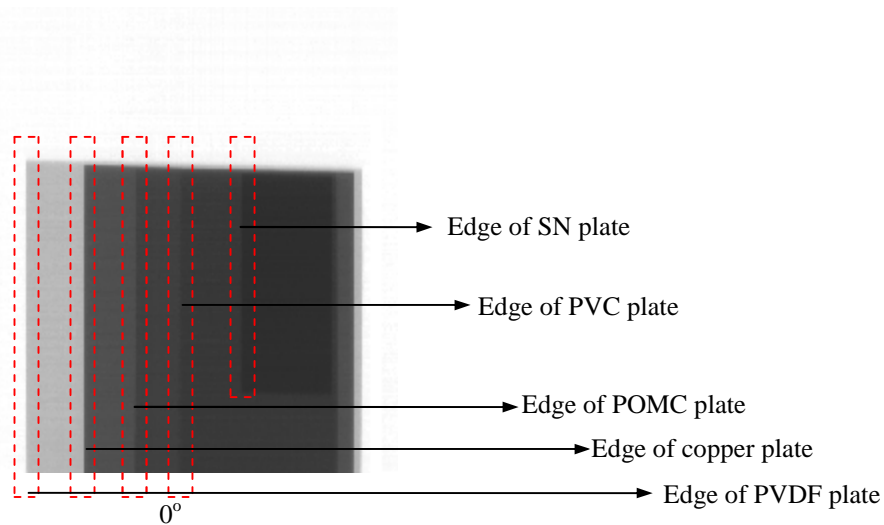
Fig. 5.10. Transmission image of the 5-layer structure.

PVDF and Copper edges are in focus

POMC edge is in focus

15th laminogram

16th laminogram

PVC and the silicon nitride edges are in focus
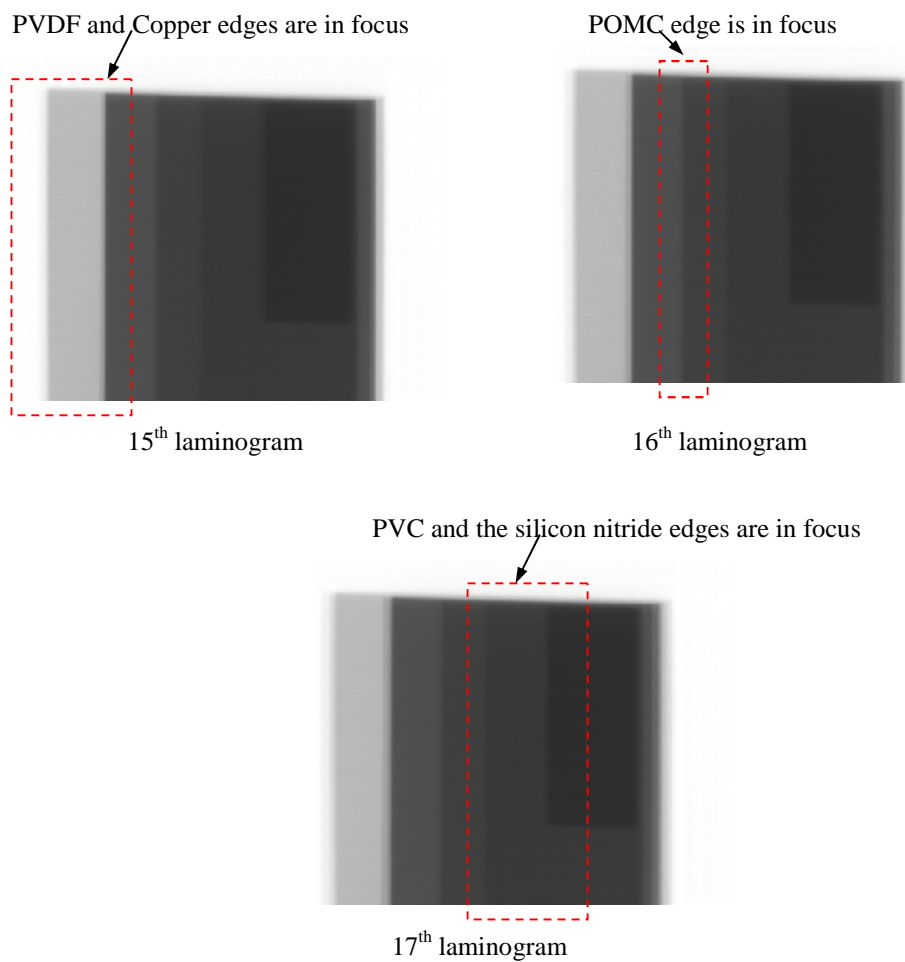
17th laminogram

Fig. 5.11. Laminograms of the 5-layer structure.

(d) Experiment 4: Experiment on mass density calculation

The accuracy of mass density calculation is limited by the error band associated with the thickness estimation. Therefore, the calculation results inherently have an error band. In this work, the maximum and the minimum mass density are computed to define the error boundary. This experiment involves scanning PMMA and AL stepwedges. The empirical result is tabulated in *Table 5-1*.

	Surface density ρ (g/cm^2)	Mass density ρ (g/cm^3)	Average estimated thickness T_E (cm)	Max. mass density ρ_{max} (g/cm^3)	Accuracy of ρ_{max}	Min. mass density ρ_{min} (g/cm^3)	Accuracy of ρ_{min}
PMMA (1.10 cm)	1.27	1.19	1.00	2.54	-13%	0.85	71%
AL (1.20 cm)	3.14	2.70	1.00	6.28	-32%	2.09	77%
PMMA (4.40 cm)	5.24	1.19	4.00	1.50	74%	1.16	97%
AL (6.00 cm)	15.90	2.70	5.00	3.53	69%	2.89	92.%
PMMA (14.30 cm)	17.80	1.19	14.00	1.32	89%	1.23	96%
AL (14.40 cm)	39.20	2.70	15.00	2.70	99%	2.53	93%

Table 5-1 Estimation of mass density for different thickness and materials.

5.2.3 Summary

Laminograms can be produced by employing a digital laminography technique with the multiple-view X-ray image sequence. It requires good quality image data and proper multiple-view image geometry. The laminograms make it possible to estimate the thickness from 2-D imaging by counting the number of layers occupied by the target objects. However, selecting feature of the objects is not trivial. Poor quality features can lead to significant errors. Hence, the proper training must be given in order to improve the accuracy of the thickness estimation. Once the thickness can be well estimated, the mass density can be extracted directly with good accuracy.

The estimation of thickness still can be poor or failure due to the error band or minimum depth increment between two adjacent layers. If the object is much thinner than the minimum depth increment between two adjacent layers, all features on the

object will focus in same laminogram. Thus, it is unable to perform estimation of thickness. To minimise the depth increment between two adjacent layers, larger view angle and smaller sample size of scanning are required. For example, the minimum depth increment between two adjacent layers can be successfully reduced to 0.1 cm if the sample size is reduced to 0.004 cm and view angle separation is expanded to 5°. The estimation results will be poor due to the error band if the thickness of object is similar to the minimum depth increment between two adjacent layers. Generally, the error band is ±50% of the minimum depth increment between two adjacent layers. Therefore, minimising the minimum depth increment can also reduce the error band and improve the quality of thickness estimation. In this experiment, the error band is ±0.5 cm which makes the estimation results invalid for the object thickness less than 4.4 cm. The estimation for the thick objects performs better than the thin objects due to signal to noise ratio which is illustrated in *Table 5-1*.

5.3 Colour Encoding Discriminated Material Information

A new colour scheme is developed for colour coding the discriminated material information. This new colour scheme is built on the industry standard colour scheme and employs red colour to highlight the potential threat information (i.e. TNT). In total, four colours appear in the new colour scheme which are red for the threat information, orange for harmless organic materials, green for mixture materials, and blue for metal materials, respectively. Under the new colour scheme, the X-ray images are colourised according to effective atomic number, ratio of input to output intensity which is mainly affected by mass density, and thickness information computed by employing the K-II technique, W-E technique, and thickness estimation method.

5.3.1 Discrimination of material information

In order to obtain the material parameters from the raw X-ray images, six major processes are required as illustrated in *Fig. 5.12*. They are image normalisation process, multiple-view image generation process, image segmentation process, the K-II technique computation process, the W-E technique extraction process, and thickness

estimation process. Initially an image normalisation process obtains line-scan X-ray images from hundreds of raw dual-energy X-ray images and refines the images by minimising heel effect, temporal noise, and spatial noise. The refined line-scan X-ray images are then reconstructed to produce a sequence of multiple-view X-ray images. Laminograms are also produced for image segmentation and thickness estimation. The K-II technique is processed to compute the effective atomic number and surface density. The overlapping regions can be determined by image segmentation. Applying W-E technique to the overlapping regions, material effective atomic number and surface density can be extracted. Combining the computed effective atomic number and surface density with the thickness estimated (by employ laminography) enables the material parameters to be obtained.

```
                          ┌─────────────────┐
                          │      START      │
                          └────────┬────────┘
                                   │
          ┌────────────────────────┤
          │                        │
          ▼                        ▼
┌──────────────────┐    ┌──────────────────┐
│ Image            │    │ Multiple-view    │
│ normalisation:   │───▶│ X-ray image      │
│ producing refined│    │ generation:      │
│ line-scan X-ray  │    │ producing a      │
│ image            │    │ sequence of      │
└────────┬─────────┘    │ multiple-view    │
         │              │ X-ray images     │
         ▼              └────────┬─────────┘
┌──────────────────┐            │
│ K-II technique:  │            │
│ computing material│           │
│ effective atomic │            ▼
│ number and surface│   ┌──────────────────┐
│ density          │   │ Laminogram:       │
└────────┬─────────┘   │ generating a      │
         │             │ sequence of       │
         ▼             │ laminograms       │
┌──────────────────┐   └────────┬─────────┘
│ Image segmentation:│          │
│ obtaining         │          │
│ overlapped regions│          │
│ in X-ray image    │          ▼
└────────┬─────────┘   ┌──────────────────┐
         │             │ Target region    │
         ▼             │ thickness:        │
┌──────────────────┐   │ estimating the    │
│ W-E technique:   │   │ thickness of a    │
│ extracting effective│ │ target region    │
│ atomic number and│──▶│ and computing     │
│ surface density from│ │ its mass density │
│ the overlapping  │   └────────┬─────────┘
│ regions and      │            │
│ determining the  │            │
│ target region    │            │
└──────────────────┘            │
                                ▼
                       ┌─────────────────┐
                       │      END        │
                       └─────────────────┘
```

Fig. 5.12. Major steps for material discrimination.

5.3.2 New colour scheme

The new colour scheme, which is based on the industry standard colour palette, is developed to encode the discriminated material information. It employs the HSI colour space and produces 4 different colours. The X-ray image is colourised according to the computed material effective atomic number and the ratio of output and input intensity (I_o/I), which is an indicator of X-ray attenuation and affected by effective atomic number, mass density and thickness. Generally, the effective atomic number determines the value of hue and the ratio I_o/I provides values of saturation and intensity. *Fig. 5.13* (a), (b), (c), and (d) illustrate the colour maps for the threat materials, organic, mixture, and metal categories respectively. The effect produced according to the colour map is shown in *Fig. 5.14*. The harmless organic materials are highlighted in orange, mixture materials are highlighted in green, and the metal materials are highlighted in blue. The materials, which have atomic number lying between 7 and 9, are highlighted in red colour. The red colour implies potential threat.
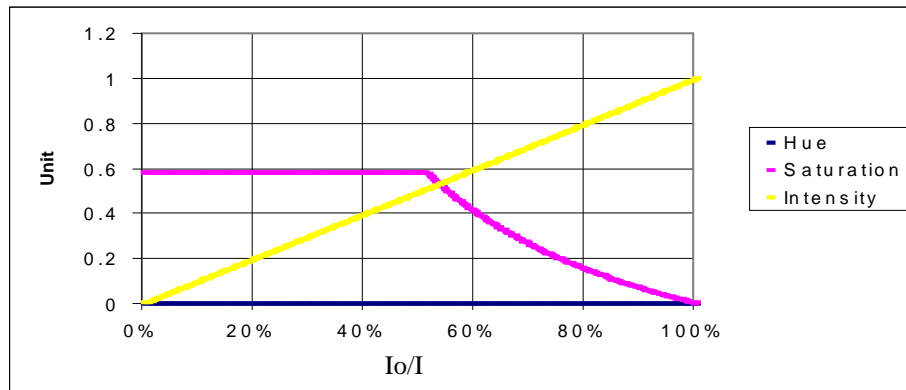
Fig. 5.13 (a). Colour scheme for threat materials.
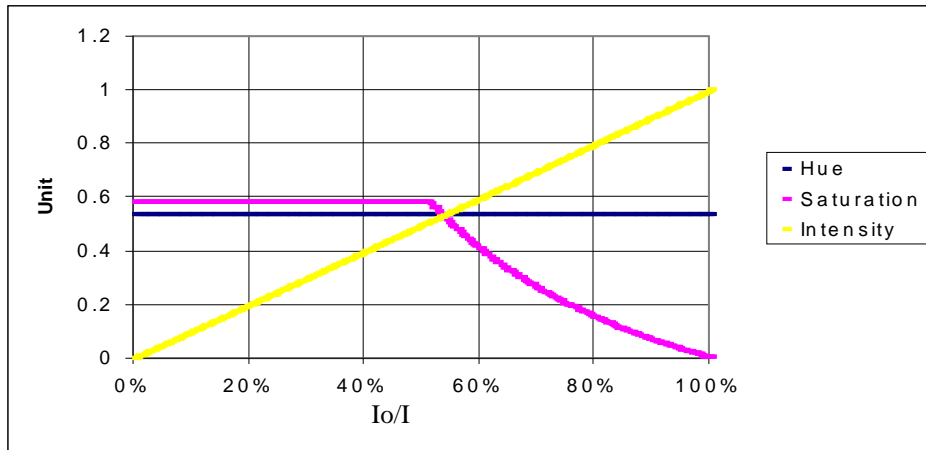
Fig. 5.13 (b). Colour scheme for organic materials.
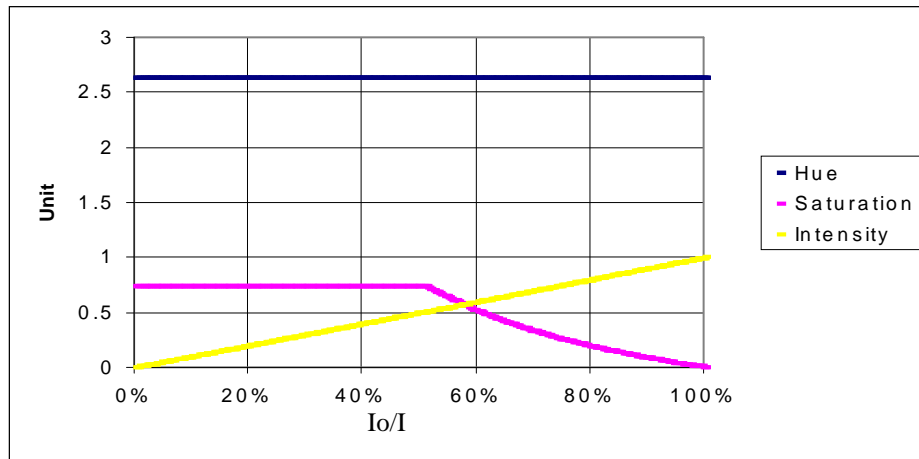
**Fig. 5.13 (c). Colour scheme for mixture materials.**
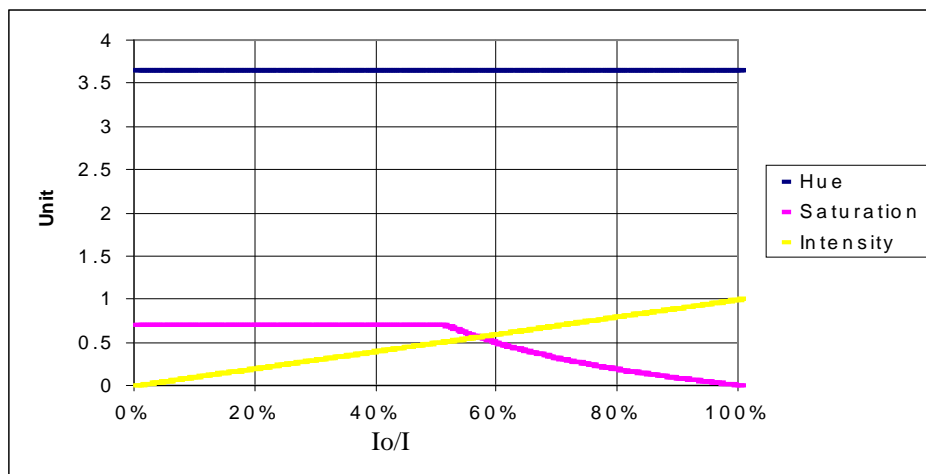
**Fig. 5.13 (d). Colour scheme for metal materials.**
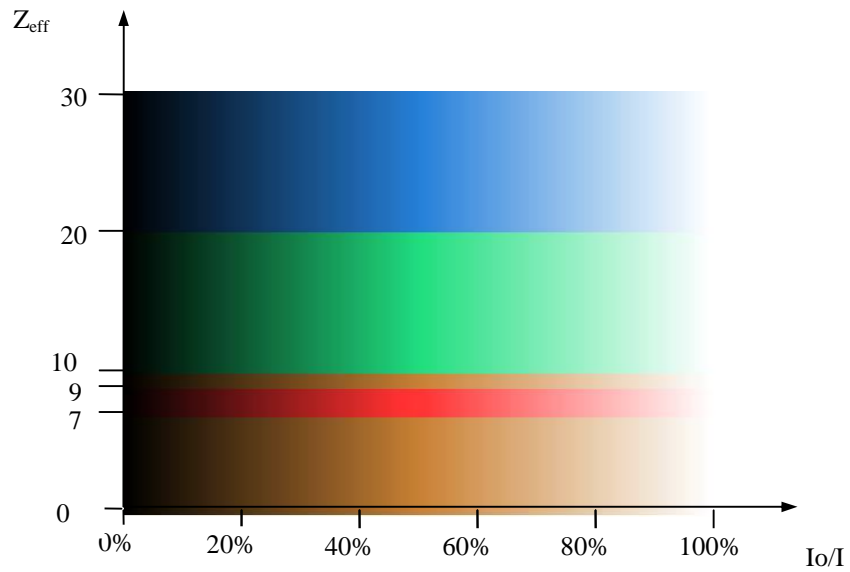
Fig. 5.14 Colour map

5.3.4 Experiments on colour encoding the discriminated material information

Four single layer plates, fabricated from copper, aluminium, *PPOm* and *PVDF*, are scanned to demonstrate the performance of the new colour scheme. The normalised images are shown in *Fig. 5.15*. The calculated material effective atomic number and mass density are shown in *Table 5-2*. The images colourised by utilising the new colour scheme are shown in *Fig. 5.16*.

PPOM (H)　　　　　PPOM (L)

(a)

PVDF (H)　　　　　PVDF (L)

(b)

SN (H)　　　(c)　　　SN L

TITAN (H)　　　(d)　　　TITAN (L)
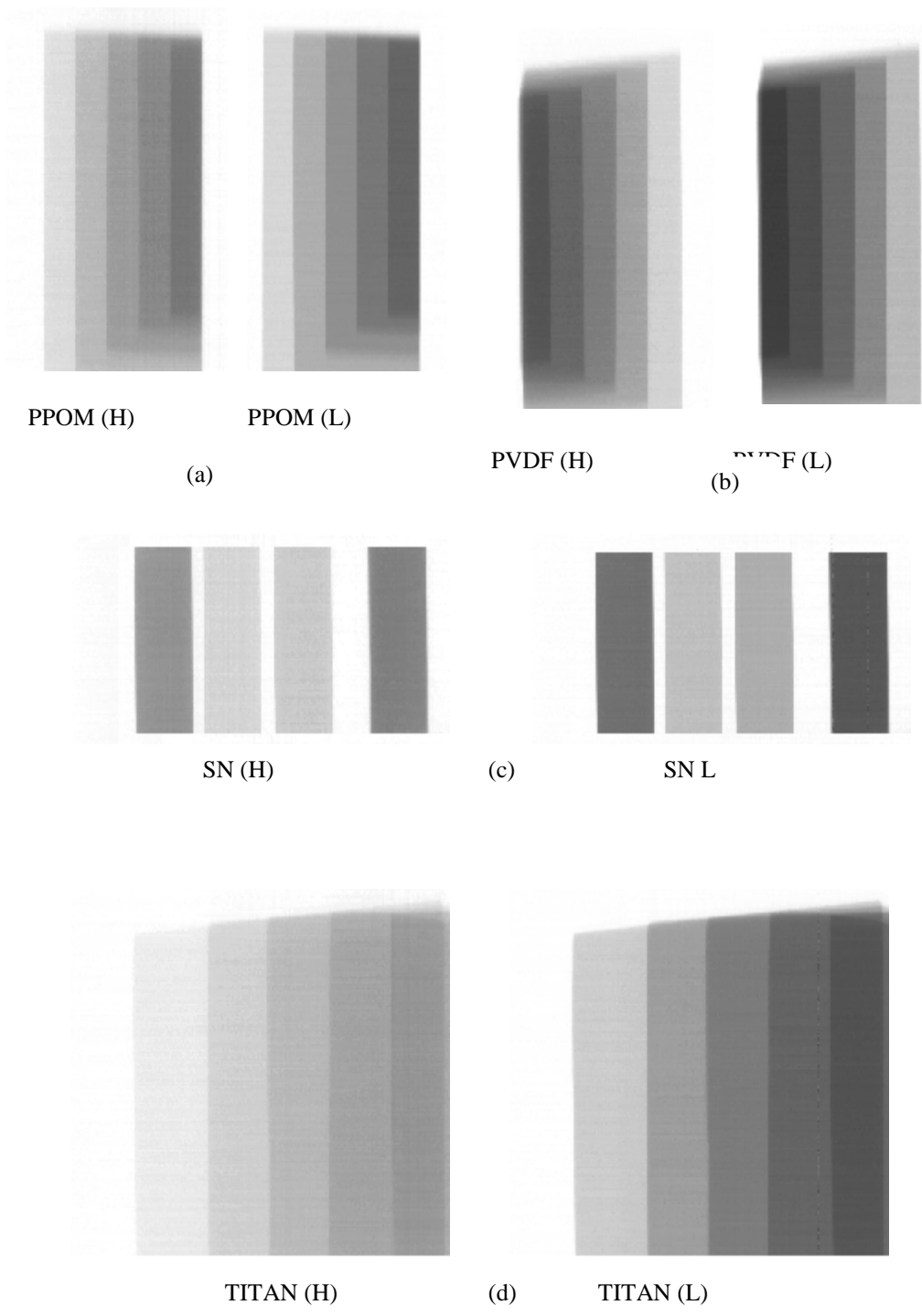
Fig. 5.15 Normalised X-ray images of (a) PPOM plate, (b) PVDF plate, (c) SN plate, and (d) TITAN plate.

	Z	K-Z	$\|\Delta Z\|$	ρ (g/cm^3)	d_E (cm)	ρ_C (g/cm^3)	$\|\Delta\rho\|$ (g/cm^3)
1-layer PPOm	6.10	6.50	0.40	1.06	0.99	1.18	0.12
2-layer PPOm	6.10	6.50	0.40	1.06	1.98	1.18	0.12
3-layer PPOM	6.10	6.50	0.40	1.06	2.97	1.18	0.12
4-layer PPOM	6.10	6.50	0.40	1.06	3.96	1.18	0.12
5-layer PPOM	6.10	6.50	0.40	1.06	4.95	1.18	0.12
1-layer PVDF	7.88	7.50	0.38	1.76	0.99	2.15	0.39
2-layerPVDF	7.88	7.50	0.38	1.76	1.98	2.15	0.39
3-layer PVDF	7.88	7.50	0.38	1.76	2.97	2.15	0.39
4-layer PVDF	7.88	7.50	0.38	1.76	4.95	1.72	0.04
5-layer PVDF	7.88	7.50	0.38	1.76	5.94	1.79	0.03
1-layer cold pressed Silicon Nitride	12.10	13.00	0.90	2.40	n/a	n/a	n/a
3-layer cold pressed Silicon Nitride	12.10	13.00	0.90	2.40	0.99	4.17	1.77
1-layer hot pressed Silicon Nitride	12.10	13.00	0.90	3.11	n/a	n/a	n/a
3-layer hot pressed Silicon Nitride	12.10	13.00	0.90	3.11	0.99	5.13	2.02
1-layer Titanium	22.00	22.00	0.00	4.50	n/a	n/a	n/a
2-layer Titanium	22.00	22.00	0.00	4.50	n/a	n/a	n/a
3-layer Titanium	22.00	22.00	0.00	4.50	n/a	n/a	n/a
4-layer Titanium	22.00	22.00	0.00	4.50	n/a	n/a	n/a
5-layer Titanium	22.00	22.00	0.00	4.50	n/a	n/a	n/a

Table 5-2 The discrimination results for four structures.
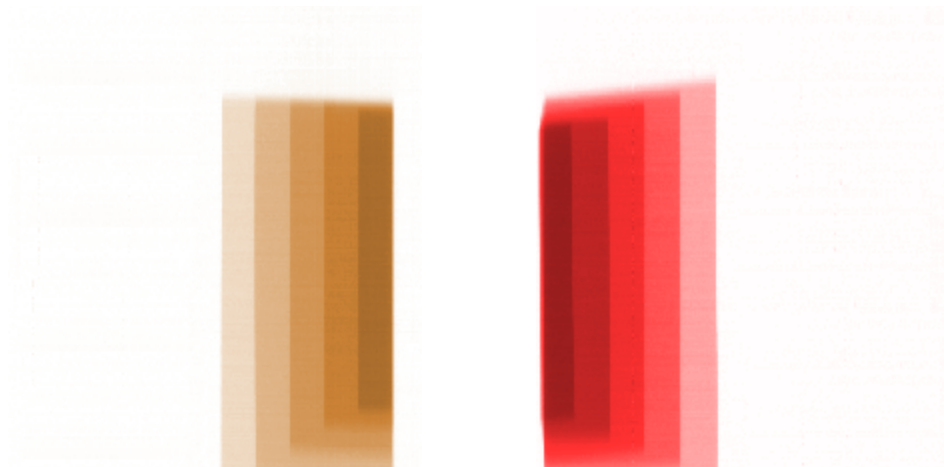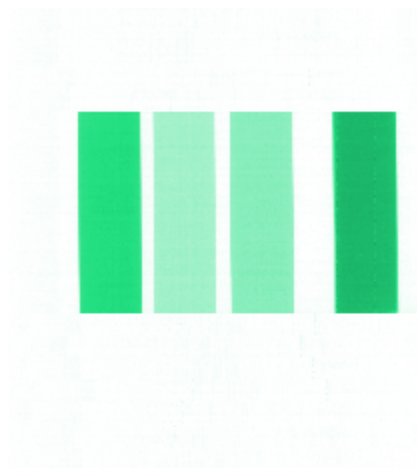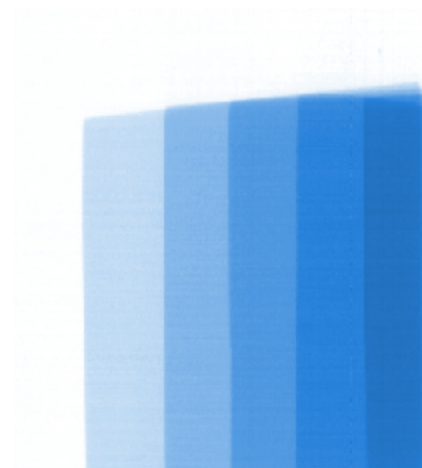
**Fig. 5.16 Colourised X-ray images of (a) PPOM plate, (b) PVDF plate, (c) SN plate, and (d) TITAN plate.**

A five-layer structure is also considered in this experiment. The normalised dual-energy X-ray images are shown in *Fig. 5.17*. The refined multiple-view X-ray images and laminograms of this structure are shown in *Fig. 5.10* and *Fig. 5.11*. In the segmentation process on edge detecting technique is applied and the detected edges of the structure

are illustrated in *Fig. 5.18 (a) and (b)*. According to the detected edges and the computed material effective atomic number, five regions are segmented and are highlighted in yellow, light blue, purple, green, and dark blue, as illustrated in *Fig. 5.18 (c)*. Observing the laminograms, the structure can be divided into 3 layers. The first layer includes yellow region and light blue region, the second layer is purple region, and the third layer involves green and dark blue regions. The calculated material effective atomic number and mass density is shown in *Table 5-3*. The X-ray image of the 5-layer structure is colourised by employing two colour schemes which are the industry colour 'standard' colour palette and the newly developed colour scheme, respectively. The resultant colourised X-ray images are shown in *Fig. 5.19* and *Fig.5.20*.

5-layer structure (H)   5-layer structure (L)
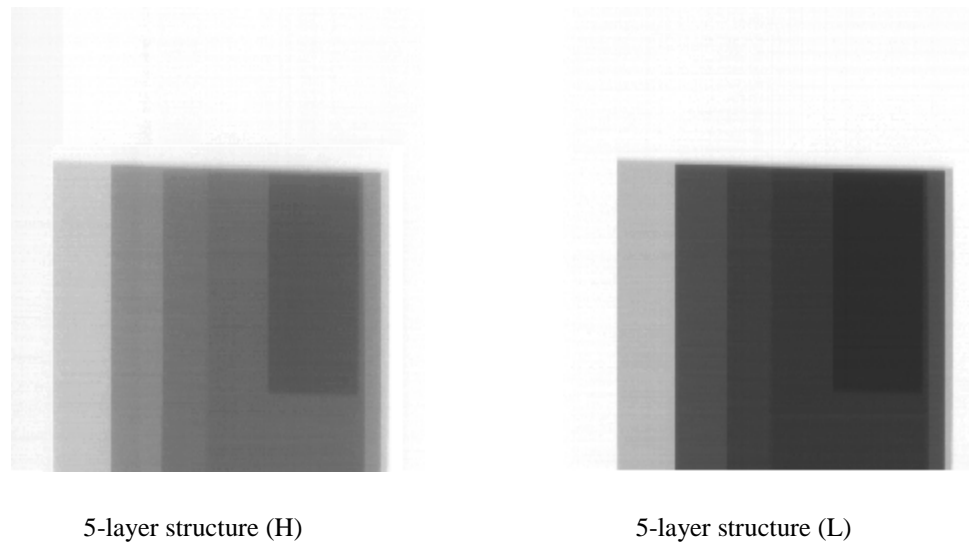
Fig. 5.17 Normalised X-ray images of a 5-layer structure.
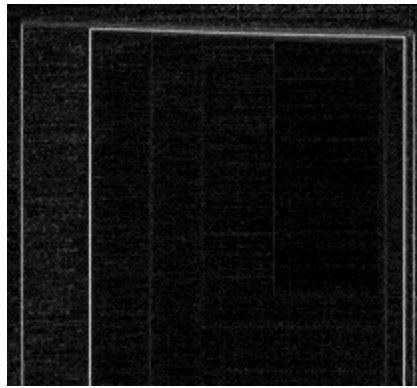
(a)
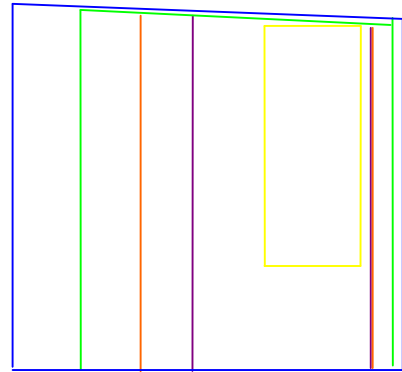
(b)
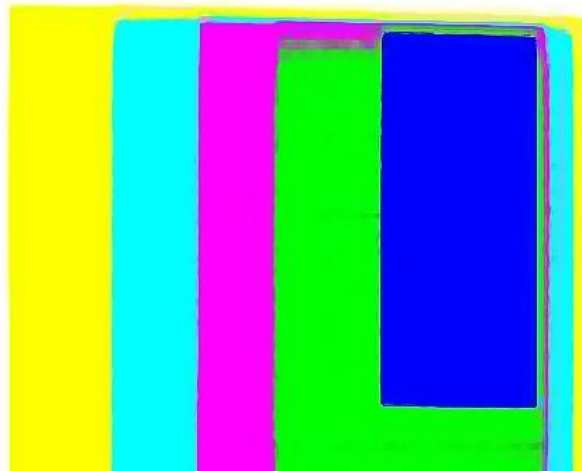
(c)

Fig. 5.18. Segmentation of a 5-layer structure.

	Z	K-Z	$\lvert \Delta Z \rvert$	ρ (g/cm^3)	d_E (cm)	ρ_C (g/cm^3)	$\lvert \Delta\rho \rvert$ (g/cm^3)
Region 1 (PVDF)	7.88	7.50	0.38	1.76	0.99	2.15	0.39
Region 2 (Copper)	29.00	31.00	2.00	0.10	n/a	n/a	n/a
Region 3 (POMC)	6.95	7.00	0.40	1.41	0.99	1.58	0.17
Region 4 (PVC)	13.90	13.50	0.40	0.40	n/a	n/a	n/a
Region 5 (Silicon Nitride)	12.10	13	0.90	0.50	n/a	n/a	n/a

Table 5-3. Discrimination results for the 5-layer structure.
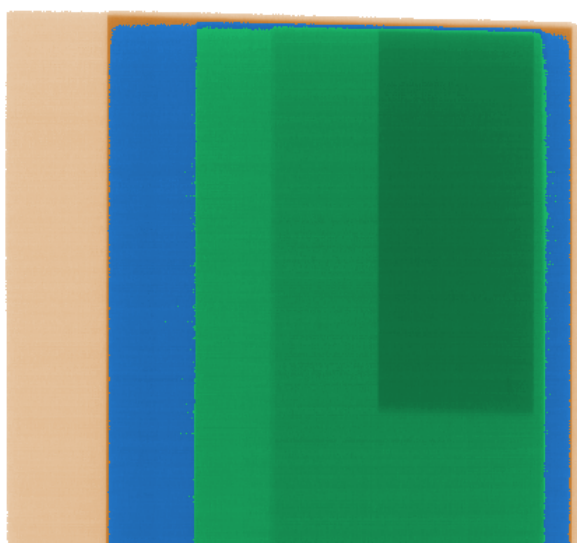
**Fig. 5.19. Conventional colourised X-ray image of a 5-layer structure.**
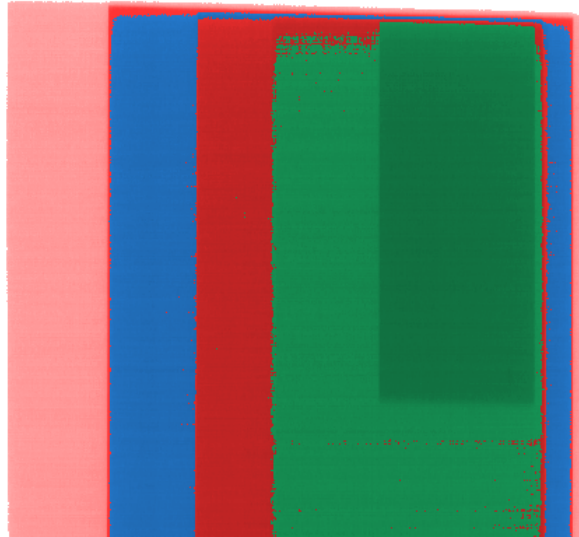
Fig. 5.20. New colour scheme for a 5-layer structure.

A simulated explosive (introduced in Chapter three) is colourised according to the new colour scheme. Four out of a total of twenty views (See Appendix C) are illustrated in *Fig. 5.21*. The effective atomic number of the dense organic material lies between 7 and 9 which falls into the range defined as a target and is highlighted by the additional red colour in the new colour scheme. Colour shifts also occur due to the changing relative interposition of background and foreground objects throughout the sequence (i.e. the blue wire becoming green as it is masked by the organic background).

-9^0 perspective angle

-4^0 perspective angle

0^0 perspective angle

5^0 perspective angle

Y

X
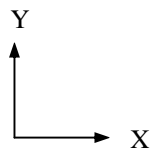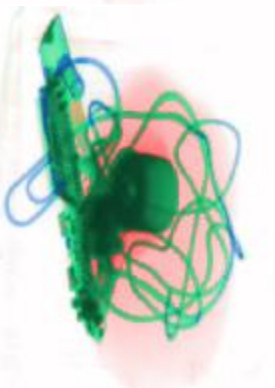
Fig. 5.21: New colour scheme for perspective images produced by the multiple view line-scan X-ray image intensifier system.

5.3.5 Summary

The new colour scheme is developed in reference to the industry 'standard' colour palette. An additional red colour is introduced to separate the potential threat information from the harmless organic materials in X-ray images. This technique enhances the visual impact of potential threat substances. The new colour scheme mainly depends on the material effective atomic number. The significant effect of the new colour scheme is to highlight the potential threat information in a manner can be easily distinguished from other harmless organic materials. Colour encoded images have shown that the new scheme is able to assign the correct colour to either single-layer objects or objects with layers of masking materials. A simulated bomb is colourised according to a 'standard' colour palette and the new colour scheme presented in Chapter Three and Chapter Five, respectively. The sequential parallax information inherent in the colour images is still apparent. The colour shifts are also observed due to the changing relative interposition of background and foreground objects, which is due to the uncompleted segmentation process and inaccurate thickness estimation. These limitations can be partly reduced by improving layer extraction and minimising the minimum depth increment. The dense organic material is highlighted in red in *Fig 5.21* (instead of orange in *Fig. 3.15*) which affords an improved way in which to distinguish the dense organic materials. Mass density has not been treated as an independent parameter in the new colour palette due to the limited thickness estimation performance. The minimum depth increment is large (0.99 cm) in this experiment.

CHAPTER 6: SUMMARY, CONCLUSION AND FUTURE WORK

6.1 Summary

The work reported is part of an ongoing investigation into the scientific and technological basis for a novel materials discriminating 3D X-ray imaging technique. As such, this thesis builds on two major components of prior research conducted by the university team. These are the development of a kinetic depth X-ray imaging (KDEX) technique and a basis materials subtraction (BMS) technique. However, the majority of the investigation concentrates on the adaptation of existing X-ray materials discrimination techniques to accommodate the novel X-ray imaging geometry employed by the KDEX technique. The resultant integration of techniques is empirically evaluated and assessed in terms of its likely utility for security X-ray screening of luggage at airport checkpoints. All original research reported in this thesis is supported by citation and appropriate discussion of contributing research work conducted by those other than the author.

This research programme was primarily instigated to investigate and develop a materials discrimination technique to enhance the visual impact of potential threat information in X-ray images of luggage. The conventional standard dual-energy X-ray discrimination technique, which employs the materials discrimination curves, enables colour coding the resultant X-ray images in terms of organic, mixture and metal groups into orange, green, and blue respectively. However, this crude materials discrimination technique may only be employed as a general indicator of materials and is by no means a precise discrimination. As a result, the 'standard' dual-energy X-ray discrimination technique places plastic explosive in the same, organic window as other harmless organic materials (i.e. paper, soap, plastic etc). The BMS technique previously developed by the university team is restricted to a limited range of materials in which effective atomic number falls between 6.6 and 13. Thus, for instance a mask, which has

an effective atomic number out of the range, would produce a false negative result. This research introduces a solution to such limitations the problems by investigating and developing the K-II technique, the W-E technique, the thickness estimation technique, and a new colour scheme, as described in the following paragraphs.

6.1.1 System calibration and standard colour encoded multiple-view X-ray image sequence

In order to simulate a dual-energy spectrum that approximates the two energy windows commonly utilised in commercially available security scanners a polychromatic X-ray source was appropriately filtered. A multiple slit collimator was constructed to reduce the build up factor and to satisfy the KDEX image collection geometry requirements. The angle of each perspective image, which comprises a complete image sequence, is taken over a range of -8° to $+8^{o}$. Initial work concentrated on developing a normalisation program to reduce the effects of X-ray heel effect, spatial and temporal noise in the resultant X-ray images. The experimental X-ray system's noise and repeatability were examined to evaluate the performance of the normalisation program. Generally, the results are acceptable for broad materials discrimination. The normalised X-ray images enable the calibration of the experimental X-ray machine for organic, mixture and metal discrimination capability. However, the accuracy of the K-II technique and the W-E technique to discriminate target materials was much affected, since it is highly sensitive to the system noise and system repeatability.

6.1.2 Computation of materials' effective atomic number and surface density

The K-II technique is derived from the ρZ projection technique and it obtains the effective atomic number and surface density from computing the intensity of dual-energy X-ray images. The ρZ projection technique was investigated by B. J. Heismann and applied to medical CT imaging for tissue, bone, and blood characterisation. However, the ρZ projection technique was designed for use with 'slice' images. Hence the author adopted the ρZ projection technique to form the K-II technique to enable KDEX imaging to be employed to compute the effective atomic number and mass density for relatively 'thick' objects under non-overlapping conditions. Five step wedges, each fabricated from plastic, Teflon, aluminium, and steel respectively, were

manufactured to calibrate the K-II technique. The calibration data generated are then fitted by a 3rd order polynomial least square fitting Levenberg-Marquardt algorithm. A series of empirical works was conducted to assess the influence of the material categories, thickness, and X-ray inspection angle on the reliability and precision of the K-II technique in discrimination. The conventional method to calculate the effective atomic number of a compound is based on the electron fraction of the individual element. This method is adopted to allow the computation of effective atomic number of an overlapped structure that consists of several compounds. A new method, namely the W-E technique, is devised in this research programme to calculate the weight fraction of the overlapped regions in the resultant X-ray image, instead of the electron fraction. Mathematical derivations are provided in Chapter Four to establish the validity of the technique. The W-E technique enables extracting the targets' effective atomic number and surface density from the masks in the layered structure. The prerequisite of the W-E technique is the application of an edge detector to segment the image into a number of overlapping regions. The author also establishes a series of experiments employing the K-II technique and the W-E technique with KDEX imaging to demonstrate the compatibility of those techniques.

6.1.3 Extraction of material thickness and development of a new colour coding scheme

A thickness estimation technique is reported in terms of mass density extraction. It employs the laminography technique to establish the approximate thickness of object features. Thickness is estimated by interrogating a sequence of laminograms produced by focusing on successive planes of depth, which subtend the object of interest. The accuracy of this information is a function of the sequential parallax exhibited by the image sequence. This in turn is a function of the full range of X-ray beam angles employed by the perspective views and the spatial resolution in the motion axis. In the experimental machine employed in this research the relatively small angular range produces a minimum resolvable thickness or depth increment of 0.99 cm and is a limiting factor in the computation of the mass density. A new colour scheme is developed to highlight the threat information according to the computation of the effective atomic number by the K-II technique and the W-E technique. In addition to the

standard colour palette, red colour is introduced to highlight a new threat window in materials space.

The accuracy in determining the materials' effective atomic number and mass density values of a target material is significantly affected by the following factors:

- unstable X-ray source output and non-uniform detector response, which impact upon the system noise and the system repeatability;

- inaccuracy in the polynomial curve fitting for the dual energy X-ray spectrum;

- limited segmentation of layered image structure;

- error propagation from the K-II technique to W-E technique for target extraction from the masks and;

- the minimum resolvable thickness or depth increment (0.99 cm), which limit the accuracy of thickness estimation.

Theoretically, both techniques are capable of discriminating materials over the same atomic range. However, no experiments have been designed in this research since these materials do not 'usually' appear in luggage encountered at airport checkpoints. A materials' effective atomic number and mass density can be employed as the basis for materials discrimination but this information is not enough for a material identification. To identify the material, atomic composition and crystal structure are required. Thus, the author suggests the use of coherently scattered or diffracted X-rays to provide the additional information. This is a nontrivial suggestion and represents substantial future work.

It is vital to acknowledge that there is no single technique that can be utilised to automatically search for target items concealed in passenger baggage. It is the strong belief of the author that the human operator will be an intrinsic part of the threat detection and identification process especially in the evaluation of shape and spatial

composition. In this research, selecting the focused points from laminograms was carried out manually and it directly influences the computation results of mass density.

6.2 Conclusion

The conclusions drawn from this research are organised in the following paragraphs.

System calibration and standard colour encoded multiple-view X-ray image generation

The heel effect, the spatial noise, and temporal noise have been compensated for via the normalisation process. The maximum noise recorded for the 8-bit greyscale imaging system has a standard deviation less than 0.2 and the system repeatability of the grey level images indicates an average standard deviation of the order of 2.5.

Computation of materials' effective atomic number and surface density

- Within the atomic number range of 6 to 30, the K-II technique has generated a promising overall accuracy of effective atomic number and surface density of 97.30% and 95.08% respectively.

- Factors such as material category, object thickness, and X-ray inspection angle have a marginal effect on the performance of the K-II technique.

- The K-II technique is capable of discriminating between materials which have the same atomic number but different mass density (e.g. Silicon Nitride: hot pressed and cold pressed).

- The performance of the W-E technique for the extraction of a target from masking materials is limited by the segmentation produced by a standard edge detection operator.

- The accuracy of W-E technique in the extraction of the targets' effective atomic number and surface density are 96.53% and 92.35% respectively.

- The W-E technique has demonstrated a robust capability in dealing with a multi-layered structure, up to 4 layers of different combination of organic, mixture, or metal material masks.

Extraction of thickness and development of a new colour coding scheme

- Laminographic data may be employed to estimate object thickness, which then allows the determination of the mass density of the object under inspection.

- Empirical data has demonstrated that the accuracy of the mass density computation is profoundly limited by the minimum resolvable depth increment associated with the laminographic data. The error associated with the surface density produced by K-II technique is regarded as insignificant since the overall accuracy is greater than 90%.

- As evidenced in the tabulated results reported in Section 5.2.3 in Chapter Five, the computation of mass density achieved relatively high accuracy for object thickness greater than 4cm. This is demonstrated for two different types of material.

- However, as expected, when the thickness of the object is identical to the minimum resolvable depth increment (e.g., the first experimental sample), or falls within its error band, the accuracy dropped very significantly and may produce highly spacious data.

- The solution to the degradation in accuracy is to reduce the minimum resolvable depth increment. Hence, it is justifiable to conclude that the proposal to compute mass density using surface density information looks to be a promising approach.

In conclusion, the K-II technique and the W-E technique have successfully worked in tandem to reliably compute materials' effective atomic number which falls into the range from 6 to 30. This is true for both non-overlapping and overlapping structures. It has been proven that the object mass density can be estimated by using the

laminography method. As a result, the joint information of effective atomic number and mass density can serve to distinguish a threat from many harmless organic materials. The principal delivery of the research programme is the demonstration of scientific premises of an innovative materials discrimination algorithm that has substantial potential in aviation luggage security screening. However, the minimum resolvable depth increment in this research still remains large (0.99cm). The thickness of the sheet plastic explosive is in the region of 0.3cm to 0.5cm. In this case, the mass density of the sheet plastic explosive cannot be computed.

6.3 Future work

The approach developed in this research is still in its infancy. A number of interdependent areas require further development work to improve the materials discrimination techniques presented in this research. The future work is proposed as follows.

6.3.1 Obtaining thickness information from 'slice' images by employing the X-ray tomosythesis

Employing a laminography technique to estimate thickness, implies an error band, which is up to the length of a 'voxel', which can produce unstable mass density for very thin objects. The X-ray tomosynthesis [136][137][138] technique, which is also referred to as limited angle CT, is widely utilised for medical applications (such as breast cancer scanning), can produce 'slice' images which would improve thickness estimation and the error band in comparision with laminography. Unlike conventional CT techniques, X-ray tomosynthesis requires only a few seconds to produce a 'slice' image and it employs a $\sim 100^{o}$ inspection range. The less restrictive requirements of this inspection angle make the X-ray tomosynthesis technique potentially useful for aviation security screening. This accuracy of thickness computation might be significantly increased and thin objects could also be extracted. The refined thickness information also produces good accuracy for mass density computation. The 'slice' image is also helpful with the segmentation of overlapping regions thus providing a basis for 3D image reconstruction.

6.3.2 Three-dimensional (3D) image reconstruction

Within the limited range of perspective angles employed in KDEX imaging, multiple-view X-ray scanners offering the display of images does not need to be restricted to the conventional axial images. Instead, it is possible to employ an X-ray tomosynthesis technique to construct a volumetric image by 'stacking' the individual slices one on top of the other. The imaging may be displayed in an alternative manner. Reconstruction techniques, such as multiplanar reconstruction and 3D rendering [139] techniques, are generally employed. Multiplanar [140][141][142] reconstruction is one of the simplest methods of reconstruction. A volume can be cut into slices through a different plane (usually orthogonal). Optionally, a special projection method, such as maximum-intensity projection or minimum-intensity projection, can be used to build the reconstructed slices. Multi-planar reconstruction is frequently used for medical examination (i.e. the spine and the brain). A threshold value of intensity is chosen or set by the operator and the edge detection image processing algorithms can be utilised. From this, a 3D model can be constructed and displayed and multiple models can be constructed from various different thresholds. Successful 3D image reconstruction will be a great help in image segmentation and materials discrimination, especially in mass density extraction.

6.3.3 X-ray crystallography for material identification

Material effective atomic number and mass density can be employed to categorise materials in materials discrimination. However, they are not enough to identify the materials. Crystal composition and structure, cannot be obtained through analysing transmission X-ray images and are the fundamental requirements for material identification. X-ray crystallography enables determination of the arrangement of atoms within a crystal, in which a beam of X-rays strikes a crystal and scatters into many different directions. X-ray crystallography has been fundamental in the development of many scientific fields. The method also reveals the structure and functioning of many biological molecules, including vitamins, drugs, proteins and nucleic acids such as DNA. After a crystal has been obtained or grown in the laboratory, it is mounted on a goniometer and gradually rotated while being bombarded with X-rays, producing a

diffraction pattern of regularly spaced spots known as reflections. The two-dimensional images taken at different rotations are converted into a three-dimensional model of the density of electrons within the crystal using the mathematical method of Fourier transforms, combined with chemical data known for the sample. The obtained crystal composition and structure enable precise identification of a threat or drugs from X-ray image of luggage. It is conjectured that the appropriate collection and processing of coherently scattered X-rays could be realised using modified KDEX image collection geometry. However, coherently scattered X-rays are orders of magnitude lower in intensity than primary beam X-rays and would require significant research effort to investigate further.

6.3.4 Human factors evaluation to enhance the colour-coding scheme

The success of the colour-coding scheme is dependent upon the visual impact of the colour encoded multiple view X-ray image sequences not confusing the observer and improving the efficiency of explosive or weapon detection and identification. The validity of such work is dependent upon psychological human factors considerations. Experiments incorporating the improved materials discrimination information and new colour scheme are planned to be incorporated into an established funded collaborative research programme with the US DHS.

PUBLICATION

J P O Evans, X Wang, J W Chan and D Downes, "Colour 3D X-Ray Imaging for Security Screening" IET Conference on Crime and Security: Imaging for Crime Detection and Prevention, pp. 372-377, 13-14 June 2006.

REFERENCE

1 Official website of the US Transportation Security Administration (http://www.tsa.gov/311/index.shtm).

2 . J. P. O. Evans, "Stereo imaging using folded linear dual-energy X-ray detectors", IOP J. Meas. Sc. & Tech., 13, pp. 1388-1397, (2002).

3 Wang T.W, "Target materials discrimination using stereoscopic dual-energy X-ray images", 2002, NTU, PhD Thesis.

4 Hon H.W, "The modelling of multiple beam X-ray systems using visible light", 2000, NTU, PhD Thesis.

5 J. P. O. Evans and H. W. Hon, "Dynamic stereoscopic X-ray imaging", J. of NDT&E, 35, pp. 337-345, (2002).

6 J. P. O. Evans, Y. Liu and J. W. Chan, "Depth from motion 3D X-ray imaging for security screening", IEE International symposium on imaging for crime detection and prevention, pp. 5-8, (2005)

7 J. P. O. Evans, Y. Liu, J. W. Chan and D. Downes, "View Synthesis for Depth from Motion 3D X-ray Imaging", Pattern Recognition Letters, accepted for publication (2006).

8 H. Wallach and D. N. O'Connell, "The kinetic depth effect", J. Experimental Psychology, 45, (4), pp. 205-217, (1953).

9 J. J. Gibson, "The Senses Considered as Perceptual Systems", Houghton Mifflin, Boston, (1966).

10 J. P. O. Evans "Kinetic depth effect X-ray (KDEX) imaging for security screening", Visual Information Engineering, 2003. VIE 2003. International Conference on Volume , Issue , 7-9 July 2003 Page(s): 69 – 72.

11 R. F. Eilbert and K. D. Krug, "Aspects of image recognition in Vivid Technology's dual-energy x-ray system for explosives detection", Proceedings of SPIE, vol. 1824, pp.127-143, (1992).

12 A. Macovski, R. E. Alverez, J. L. Chan, J. P. Stonestrom and L. M. Zata, "Energy Dependent Reconstruction in X-ray Computerized Tomography", Computers in Biology and Medicine, vol. 6, pp. 325-336, (1976).

13 ALVAREZ R.E., MACOVSKI A., 'Energy-selective reconstructions in X-ray computerized tomography', Phys. Med. Biol., Vol. 21, No. 5, pp. 733-744, 1976.

14 LEHMANN L.A., ALVAREZ R.E., MACOVSKI A., BRODY W.R., 'Generalized image combinations in dual KVP digital radiography', *Med. Phys.*, Vol. 8, No. 5, pp. 659-667, Sept./Oct. 1981.

15 B. J. Heismann, J. Leppert, and K. Stierstorfer, "Density and atomic number measurements with spectral x-ray attenuation method", Journal of applied physics, volume 94, number 3, 1 August 2003.

16 Evans J. P. O. and Hon H. W., "Multiple-view stereoscopic line-scan imaging", in Proceedings of SPIE Vol. 4660, pp. 320-324, 2001.

17 Evans, J. P. O., Hon H. W. and Chan J. W., "Motion–induced depth effect using a multiple view dual-energy X-ray camera", in Proceedings of SPIE Vol. 4786, pp. 65-71, 2002.

18 Evans J. P. O., "Kinetic depth effect x-ray (KDEX) imaging for security screening", in IEE Proceedings Vision Image Processing 2003, International Conference on Visual Information Engineering: Ideas, Applications and Experience, pp. 69-72, July 2003.

19 Chan J.W, 'Investigation into an integrated stereoscopic dual-energy X-ray camera', 2004, NTU, PhD Thesis.

20 A. S. Sobania, 'The Automatic Extraction of 3D Information from Stereoscopic Dual-Energy X-ray Images', 2003, NUT, PhD Thesis.

21 Sobania A, Evans J P O, Corner detection from segments using mathematical morphology, Pattern Recognition, Journal of the Pattern Recognition Society, Pattern Recognition Volume 38, Issue 7, July 2005, Pages 1087-1098.

22 Sobania A., "The automatic extraction of 3D information from stereoscopic dual-energy x-ray images", Ph.D. Thesis, The Nottingham Trent University, February 2003.

23 Sobania A., Evans J. P. O, Robinson M., "Object recognition using stereoscopic dual-energy x-ray images", in Proceedings of IEE PREP 2001 Third Conference, pp. 117-118, April 2001.

24 Yong Y. S., Evans J. P. O. and Robinson M., "Automatic extraction of 3D information from binocular stereoscopic x-ray images", in Proceedings of IEE PREP 2001 Third Conference, pp. 137-138, April 2001.

25 Yong Y. S., Evans J. P. O. and Robinson M., "Threat image projection for stereoscopic x-ray imaging", in Proceedings of The IASTED International Conference, Visualization, Imaging and Image Processing, VIIP, pp. 301-306, September 2001.

26 Yong Y. S., "Threat image projection for stereoscopic x-ray screening systems", Ph.D. Thesis, Nottingham Trent University, September 2003.

27 Liu Y, 'View synthesis for depth from motion 3D X-ray imaging', Ph.D. Thesis, Nottingham Trent University, September 2008.

28 Wang T. W. and Evans J. P. O., "Stereoscopic dual-energy x-ray imaging for target materials identification", in IEE Proceedings Vision Image Processing, Vol. 150, No. 2, pp. 122-130, April 2003.

29 J P O Evans, X Wang, J W Chan and D Downes, "Colour 3d X-Ray Imaging for Security Screening" IET. The Crime and Security Conference pp. 372-377, 13-14 June 2006.

30 EVANS J.P.O., 'Development of a 3-D X-ray system', The Nottingham Trent University, PhD Thesis, 1993.

31 EVANS J.P.O., ROBINSON M., 'A binocular stereoscopic X-ray imaging technique using folded array linear X-ray detectors', Institute of Physics: Journal of Measurement Science and Technology, No. 13, pp. 1388-1397, July 2002.

32 R. C. Murty, "Effective atomic numbers of heterogeneous materials", Nature 207, 398-399 (24 July 1965).

33 A. Michette, S. Pfauntsch, "X-rays - The First Hundred Years", pp. 256, Wiley, ISBN 0-471-96502-2, March 1997.

34 A. G. Michette, C. J. Buckley, "X-rays Science and Technology", Institute of Physics Publishing, ISBN 0-7503-0233X, 1993.

35 Sample, Sharron,. "X-Rays". The Electromagnetic Spectrum. NASA. 2007.

36 G. F. Knoll, "Radiation Detection and Measurement", second edition, John Wiley & Sons Ltd., ISBN 0471815047, pg. 50-55, 1989.

37 J.H. Hubbell, "Photon Cross Sections, Attenuation Coefficients, and Energy Absorption Coefficients From 10eV and 100GeV, Report No: NSRDS-NBS 29", Washington: U.S.G.P.O, 1969.

38 J.H. Hubbell, S.M. Seltzer "Table of X-rays Mass Attenuation Coefficients and Mass Energy Photon Coefficients 1keV to 20 MeV for Elements Z=1 to 92 and 48 Additional Substances of Dosimetric Interest. NISTIR 5632", U.S. Department of Commerce, May 1995.

39 J.H. Hubbell "Radiation Physics, Encyclopaedia of Physical Science and Technology", third edition, vol. 13, Academic Press, 2002

40 T. S. Curry. Ш, J. E. Dowdey, R. C. Murray, "Christensen's Introduction to the Physics of Diagnostic Radiology", third edition, Lea & Febiger, ISBN 081210918X, Chapter 5, 1984.

41 National Research Council, U.S. Committee on Commercial Aviation Security, "Detection of explosives for commercial aviation security. Committee on Commercial Aviation Security, National Materials Advisory Board, Commission on Engineering and Technical Systems, National Research Council", Washington, D.C. National Academy Press, ISBN 0309049458, 1993.

42 RUTHERFORD R.A., PULLAN B.R., ISHERWOOD I., 'Measurement of Effective Atomic Number and Electron Density Using an EMI Scanner', Neuroradiology, Vol. 11, pp. 15-21, 1976.

43 COENEN J.G.C., MAAS J.G., 'Material classification by dual-energy computerized X-ray tomography', International Symposium on Computerized Tomography for Industrial Applications, pp. 120-127, June 1994.

44 CHUANG K.S., HUANG H.K., 'Comparison of four dual energy image decomposition methods', Phys. Med. Biol., Vol. 33, No. 4, pp. 455-466, 1988.

45 GUY M.J., CASTELLANO-SMITH I.A., FLOWER M.A., FLUX G.D., OTT R.J., VISVIKIS D., 'DETECT-dual energy transmission estimation CT-for improved attenuation correction in SPECT and PET', IEEE Transactions on Nuclear Science, Vol. 45, No. 3, pp. 1261-1267, June 1998.

46 WILLI A. KALENDER, ERNST KLOTZ, LENA KOSTARIDOU, 'An Algorithm for Noise Suppression in Dual Energy CT Material Density Images', IEEE Transactions on Medical Imaging, Vol. 7, No. 3, pp. 218-224, Sept. 1988.

47 WOJCIK R., MAJEWSKI S., PARKER F.R., WINFREE W.P., 'Single shot dual energy reverse geometry X-radiography (RGX)', IEEE Nuclear Science Symposium, Vol. 2, pp. 811-815, 1996.

48 HOBBIE R.K., 'Interaction of photons and charged particles with matter', Nuclear Medical Physics, Vol. 1, pp. 65-141, 1987.

49 YAN C.H., WHALEN R.T., BEAUPRE G.S., YEN S.Y., NAPEL S., 'Reconstruction algorithm for polychromatic CT imaging: application to beam hardening correction', IEEE Transactions on Medical Imaging, Vol. 19, No. 1, pp. 1-11, Jan. 2000.

50 Guowei Zhang; Li Zhang; Zhiqiang Chen, 'An H-L curve method for materials discrimination of dual energy X-ray inspection systems', Nuclear Science Symposium Conference Record, 2005 IEEE Volume 1, Issue , 23-29 Oct. 2005 Page(s):326 - 328

51 V.L. Novikov, S.A. Ogorodnikov, V.I. Petrunin, "Dual energy method of material recognition in high

energy introscopy systems", Proc. 16th International Workshop on charged particle linear accelerators, 1999, Alushta, Crimea, Ukraine, appeared in ISSN 1562-6016, Problems of atomic science and technology, 1999,v.4, 93.

52 S.A. Ogorodnikov, V.I. Petrunin, "Processing of interlaced images in 4-10MeV dual energy customs system for material recognition", Proceedings of the 6th International Computational Accelerator Physics Conference, 2000, Darmstadt, Germany.

53 WANG T.W., EVANS J.PO., 'Dual-energy X-ray Imaging for the Extraction of Effective Atomic Number from Overlapping Materials', IEE Proceedings – Vision, Image and Signal Processing, submitted Dec 2001 (accepted for publication).

54 WANG T.W., EVANS J.P.O., 'The Application of Stereoscopic Dual-energy X-ray System for Target Materials Identification', IEE Proceedings – Vision, Image and Signal Processing, submitted Dec 2001 (accepted for publication pending minor revision).

55 WILLIAM H.P., SAUL A.T., WILLIAM T.V., BRIAN P.F., 'Numerical Recipes in C – The Art of Scientific Computing', 2nd Edition, Cambridge University Press, 1995.

56 B.J. Heismann, 'Signal to noise behavior of bone and water material decomposition' and 'Noise transfer analysis of Base material decomposition in dual energy CT', submitted to IEE MIC (2006).

57 CHRISTENSEN E.E., CURRY T.S., NUNNALLY J., 'An Introduction to the Physics of Diagnostic Radiology', Lea and Feibiger - Philadelphia,   pp. 196-223, 1972.

58 DAVSON H., 'Davson's Physiology of the Eye, 5th Edition', Macmillan Press London, pp. 449-485, 1990.

59 HARALICK R.M., SHAPIRO L.G., 'Glossary of computer vision terms', Pattern Recognition, Vol. 24, No. 1, pp. 69-93, 1991.

60 KANG S.B., WEBB J.A., ZITNICK C.L., KANADE T., 'A multibaseline stereo system with active illumination and real-time image acquisition', Proceeding 5th International Conference on Computer Vision, pp. 88-93, USA, June 1995.

61 SPOTTISWOODE R., SPOTTISWOODE N.L., SMITH C., 'Basic principles of the three-dimensional film', Journal of the SMPTE, pp. 249-286,   Oct. 1952.

62 TYCHSEN L., 'Adler's Physiology of the Eye, 9th Edition', Mosby-Year Book Inc., pp. 773-853, 1992.

63 VALYUS N.A., 'Stereoscopy', The Focal Press, 1966.

64 OKOSHI T., 'Three-dimensional Imaging Techniques', Academic Press,   pp. 49-59, 1976.

65 PONG T.C., KENNER M.A., OTIS J., 'Stereo/motion cues in pre-attentive vision processing: some experiments with random dot stereographic image sequences', IEEE Proceeding of the workshop on visual motion, pp. 314-320, March 1989.

66 Hon H.W, Evans J.P.O, "Multiple view line-scan imaging", 2002, IEE Proc. Optoelectronics, 149, 2, 45-50.

67 X-TEK Systems Limited, 64-66 Akeman Street, Tring, Herts. HP23 6AF, United Kingdom.

Website : http://www.xtek.co.uk/systems.htm.

68 Euclid Seeram, "Digital Radiography: An Introduction for Technologists," Delmar Cengage Learning, 1st edition, 2008.

69 J.G. Kereiakes, C.G. Orton, S.R. Thomas, 'Digital Radiography', Springer; 1st edition, 1986.

70 R. D. Speller and G. J. Ensell, "A System for Dual-energy Radiography," The British Journal of Radiology 56, pg. 461-465, 1983.

71 H. N. Cardinal and A. Fenster, "An Accurate Method for Direct Dual-energy Energy Calibration and Decomposition", Med. Phys. 17 (3), pg. 327-341, May/Jun 1990.

72 N. C. Murray, R. J. Lacey and P. H. Mason, "Exploitation of X-rays Technology for the Detection of Contraband, Aviation Security Applications", European Conference on Security and Detection, Conference Publication No. 437, pg. 13-18, 28-30 April 1997.

73 J. Yinon, "Forensic and Environmental Detection of Explosives", John Wiley & Sons Ltd., ISBN 0471983713, pg. 88-103, 1999.

74 Miles W. R., "Movement Interpretation of the Silhouette of a Revolving Fan", Amer. J.

Psychology, 43, pp. 392-405, 1931.

75 Metzger W., Tiefenerscheinungen in Optishen Bewegungnsfeldern. Psychol. Forsh., 20,

pp. 195-260, 1934.

76 A. C. Kak and Malcolm Slaney, 'Principles of Computerized Tomographic Imaging', IEEE Press, 1988.

77 A. C. Kak and Malcolm Slaney, 'Principles of Computerized Tomographic Imaging', Society for Industrial Mathematics, ISBN-10: 089871494X, 2001.

78 Antti Happonen, 'Advances in Tomographic Imaging', VDM Verlag, ISBN-10: 3639087917, 2008.

79 S. Gondrom, S. Schröpfer, FhG ITFP, Saarbrücken, D, 'Digital computed laminography and tomosynthesis - functional principles andindustrial applications', International Symposium on Computerized Tomography for Industrial Applications and Image Processing in Radiology March, 15 - 17, 1999 Berlin, Germany.

80 J. Zhou, 'Entwicklung eines Röntgen-Computerlaminographie-Verfahrens für die Materialprüfung', Thesis, Technical Faculty, University of Saarbrücken, 1995, unpublished.

81 J. Zhou, M. Maisl, H. Reiter, and W. Arnold, 'Computed Laminography for Materials Testing', Applied Physics Letters 68 (1996) 3500.

82 FRIEND D.B., JONES A., "A stereoscopic television system for reactor inspection", C.E.G.B. Research Division, March 1980.

83 JONES A., "Some theoretical aspects of the design of stereoscopic television systems", C.E.G.B. Research Division, March 1980.

84 M. Sonka, V. Hlavac, R. Boyle, "Image Processing, Analysis and Machine Vision", First Edition, Chapman & Hall Computing, pp. 112-179, 1993.

85 K.S. Fu, J.K. Mui, "A Survey on Image Segmentation", Pattern Recognition, Vol. 13,   pp. 3-16, 1981.

86 N.R. Pal, S.K. Pal, "A Review on Image Segmentation Techniques", Pattern Recognition, Vol. 26(9), pp. 1277-1294, 1993.

87 N. Otsu, "A Thresholding Selection Method from Gray-level Histogram", IEEE Transactions on System, Man, Cybernet, Vol. 9(1), pp. 62-66, January 1979.

88 J.N. Kapur, P.K. Sahoo, A.K.C. Wong, "A New Method for Gray-Level Picture Thresholding Using the Entropy of the Histogram", Computer Vision, Graphics and Image Processing, Vol. 29(3), pp. 273-285, 1985.

89 W.H. Tsai, "Moment-preserving Thresholding: A New Approach", Computer Vision, Graphics and Image Processing, Vol. 29(3), pp. 377-393, 1985.

90 L. Kittler, J. Illingworth, "Minimum Error Thresholding", Pattern Recognition, Vol. 19(1), pp. 41-47, 1986.

91 J.M.S. Prewitt, M.L. Mendelsohn, "The Analysis of Cell Images", Transaction on New York Academy of Sciences, Vol. 128, pp. 0035-1053, 1996.

92 J.S. Weszka, "A Survey of Threshold Selection Techniques", Computer Graphics and Image Processing, Vol. 7, pp. 259-265, 1978.

93 P.K. Sahoo, S. Soltani, A.K.C. Wong, "A Survey of Thresholding Techniques", Computer Vision, Graphics and Image Processing, Vol. 41(2), pp. 233-60, 1988.

94 C.A. Glasbey, "An Analysis of Histogram-based Thresholding Algorithm", CVGIP: Graphical Models and Image Processing, Vol. 55(6), pp. 532-537, November 1993.

95 D.M. Tsai, "A Fast Thresholding Selection Procedure for Multimodal and Unimodal Histograms", Pattern Recognition Letters, Vol. 16(6), pp. 653-666, 1995.

96 C.C. Chang, L.L. Wang, "A Fast Multilevel Thresholding Method Based on Lowpass and Highpass Filtering", Pattern Recognition Letters, Vol. 18(14), pp. 1469-1478, 1997.

97 P.S. Liao, T.S. Chen, P.C. Chung, "A Fast Algorithm for Multilevel Thresholding", Journal of Information Science and Engineering, Vol. 17, pp. 713-727, 2001.

98 D. Marr, E. Hildreth, "Theory of Edge Detection", Proceedings of the Royal Society of London, Vol. 207, pp. 187-217, 1980.

99 J. Canny, "A Computational Approach to Edge Detection", IEEE Transactions on Pattern Analysis and Machine Intelligence, Vol. 8(6), pp. 679-698, November 1986.

100 J.R. Beltran, J. Navarro, "Wavelet-based Edge Detection and Classification", Proceedings EUSIPCO-94, pp. 1381-1384, 1994.

101 S.E. Umbaugh, "Computer Vision and Image Processing: A Practical Approach Using CVIPtools", Prentice-Hall, pp. 61-79, 1998.

102 S. Venkatesh, P. Rosin, "Dynamic Threshold Determination by Local and Global Edge Evaluation", SPIE Proceedings, Intelligence, Vol. 1964, pp. 40-50, 1993.

103 Judd, D.B. & Wyszecki, G. Colour in Business Science and Industry, 3rd ed., p. 388, Wiley, New York (1975).

104 R.W.G. Hunt, Ellis Horwood, "Measuring Colour" Second edition, 1991, ISBN - 013567686x.

105 R.W.G. Hunt, 'The Reproduction of Colour' Sixth edition, 2004, ISBN-10: 0470024259.

106 Walraven, P. L.& Bouman, M. A. Vision Research, 6, 567 (1966).

107 Mollon, J.D. Ann. Rev. Psychol. 33, 41 (1982).

108 R.W.G. Hunt, "Measuring Colour" Thrid edition, 1998, ISBN-10: 0863433871.

109 R. C. Gonzalez and R. E. Woods, Digital Image Processing, Prentice Hall (Second Edition), 2002.

110 R. N. Czerwinski, D. L. Jones, and W. D. O'Brien, Jr., "Detection of Lines and Boundaries in Speckle Images Application to Medical Ultrasound," IEEE Transactions on Medical Imaging Vol. 18, No. 2, pp. 126-136, February 1999.

111 J. Dai and S. Zhou, "Computer Aided Pseudo-color Coding of Gray Image: Complementary Color Coding Technique," Proceedings of the SPIE, The International Society for Optical Engineering, Vol. 2898, pp. 186-191, 1996.

112 B. Abidi, Y. Zheng, A. Gribok, and M. Abidi, "Screener Evaluation of Pseudo-Colored Single Energy X-Ray Luggage Images," Proc. of IEEE Conference on Computer Vision and Pattern Recognition, Workshop CDROM, San Diego, CA, USA, June 2005.

113 Matthew Bernd Hilscher, "Performance Implications of Alternative Colour-codes in Airport X-ray Baggage Screening" PhD Thesis at the University of Central Florida, Orlando, Florida. May, 2005.

114 Rafael C. Gonzalez, Richard E. Woods, "Digital Image Processing" Second Edition, 1992. pp295-296, ISBN 0-13-094650-8.

115 Sonia O'Connor; Mary Brooks, "X-Radiography of Textiles, Dress and Related Objects", Butterworth-Heinemann, ISBN-10: 0750666323, 2007.

116 R. M. Harrison, "Digital radiography − a review of detector design", Nuclear Insrum. and Meth., vol. A310, pp. 24-34, 1991.

117 Faiz M Khan (Author), Faiz M. Khan, "The Physics of Radiation Therapy", third edition, Lippincott Williams & Wilkins, ISBN-10: 0781730651, 2003.

118 Stewart C. Bushong, 'Radiologic Science for Technologists: Physics, Biology, and Protection', 9 edition, Mosby, 2008.

119 International Commission on Radiation Units and Measurements- U.S.A., "Tissue Substitutes in Radiation Dosimetry and Measurement", ICRU report 44, US, (15 January 1989).

120 P. Sprawls, "Physical Principles of Medical Imaging", second edition, An Aspen Publication, pp. 67, (1993)

121 A. K. Novakoff, "FAA bulk technology overview for explosives detection", Proceedings of SPIE vol.1824, pp. 2-12, (1992).

122 National Research Council, U.S. Committee on Commercial Aviation Security, "Detection of explosives for commercial aviation security", Committee on Commercial Aviation Security, National Materials Advisory Board, Commission on Engineering and Technical Systems, National Research Council, Washington, D.C. National Academy Press, (1993)

123 S. V. Naydenov, V. D. Ryzhikov, C. F. Smith, "Direct reconstruction of the effective atomic number of materials by the method of multi-energy radiography", Nuclear Instrum. and Meth., vol. B215, pp. 552-560, 2004.

124 S. V. Naydenov, V. D. Ryzhikov, "Multi-energy techniques for radiographic monitoring of chemical composition: theory and applications", Nuclear Instrum. and Meth., vol. A505, pp. 556-558, 2003.

125 Sergey V. Naydenov, Vladimir V. Yanovsky, 'Geometry and dynamics of billiards in symmetric phase space', International Conference dedicated to the 90th anniversary of A.I. Akhiezer (QEDSP 2001), October 30 - November 3, 2001, Kharkov, Ukraine.

126 Hoheisel, M.; Bernhardt, P.; Lawaczeck, R.; Pietsch, H., 'Comparison of polychromatic and monochromatic x-rays for imaging', Medical Imaging 2006: Physics of Medical Imaging. Edited by Flynn, Michael J.; Hsieh, Jiang. Proceedings of the SPIE, Volume 6142, pp. 71-78 (2006).

127 Emil Y Sidky, Yu Zou and Xiaochuan Pan, 'Impact of polychromatic x-ray sources on helical, cone-beam computed tomography and dual-energy methods', Phys. Med. Biol. 49 (2004) 2293–2303.

128 P Baldelli, A Taibi, A Tuffanelli and M Gambaccini, 'Dose comparison between conventional and quasi-monochromatic systems for diagnostic radiology', Phys. Med. Biol. 49 (2004) 4135–4146.

129 C. T. Kelley, Solving Nonlinear Equations with Newton's Method, no 1 in Fundamentals of Algorithms, SIAM, 2003

130 J. M. Ortega, W. C. Rheinboldt, Iterative Solution of Nonlinear Equations in Several Variables. Classics in Applied Mathematics, SIAM, 2000.

131 Tjalling J. Ypma, Historical development of the Newton-Raphson method, SIAM Review 37 (4), 531–551, 1995.

132 "Atomic Weights and Isotopic Compositions for All Elements". National Institute of Standards and Technology. Retrieved on 2007-01-04.

133 Official website of Wikipedia (http://en.wikipedia.org/wiki/Atom#cite_note-iupac-60).

134 L. Helfen, T. Baumbach, P. Mikulík, D. Kiel, P. Pernot, P. Cloetens and J. Baruchel, Appl. Phys. Lett. 86, 071915 (2005).

135 L. Helfen, A. Myagotin, P. Pernot, M. DiMichiel, P. Mikulík, A. Berthold, T. Baumbach, Nucl. Instr. Meth. A, 563, 163-166 (2006).

136 Niklason LT, Christian BT, Niklason LE, et al. Digital tomosynthesis in breast imaging. Radiology 1997; 205:399–406.

137 G. Lauritsch and W. H. Harer, ″A theoretical framework for filtered backprojection in tomosynthesis,″ Proc. SPIE 3338, pp. 1127– 1137, 1998.

138 G.-H. Chen, S. Leng, and C. Mistretta, ″A novel extension of the parallel-beam projection-slice theorem to the divergent fan-beam and cone-beam projections,″ Med. Phys. 32, pp. 654– 665, 2005.

139 Jeremy Birn, 'Digital Lighting and Rendering', New Riders Press, 2nd edition, ISBN-10: 0321316312 , 2006.

140 Alexandre Faure, Bernard Floccard, Frank Pilleul, Frédéric Faure, Bruno Badinand, Nicolas Mennesson, Thierry Ould, Christian Guillaume, Albrice Levrat, Farida Benatir and Bernard Allaouchiche, 'Multiplanar reconstruction: a new method for the diagnosis of tracheobronchial rupture?', Springer, DOI10.1007/s00134-007-0830-9, 2007.

141 A. Ardeshir Goshtasby, '2-D and 3-D Image Registration', Wiley-Interscience; 1st edition, ISBN-10: 0471649546, 2005.

142 National Research Council, U.S. Committee on Commercial Aviation Security, "Detection of explosives for commercial aviation security. Committee on Commercial Aviation Security, National Materials Advisory Board, Commission on Engineering and Technical Systems, National Research Council", Washington, D.C. National Academy Press, ISBN 0309049458, 1993.

APPENDIX

APPENDIX A

GREY LEVEL MULTIPLE-VIEW DUAL-ENERGY X-RAY

IMAGES.

-9°

-8°

-7°

-6°

-5°

-4°

-3º

-2º

-1º

0º

1º

2º

3º

4º

5º

6º

7º

8º
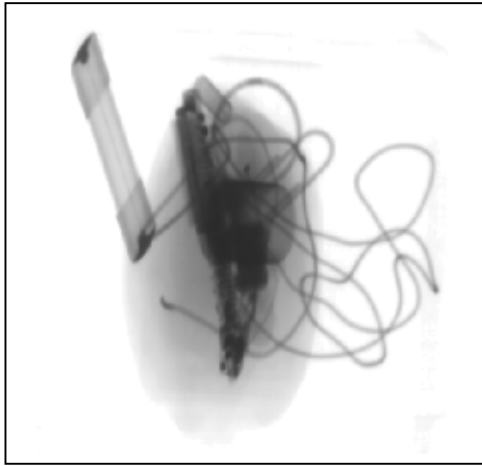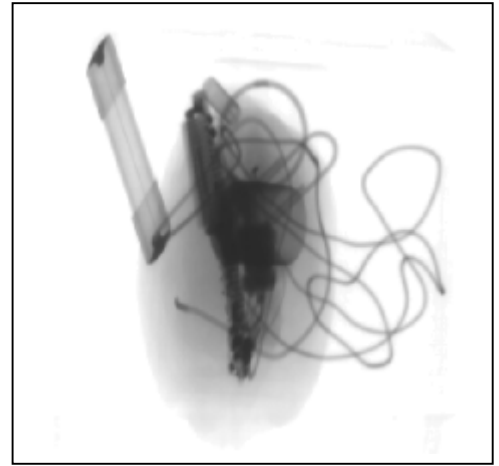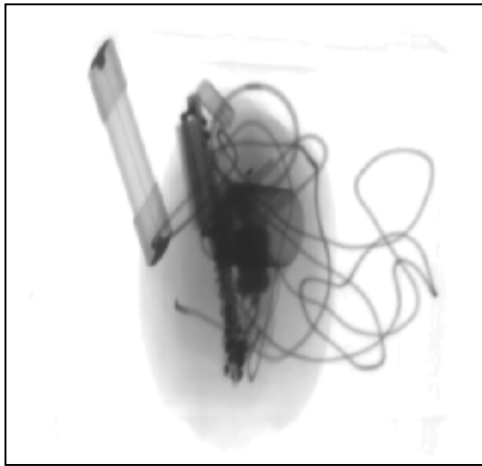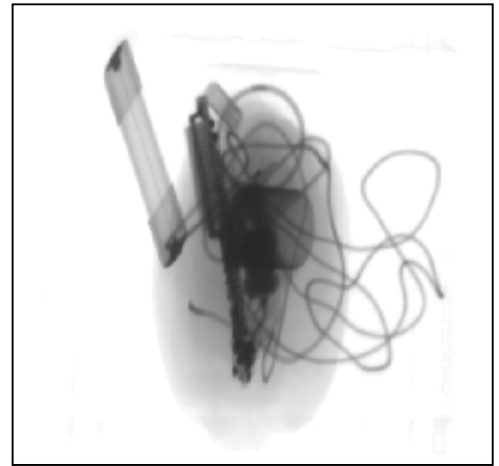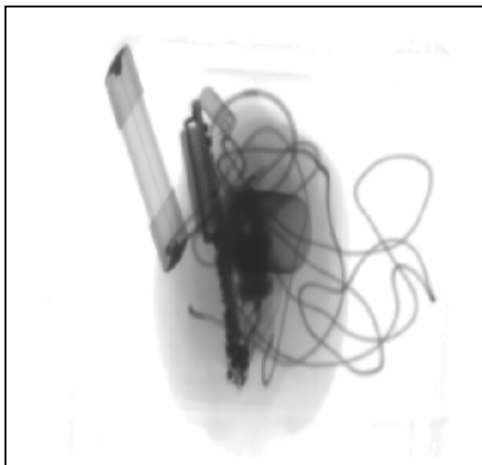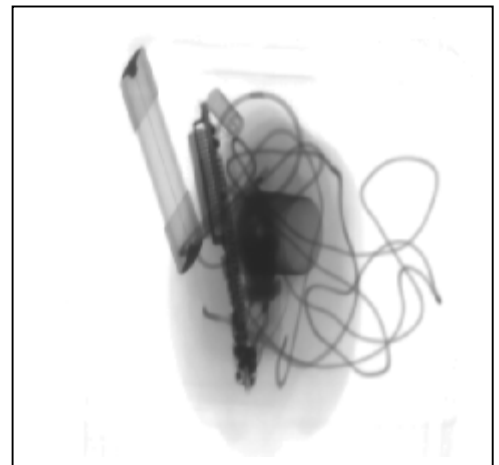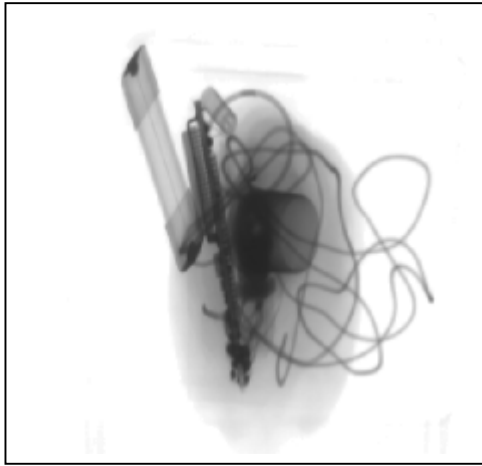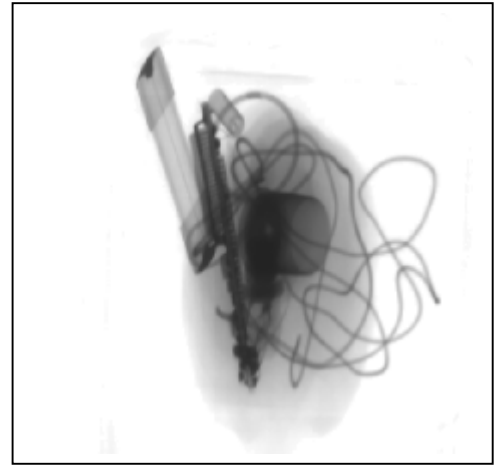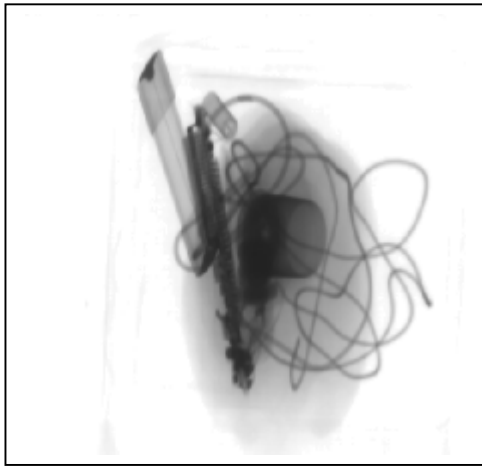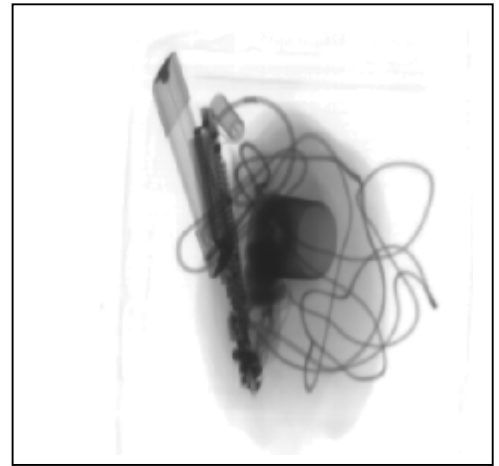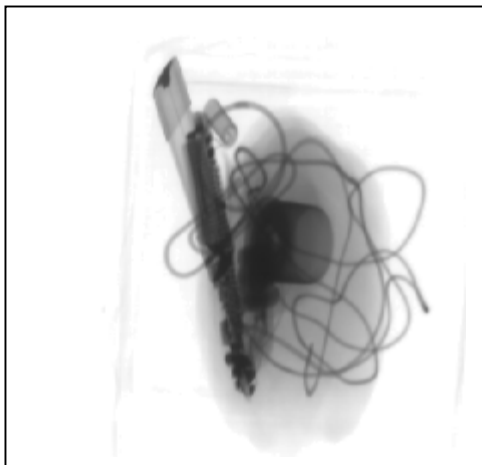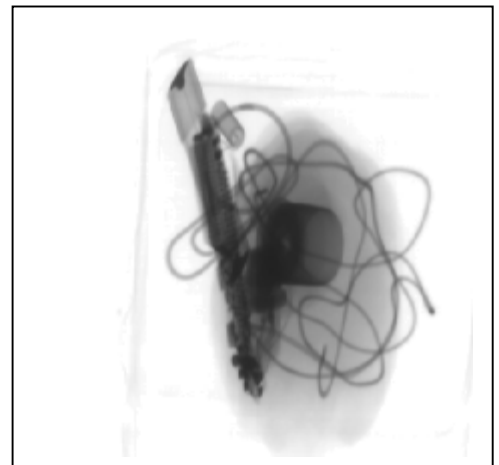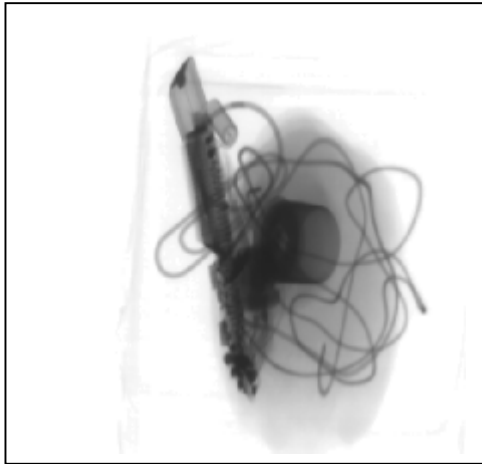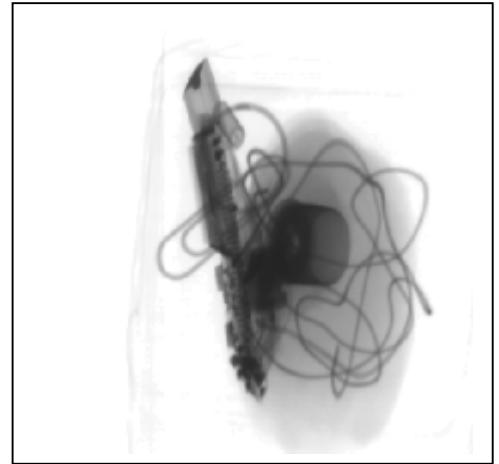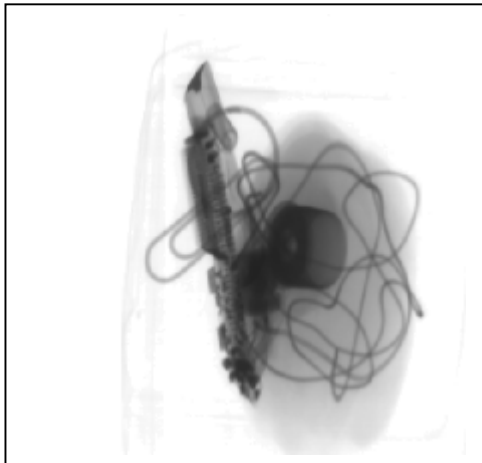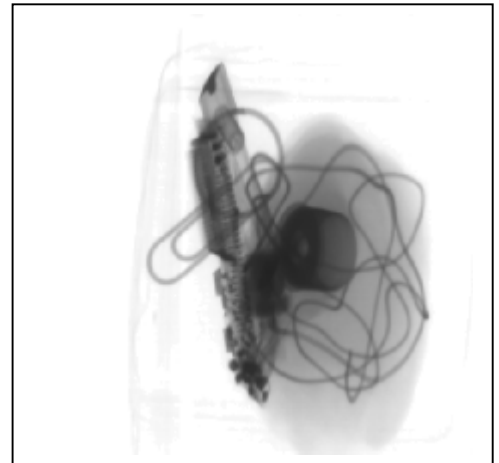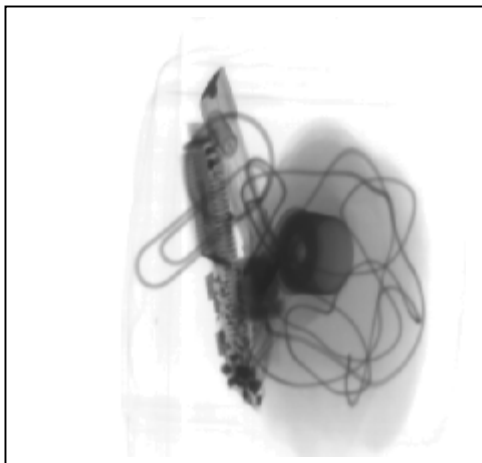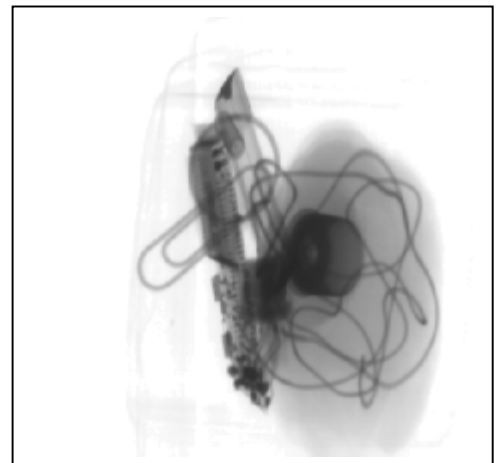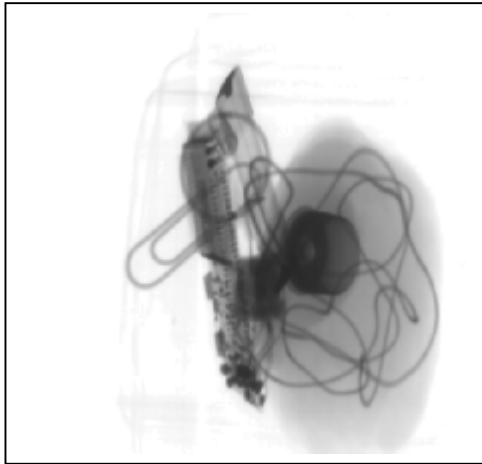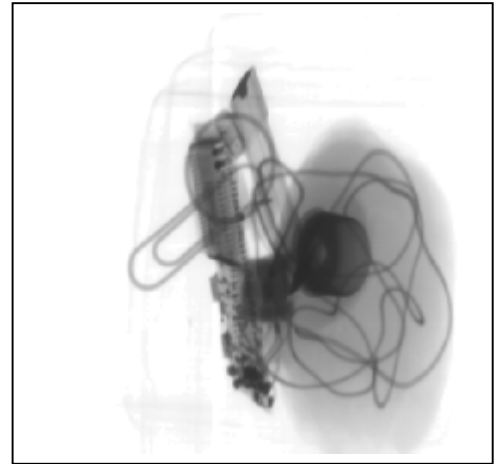
9°   10°

APPENDIX B

MULTIPLE-VIEW DUAL-ENERGY X-RAY IMAGES

COLOUR CODED BY EMPLOY 'STANDARD' COLOUR

PALETTE

-9º

-8º


-7º

-6º

-5º

-4º

-3°   -2°

1°   0°

1°   2°

3º

4º

5º

6º

7º

8º
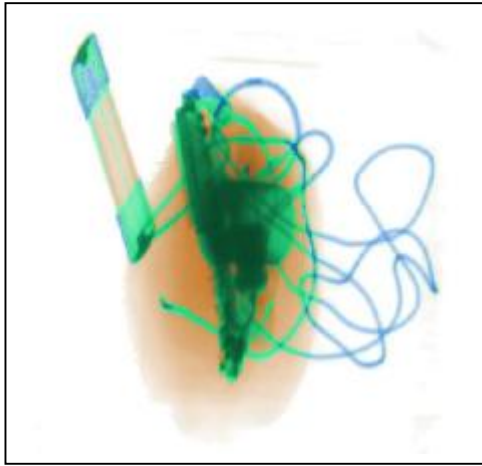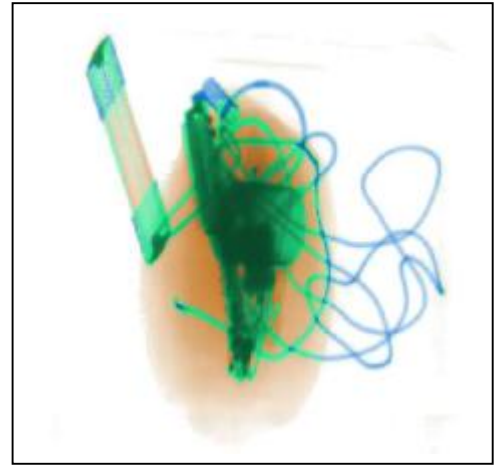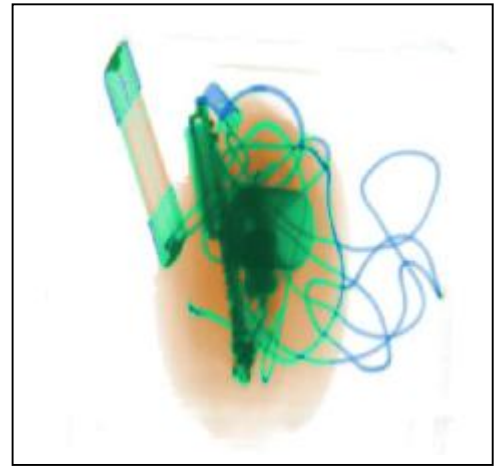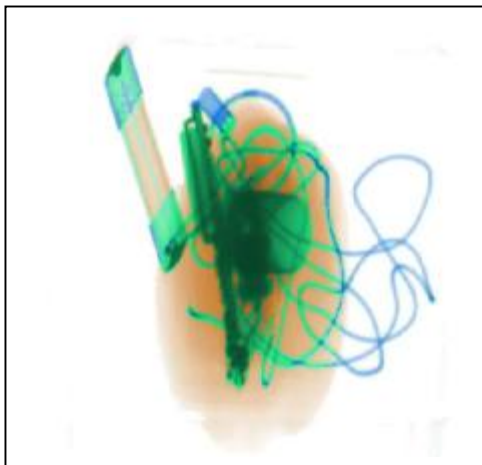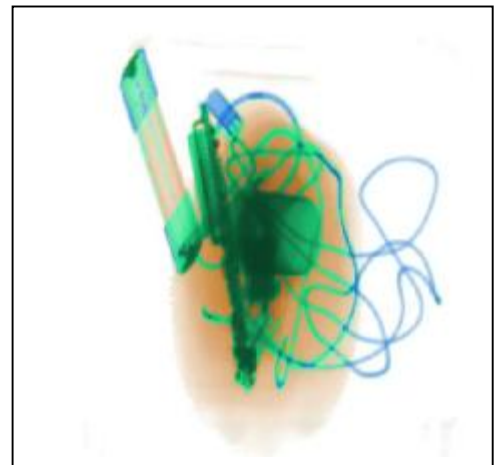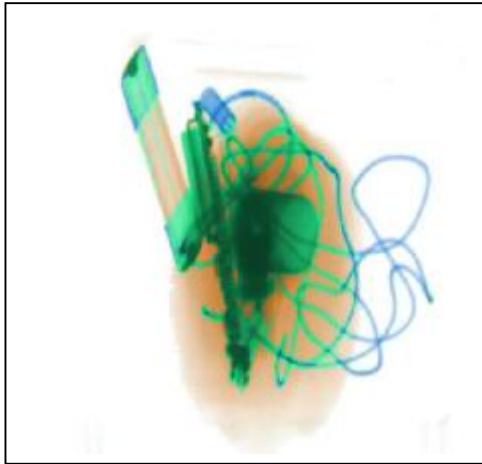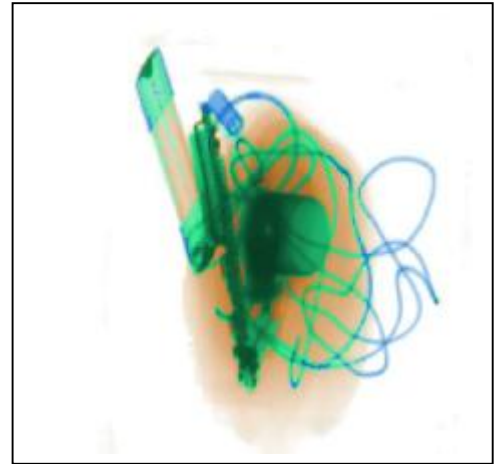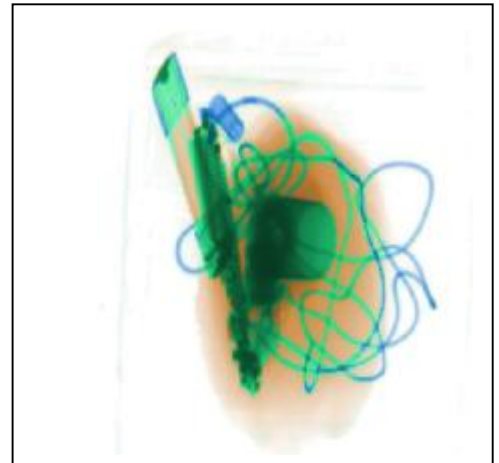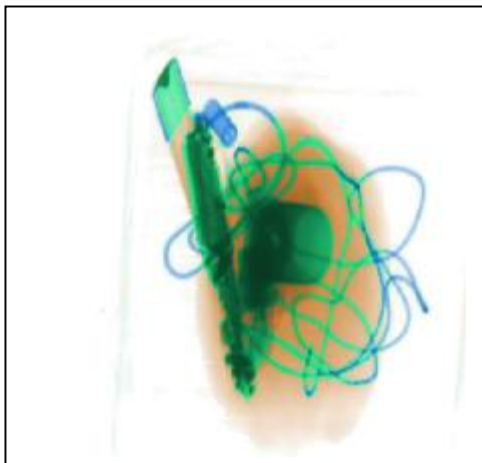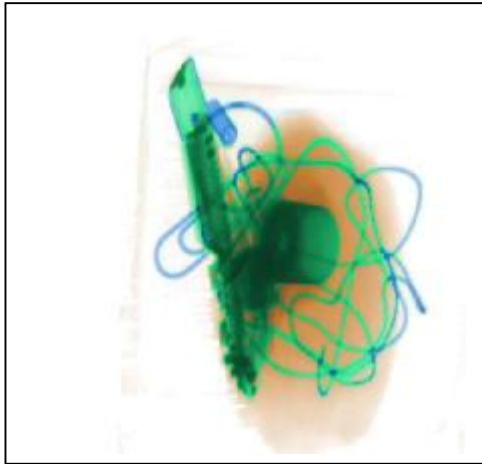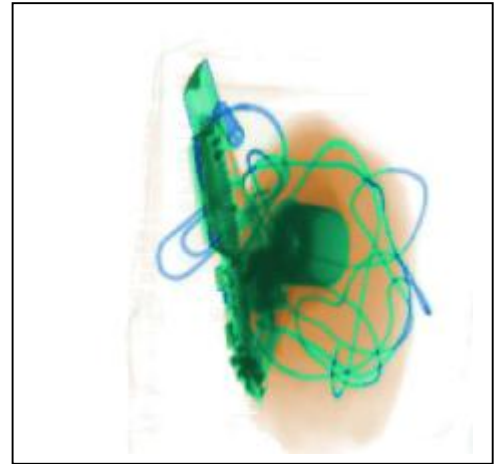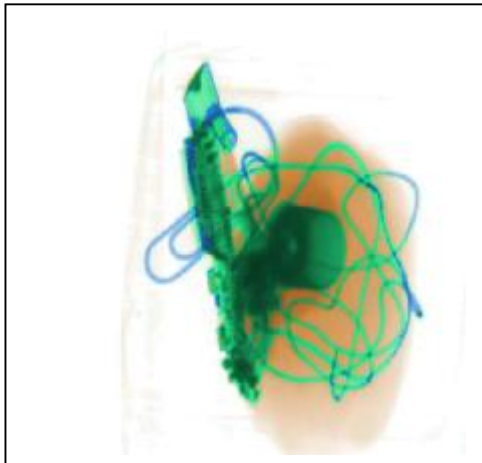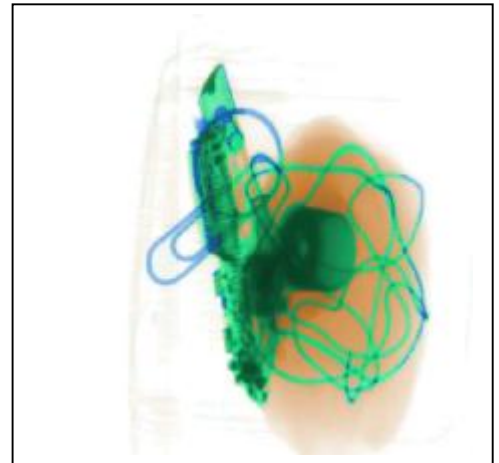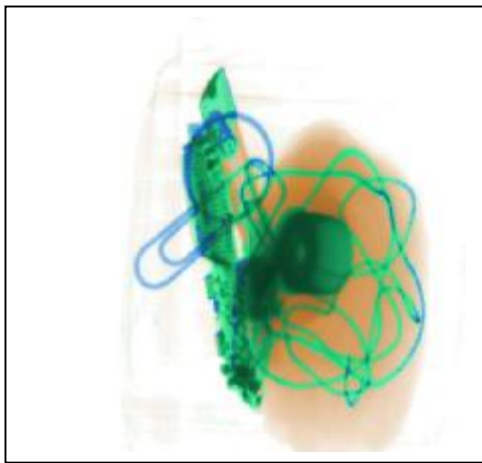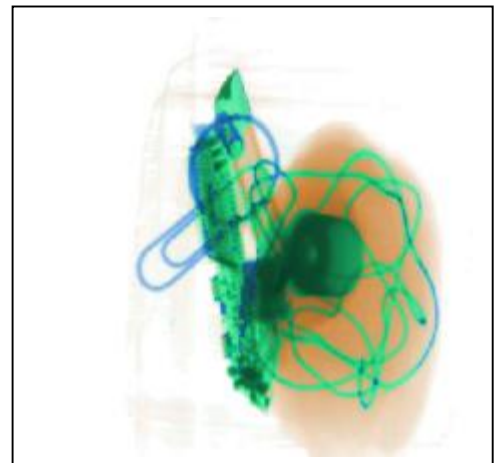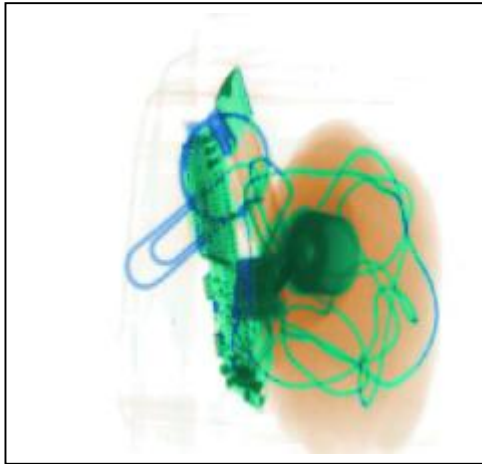
9°


10°

APPENDIX C

MULTIPLE-VIEW DUAL-ENERGY X-RAY IMAGES

COLOUR CODED BY EMPLOYING NEW COLOUR MAP

-9º

-8º

-7º

-6º

-5º

-4º

-3°

-2°

-1°

0°

1°

2°

152

3º


4º

5º

6º

7º

8º

9º   10º
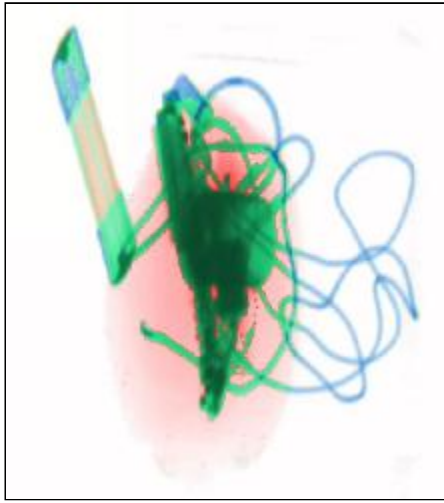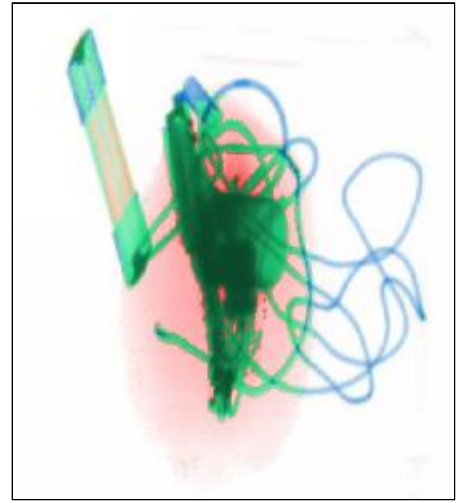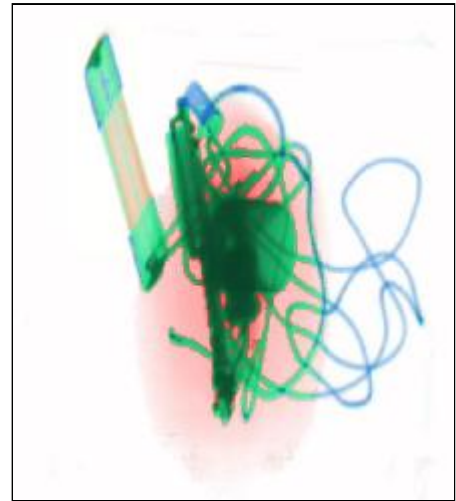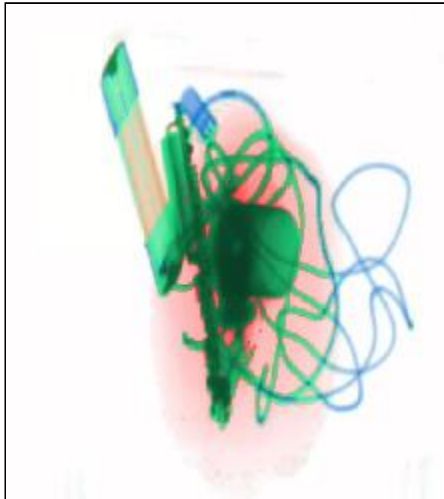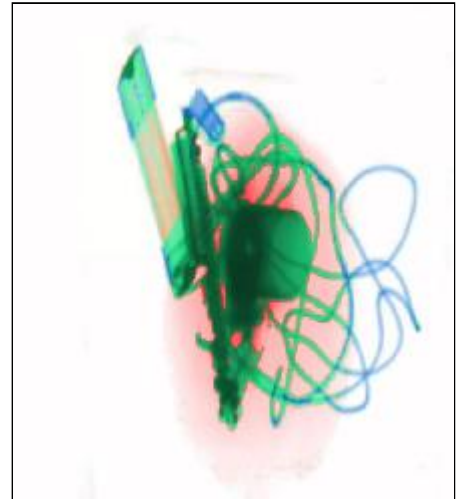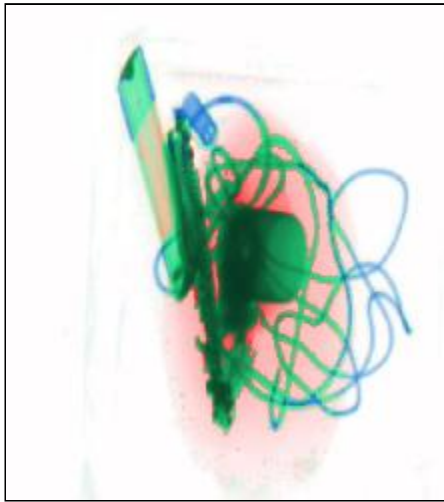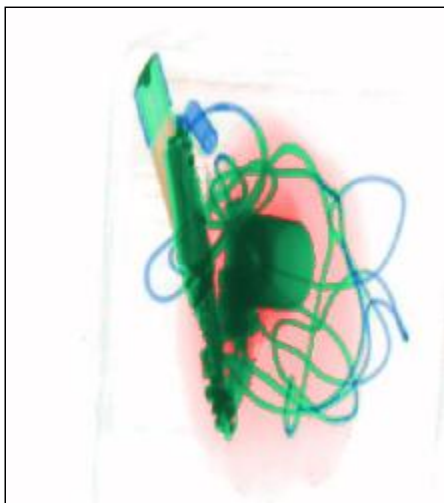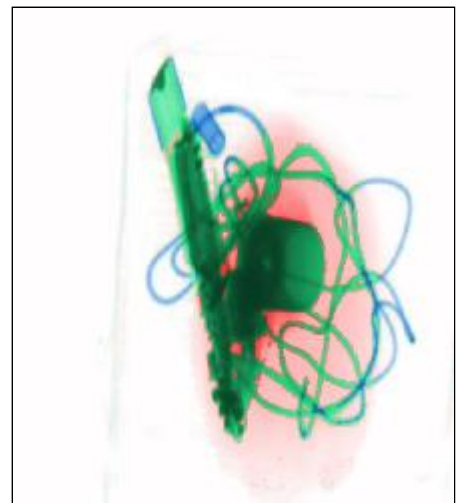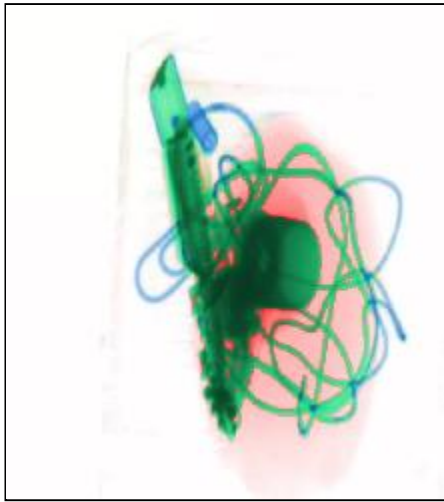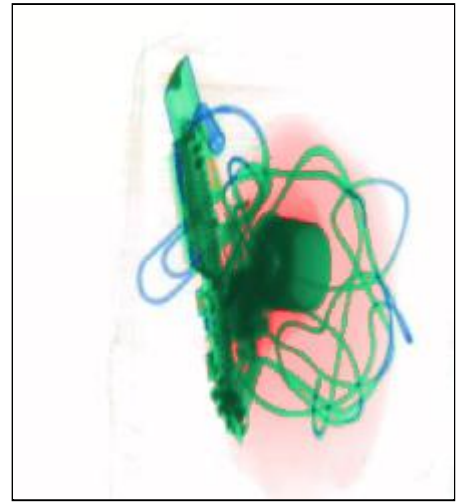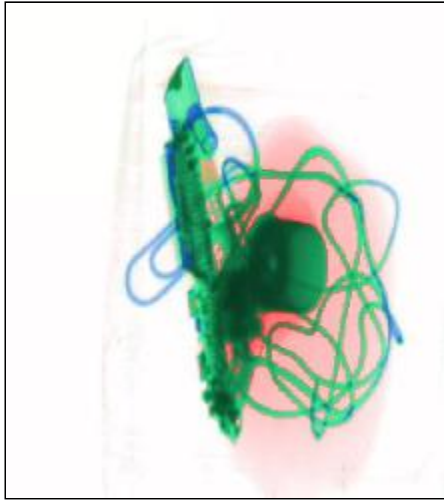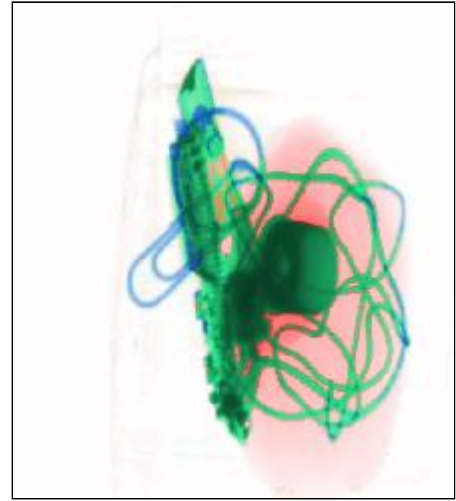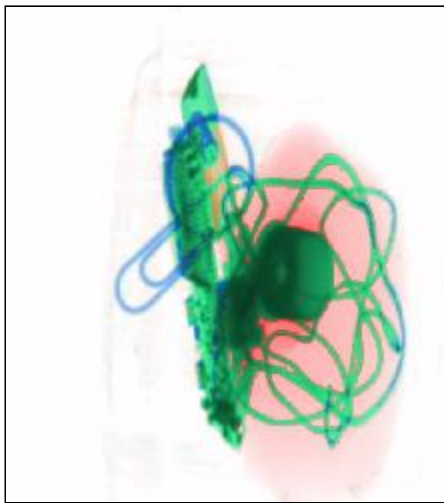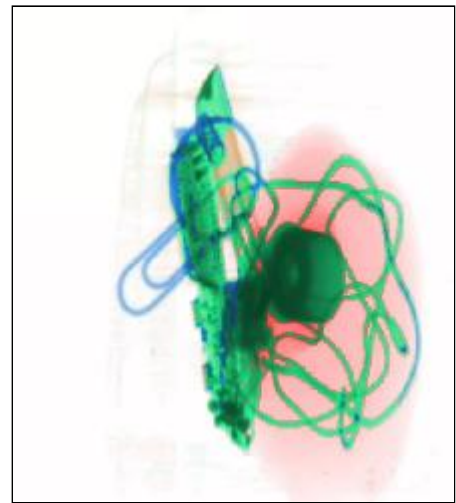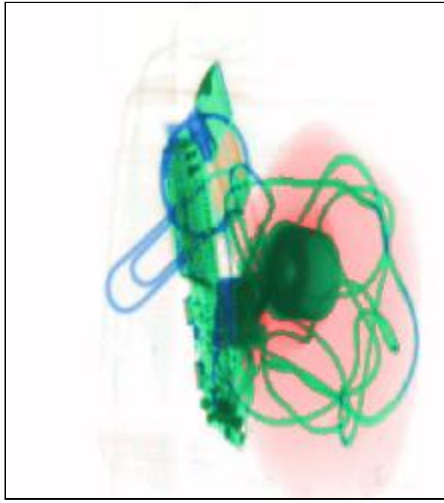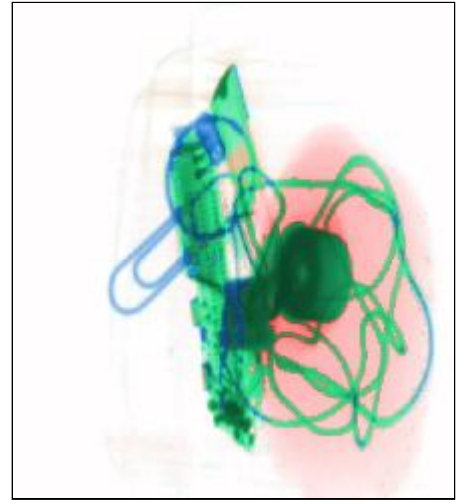
APPENDIX D

LOOK UP TABLE OF MATERIAL DISCRIMINATION

INFORMATION

(Full table in attached CD)

Part of low-energy look up table

intensity	atomic number	6.0000000000000000000	6.5000000000000000000
45		4391.79288164274000000000	562.77965852609700000000
46		4328.71138307445000000000	555.83337133408100000000
47		4266.54841938805000000000	548.98167169456000000000
48		4205.29335931246000000000	542.22330739970300000000
49		4144.93563320197000000000	535.55703557588300000000
50		4085.46473303625000000000	528.98162268367900000000
51		4026.87021242039000000000	522.49584451788000000000
52		3969.14168658487000000000	516.09848620748000000000
53		3912.26883238556000000000	509.78834221567900000000
54		3856.24138830373000000000	503.56421633988500000000
55		3801.04915444603000000000	497.42492171171300000000
56		3746.68199254453000000000	491.36928079698400000000
57		3693.12982595668000000000	485.39612539572700000000
58		3640.38263966532000000000	479.50429664217600000000
59		3588.43048027869000000000	473.69264500477500000000
60		3537.26345603045000000000	467.96003028617000000000
61		3486.87173677960000000000	462.30532162321900000000
62		3437.24555401060000000000	456.72739748698400000000
63		3388.37520083325000000000	451.22514568273300000000
64		3340.25103198277000000000	445.79746334994400000000
65		3292.86346381979000000000	440.44325696229900000000
66		3246.20297433030000000000	435.16144232768700000000
67		3200.26010312571000000000	429.95094458820700000000
68		3155.02545144282000000000	424.81069822016000000000
69		3110.48968214382000000000	419.73964703405800000000
70		3066.64351971630000000000	414.73674417461800000000
71		3023.47775027325000000000	409.80095212076300000000
72		2980.98322155304000000000	404.93124268562500000000
73		2939.15084291945000000000	400.12659701654200000000
74		2897.97158536164000000000	395.38600559505700000000
75		2857.43648149418000000000	390.70846823692300000000

Part of high-energy look up table

intensity	atomic number	6.00000000000000000000	6.50000000000000000000
50		4710.9548194967800000000	677.9125128499950000000
51		4660.9162437233800000000	668.3801670458540000000
52		4611.0405922738600000000	659.0070218735420000000
53		4561.3351783757500000000	649.7905776406900000000
54		4511.8071954227400000000	640.7283560960870000000
55		4462.4637169746600000000	631.8179004296720000000
56		4413.3116967574800000000	623.0567752725380000000
57		4364.3579686633300000000	614.4425666969320000000
58		4315.6092467504800000000	605.9728822162540000000
59		4267.0721252433600000000	597.6453507850580000000
60		4218.7530785325300000000	589.4576227990520000000
61		4170.6584611747100000000	581.4073700950960000000
62		4122.7945078927600000000	573.4922859512040000000
63		4075.1673335756800000000	565.7100850865440000000
64		4027.7829332786300000000	558.0585036614380000000
65		3980.6471822229100000000	550.5352992773590000000
66		3933.7658357959900000000	543.1382509769370000000
67		3887.1445295514400000000	535.8651592439510000000
68		3840.7887920902000000000	528.7138460033390000000
69		3794.7039806546300000000	521.6821546211880000000
70		3748.8954099402900000000	514.7679499047400000000
71		3703.3682232842000000000	507.9691181023910000000
72		3658.1274570706800000000	501.2835669036900000000
73		3613.1780278502300000000	494.7092254393390000000
74		3568.5247323394600000000	488.2440442811940000000
75		3524.1722474211600000000	481.8859954422640000000
76		3480.1251301442400000000	475.6330723767130000000
77		3436.3878177237800000000	469.4832899785700000000
78		3392.9646275409900000000	463.4346845881660000000
79		3349.8597571432300000000	457.4853139792620000000
80		3307.0772842440300000000	451.6332573719240000000
81		3264.6211667230200000000	445.8766154260800000000
82		3222.4952426260300000000	440.2135102428150000000
83		3180.7032301650000000000	434.6420853643660000000
84		3139.2487277180400000000	429.1605057741240000000
85		3098.1352138293900000000	423.7669578966330000000
86		3057.3660472094400000000	418.4596495975900000000
87		3016.9444667347400000000	413.2368101838470000000
88		2976.8735914479700000000	408.0966904034080000000
89		2937.1564205579800000000	403.0375624454310000000
90		2897.7958334397400000000	398.0577199402290000000
91		2858.7945896343900000000	393.1554779592650000000
92		2820.1553288492000000000	388.3291730151580000000
93		2781.8805709576000000000	383.5771630616820000000
94		2743.9727159991600000000	378.8978274937600000000
95		2706.4340441796000000000	374.2895671474710000000